CCD PHOTOMETRY OF NGC 3201

by

JAMES PHILIP BREWER

B.Sc., The University of Leeds, 1988

A THESIS SUBMITTED IN PARTIAL FULFILLMENT OF

THE REQUIREMENTS FOR THE DEGREE OF

MASTER OF SCIENCE

in

THE FACULTY OF GRADUATE STUDIES

(Department of Geophysics and Astronomy)

We accept this thesis as conforming

to the required standard

THE UNIVERSITY OF BRITISH COLUMBIA

September 1991

In presenting this thesis in partial fulfilment of the requirements for an advanced degree at the University of British Columbia, I agree that the Library shall make it freely available for reference and study. I further agree that permission for extensive copying of this thesis for scholarly purposes may be granted by the head of my department or by his or her representatives. It is understood that copying or publication of this thesis for financial gain shall not be allowed without my written permission.

Department of Geophysics & Astronomy

The University of British Columbia
Vancouver, Canada

Date 29 August '91

ABSTRACT

CCD observations of the halo globular cluster NGC 3201, acquired at the Dupont 2.5m telescope at Las Campanas, are reduced and analyzed. The data are from two separate observing runs. During the first run deep data were secured for a field at seven core radii from the centre, whilst during the second run, shallow data were secured for the central field of the cluster. Colour-magnitude diagrams are presented, and a two-colour diagram is constructed using data from the latter run. From the colour-magnitude diagram and colour-colour diagrams, estimates for reddening, metallicity, distance modulus and age are derived, and consistency with values in the literature is shown. Blue stragglers were observed in the central field, and are shown to be more centrally concentrated than subgiants in an equal magnitude interval. A UV bright star was observed in the central field, and magnitudes and colours are reported for it. The possible nature of this object is discussed.

Mass functions were derived using deep V and I band data, by binning both on mass and on luminosity. Discrepancies between the two mass functions are discussed and resolved. The counts in a background field are compared to those expected from the Galactic model of Bahcall and Soneira (1980, 1984), and a discrepancy is found at fainter magnitudes. Mass-luminosity relationships (MLRs) in V and I were used to generate an isochrone which showed good agreement with the data, lending credence to the MLRs. Finally, the slope of the mass function is measured for stars with $\mathcal{M} < 0.4\mathcal{M}_{\odot}$, and values are obtained for the half-mass relaxation time and 'destruction time' of NGC 3201. These values show consistency with the results of Richer *et al.* (1991).

CONTENTS

LIST OF FIGURES

LIST OF TABLES

ACKNOWLEDGMENTS

Thanks to life, for being such a wonderful and truly joyous experience.

"We are all in the gutter, but some of us are looking at the stars."

Oscar Wilde (1854-1900)

Chapter 1
PRELUDE

1.1 Globular Clusters, an Overview

Globular clusters are systems of stars which are gravitationally bound and long-lived, as opposed to Galactic clusters which tend to be loosely bound and short-lived. Most globular clusters appear spherical, their axial ratios lying between 0.9:1 and 1:1, though a few clusters have axial ratios of up to 0.6:1 in their outer regions. N-body modelling of globular cluster dynamics is not realizable with current computing technology, but their kinematics can be described by King Models (King 1966) which are spatially limited, steady state solutions of the Fokker-Planck equation. The Fokker-Planck equation is an approximation to the collisionless Boltzmann-equation. Globular clusters are Population II objects which, in the Milky Way, are found to have a bimodal metallicity distribution. There are both halo and disk globular clusters, the halo clusters having a low systemic rotation and a high random velocity dispersion, and the disk clusters having a larger rotation and a smaller random velocity dispersion (Zinn 1985).

The Milky Way has associated with it a system of 150 to 200 globular clusters, each of which contains approximately 10^5 stars. Globular clusters, *per se*, make a negligible contribution to the mass of the Galaxy. Over half of the globular clusters are at a distance of less than 10 kpc from the Galactic centre, the radius of the disk being 25 - 30 kpc (Mihalas and Binney 1981). The distribution extends far out into the halo, for example the globular cluster NGC 2419 is at a Galactocentric distance of 99.4 kpc (Webbink 1985). The distribution above the Galactic plane does not differ significantly from that in the two orthogonal directions; Shapley recognized this, and was able to determine the dimensions of the Milky Way, concluding that the sun is not near the centre of the Galaxy. This is contrary to what had been previously thought by Kapetyn, who had failed to allow for the absorption of starlight by interstellar material (Mihalas and Binney 1981).

Synthetic isochrone fitting to globular cluster colour-magnitude diagrams (CMDs) shows them to be approximately 15 gigayears (Gyr) old, with a definite age spread. These ages, on the scale defined by VandenBerg and Bell (1985, henceforth VB85), are hard to reconcile with the age of the universe derived using Hubble's constant, which is believed to lie in the range H_0=50 - 100 $kms^{-1}Mpc^{-1}$, implying an age of between 7 and 13 Gyr, assuming a k=0, Λ=0

Friedmann-Lemaître model (Börner 1988). The values may be reconciled if it is found that the *absolute ages* of the isochrones, which are very uncertain, are somewhat overestimated.

A globular cluster will show a large range in its surface brightness. Two parameters are used to characterize the surface brightness distribution, they are

- r_c=Core radius; the radius at which the surface brightness is half of its central value.
- r_t=Tidal radius; the radius at which the surface brightness reaches zero, often obtained by extrapolation of the surface brightness profile.

Of the Galactic globular clusters, 5/6 of them have $(0.3 \leq r_c \leq 10)$ pc and $(10 \leq r_t/r_c \leq 100)$. Inspection of Table 1.1 shows NGC 3201 to be typical in its surface brightness parameters. Most globular clusters have a core where the surface brightness changes slowly, *i.e.* they have an isothermal velocity dispersion, while for a few, the surface brightness keeps increasing down to the smallest radius which can be resolved in the cluster. These clusters are said to possess 'cusps' and are believed to be in the post core-collapse stage of evolution (Spitzer 1987).

The distribution of the integrated luminosity of globular clusters has a mean value of 4.8 with a dispersion of 0.5 in $\log\left(\frac{L_{cluster}}{L_\odot}\right)$. The central velocity dispersion, which can be obtained using line widths of integrated spectra or measurement of individual giants, combined with the virial theorem, allows for the total mass of a cluster to be estimated (this is model dependant). Using this method, it is found that the mass to light ratio, in solar units, is in the range 1 to 4, though recent studies by Richer and Fahlman (1991) and Richer *et al.* (1991), where data were fitted to King models, indicate values of around 6. Knowing this, and applying it to fainter clusters from which integrated spectra cannot be obtained, it would appear that the masses of globular clusters lie in the range 10^4 to 10^6 $\mathcal{M}_\odot$.

The integrated colour of globular clusters, $(B-V)_0$, is found to lie in the range $0\overset{m}{.}4 \leq (B-V)_0 \leq 0\overset{m}{.}8$, with the distribution peaking at $(B-V)_0 = 0\overset{m}{.}57$. This shows that the light from globular clusters is dominated by light from stars cooler than the sun, *i.e.* of a later spectral type than G5. An integrated colour is not a good parameter for classification; the colour of a star depends on two factors, *viz.*: temperature and metallicity.

Clusters can be classified into concentration classes, the classes being designated I to XII. In this system, devised by Shapley and Sawyer, class I clusters show the highest central concentration of stars whilst class XII clusters the lowest. The divisions were made such that the clusters divide almost equally between the twelve classes.

1.2 NGC 3201, Previous Studies

NGC 3201 is in Vela, a constellation in the southern hemisphere near Crux. The constellation of Vela lies partly in the plane of the Milky Way. NGC 3201 is a halo globular cluster, with fairly typical properties, as shown in Table 1.1.

One striking thing about NGC 3201 is its high heliocentric radial velocity, which is $+493$ kms^{-1} (Kinman 1959). This is the largest radial velocity, in the absolute sense, of any cluster in the Milky Way. If the effect of the sun's motion is removed from the radial velocity of NGC 3201, the radial velocity is approximately 240 kms^{-1}. With this velocity, the cluster probably cannot escape from the Milky Way, but will be in a retrograde orbit (White and Kraft 1972).

Menzies (1967) was the first person to produce a colour-magnitude diagram (CMD) on the *BV* system for NGC 3201. He measured 25 stars photoelectrically and 300 stars photographically, producing a CMD with a limiting magnitude of V=15$^{\rm m}\!.$6. The results of this work are published in Alcaino's (1974) Atlas of Globular Clusters. From his work, Menzies determined a distance of 6.9 kpc (Alcaino and Liller 1981) and a reddening of E($B-V$)=0$^{\rm m}\!.$07 (Alcaino *et al.* 1989) for NGC 3201.

Alcaino (1976) carried out an investigation of NGC 3201, using B and V band photometry, measuring 18 stars photoelectrically and 313 stars photographically. The limiting magnitude of his survey was V=16$^{\rm m}\!.$30. Alcaino derived $(m-M)_V$=14$^{\rm m}\!.$10 and E($B-V$)=0$^{\rm m}\!.$14, though he advises the use of caution with the reddening value. Alcaino noted that the horizontal branch was richly populated with blue, red and RR-Lyrae stars.

Lee (1977) performed *UBV* photometry on NGC 3201, measuring 78 stars photoelectrically and 649 photographically. In this study, U, B, and V magnitudes were obtained for all stars having $V < 15^{\rm m}\!.8$, within 5.8 *arcmin* of the cluster centre. Lee noted that the CMD of NGC 3201 resembles that of M3, the main difference between the clusters being that NGC 3201 has a concentration class of X, while M3 has a concentration class of VI (Lang 1980). Using a two-colour diagram Lee deduced E($B-V$)=0$^{\rm m}\!.$21 $\pm$ 0$^{\rm m}\!.$02, and the true distance modulus to be $(m-M)_0$=13$^{\rm m}\!.$57, assuming that M$_V$(horizontal branch)=0$^{\rm m}\!.$6. Using metal abundance indicators, Lee deduced the metallicity of NGC 3201 as being -1.2 ± 0.1 dex relative to the Hyades. Lee (1977) suggests that he may have blue stragglers in his photometry, though he stresses that his photometry is not reliable at the magnitude of the candidate blue stragglers.

Alcaino and Liller (1981) used a Pickering-Racine wedge, a device which produces two images with a constant magnitude difference between them for each star, to perform photographic photometry on 1452 stars in NGC 3201. The magnitude limit of their survey was V=19$^{\rm m}$.6, and was the first study which reached the main sequence turn off. Alcaino and Liller determined the turn off to lie at a magnitude of V=18$^{\rm m}$.0 $\pm$ 0$^{\rm m}$.18, and a colour of $(B-V)$=0$^{\rm m}$.61 $\pm$ 0$^{\rm m}$.03. They deduced a distance modulus of $(m-M)_V$=14$^{\rm m}$.07 $\pm$ 0$^{\rm m}$.15 and a reddening of E$(B-V)$=0$^{\rm m}$.22 $\pm$ 0$^{\rm m}$.03. Alcaino and Liller also estimated the age of the cluster as lying between 7.9 and 12.3 Gyr by several means, including using the formula of Iben and Rood (1970), fitting Demarque and McClure's (1977) isochrones and Carney's (1980) relationship, based on Demarque and McClure's (1977) isochrones.

Penny (1984), working with Griffiths, was the first to produce CMDs for NGC 3201 by the use of a CCD (see §2.1) detector. Using *B*, *V* and *I* filters, they produced CMDs which extend below the main sequence turn off, and are well defined down to V= 21$^{\rm m}$.0. Metallicity and reddening were not determined in this study, but VandenBerg (1983) isochrones were fitted to the data, and agreement was found between the morphologies in the colour-magnitude plane.

Alcaino, Liller and Alvarado 1989 (henceforth ALA89) used 67 CCD frames obtained at the 1.54 metre Danish telescope at La Silla, European Southern Observatory, to perform *BVRI* photometry on NGC 3201. They found the main sequence turn off at a magnitude of V=18$^{\rm m}$.20 $\pm$ 0$^{\rm m}$.1, and a colour of $(B-V)$=0$^{\rm m}$.57 $\pm$ 0$^{\rm m}$.02. They report the magnitude difference between the turnoff and the horizontal branch as being 3$^{\rm m}$.44 $\pm$ 0$^{\rm m}$.12. The CMDs were fitted to VB85 isochrones, a best fit being found for Y=0.2, [Fe/H]=$-$1.27, α=1.65, $(m-M)_V$=14$^{\rm m}$.00, and an age of 16 $\pm$ 2 Gyrs.

1.3 Objectives of Present Study

The main objective of the present study is to determine the mass function of NGC 3201, which has not been published. The data are also used to investigate the reddening, metallicity, distance modulus and age of the cluster, as well as looking for a binary sequence and the concentration of the blue stragglers.

TABLE 1.1: Some parameters of NGC 3201

Quantity	Value	Reference
Right Ascension, α_{1950}	$10^h15^m34^s$	Webbink (1985)
Declination, δ_{1950}	$-46°\ 09'\ 42''$	Webbink (1985)
Galactic Longitude, l	$277\overset{\circ}{.}229$	Webbink (1985)
Galactic Latitude, b	$8\overset{\circ}{.}641$	Webbink (1985)
Foreground Reddening, $E(B-V)$	$0\overset{m}{.}21$	Lee (1977)
Heliocentric Distance, R_S	5.0 Kpc	Webbink (1985)
Integrated Absolute Magnitude, M_V	-7.47	Webbink (1985)
Magnitude of Horizontal Branch, V_{HB}	$14\overset{m}{.}75$	Lee (1977)
Colour of Subgiant Branch at Horizontal Branch Level, $(B-V)_{0,g}$	$0\overset{m}{.}79$	Lee (1977)
Concentration Class	X	Lang (1980)
Ratio of Stars in Horizontal Branch, N_{BH}:N_{VA}:N_{RH}, for r < 5'.8	65:60:51	Lee (1977)
Galactocentric Distance, R_{GC}	9.5 Kpc	Webbink (1985)
Heliocentric Radial Velocity, v_r	493 km s^{-1}	Kinman (1959)
Metallicity, [m/H]	-1.6 dex	Webbink (1985)
Core Radius, r_c	1.58 pc	Webbink (1985)
Limiting Radius, r_t	52.4 pc	Webbink (1985)
Core Concentration Parameter	1.55	Webbink (1985)

Chapter 2
OBSERVATIONS AND REDUCTIONS

2.1 Charge-Coupled Devices

The mid-1970's were the dawn of a new age for observational astronomy with the invention of the charged-coupled device (CCD). A CCD is near to being the perfect detector; it has a high quantum efficiency (QE), is linear in response to near its saturation limit, and has a large dynamic range. CCDs were originally designed for television applications, having an imaging and read out area, this type of CCD is known as a 'frame transfer device'. The Texas Instruments 800 $\times$ 800 CCD, made for the Hubble Space Telescope wide-field/planetary camera, and the Tektronix CCD, both used for the observations in this thesis, are for non-television applications and have only an imaging area.

The principle of operation of a CCD is quite simple: a photon incident upon the silicon of a CCD will cause the production of an electron/hole pair. Electrodes are used to create potential wells in the silicon in which the photoelectrons are trapped. By use of driving pulses the charge can be transferred along the CCD. An analogue to digital converter is used to read out the accumulated charge, and the actual values obtained are in terms of analogue to digital units (ADUs). The read out process has read out noise (RON) associated with it. This noise is reduced by cooling, but at the expense of sensitivity loss at the red end of the spectrum.

A bias frame is a frame containing only the pedestal which was imposed on the CCD before an exposure. This helps to alleviate the low level charge transfer inefficiency. The CCDs used for the observations in this thesis were 'injected' with charge, to create a pedestal, before the actual exposure. MacKay (1986) states that "*The only uniform CCD is a dead CCD.*" The response of any contemporary CCD is not uniform; individual pixels vary in their QEs, and there is often a large scale structure over the chip. To overcome the non-linearities, 'flat fields', images of an area with uniform illumination, are taken using the appropriate filter and normalized. These are then divided into an image to normalize the response of the pixels. This is not an ideal solution, non uniformities are colour dependent and so it is impossible to correct the field in a perfect manner as the objects in the field will have varying colours. Either dome flats, using artificial illumination on the inside of the dome, sky flats, which are images of the dusk, dawn or dark sky are used. MacKay (1986) says of flat fielding that it " . . . *is at best a compromise and in no way a substitute for intrinsic device uniformity.*"

2.2 IRAF

IRAF (Image Reduction and Analysis Facility) is a general purpose software system, containing a suite of programs for astronomical applications, which include routines capable of handling CCD data frames. The IRAF project was initiated in the autumn of 1981 at the Kitt Peak National Observatory, the project later being taken over and further developed by the National Optical Astronomy Observatories. The version of IRAF that was mainly used was 2.9.1, though earlier versions were utilized.

2.3 Data

In this thesis two data sets are analyzed. The deeper of the two data sets was secured using the 2.5 metre Dupont telescope at Las Campanas Observatory in Chile, on the nights of May 22/23 and May 23/24 1988. The observers were G.G. Fahlman and I.B. Thompson. This data set will be referred to as the *TI data*, and observation numbers will have the prefix *nee*, an acronym for nineteen eighty eight, for the rest of this thesis. The detector used for the observations was a Texas Instruments CCD, which had the characteristics shown in Table 2.1. The telescope configuration gave a plate scale of 0.162 *arcsec* per pixel, which gives a total field area of approximately $2'\,9'' \times 2'\,9''$. The cluster field is located at $\alpha_{1988}=10^h\ 16^m\ 26.7^s$ and $\delta_{1988}=-46°\ 22'\ 15''$, and lies at a distance of approximately 7 core radii from the cluster centre (Figure 2.1). The observing log for the TI data is given in Table 2.4. Observations were secured using filters which emulate the Johnson B and V filters, and the Kron-Cousins I filter.

The second data set analyzed, also secured at the 2.5 metre Dupont telescope at Las Campanas Observatory, was obtained on the nights of May 22/23, May 27/28 and May 29/30 1990. The observers were again G.G. Fahlman and I.B. Thompson. This data set will be referred to as the *TEK data*, and the observations will have the prefix *nn*, standing for nineteen ninety, for the rest of this thesis. A C100 Tektronix CCD was used as a detector, which had the characteristics shown in Table 2.1. The telescope configuration gave a plate scale of 0.29 *arcsec* per pixel, giving a total field area of approximately $2'\,29'' \times 2'\,29''$. The TEK cluster field is located at the centre of NGC 3201 (Figure 2.1), and has coordinates $\alpha_{1950}=10^h\ 15^m\ 34^s$ and $\delta_{1950}=-46°\ 09'\ 42''$. The observing log for the TEK data is given in Table 2.5. Observations were secured using filters that emulate the Johnson U, B, and V filters.

TABLE 2.1: Characteristics of the TEK and TI CCDs

Property	TI	TEK
Manufacturer	Texas Instruments	Tektronix
Pixel Size[2]	15 microns	27 microns
Dimensions	800 × 800 pixels	512 × 512 pixels
Read Out Noise[1]	12 e pixel^{-1}	8 e pixel^{-1}
Gain[1]	2.1 e ADU^{-1}	2 e ADU^{-1}
Limit of Linearity[1]	25000 ADU	32000 ADU

Notes to Table 2.1:
1) G.G. Fahlman, Private Communication
2) CTIO Observer's manual

Throughout this thesis I adopt the convention that U, B and V represent the Johnson system, while I represents the Kron-Cousins system. By 'standard system' I am referring to either the Johnson *UBV* and/or the Kron-Cousins I system.

2.4 Preprocessing of Data

2.4.1 TI Data

The CCD frames had been previously debiased, but not flat fielded. Three dome flat-fields were produced by combining several individual flats, see observations *nee*177 → *nee*191 and *nee*276 → *nee*293. The flats were combined, using a median filter to aid the removal of cosmic ray strikes, and normalized to a value of unity. The data frames were divided through by the appropriate flat field, and trimmed to a size of 798 × 794 pixels to remove overscan regions. The B and V frames showed localized regions where the flat fielding had been poor; the mean sky level being 918 in the field and 754 in the worst region of the B frame. This may be attributable to problems with the CCD temperature at the start and finish of the run on the night of May 22/23; the CCD may not have fully cooled, thus causing the effect. (The quantum efficiency of a CCD is very sensitive to temperature, and a non uniform temperature distribution could have caused this effect.) It is also possible that the colour-temperature of the illumination, as discussed in §2.1, may have had an effect, the spectral sensitivity changing rapidly in the poor regions.

Fringing is an effect which manifests itself as a ripple pattern on a frame due to interference in the silicon layer of the chip. No fringing was apparent on any of the frames.

2.4.2 TEK Data

The CCD frames had not been debiased and no bias frames had been taken. The frames were debiased by evaluating the mean ADU value in the overscan region of the frame and subtracting this value from every pixel in the frame. It is not expected that the bias will show appreciably structure over the frame, so this method of debiasing should be valid.

A *U* dome flat was constructed, as above, using seven frames. Dome flats for *B* and *V* had already been constructed at the telescope by using the median of five frames. The data frames were divided through by the appropriate flat field and trimmed to a size of 503 $\times$ 511 pixels to remove overscan regions. No fringing was apparent on any of the frames.

2.5 Production of Program Frames

2.5.1 Classification of Observations

The observations consist of essentially three different types of fields. What I shall refer to as a *program field* is a field in the cluster, whereas a *background field* is a field located near the cluster, but devoid of cluster stars. The third type of field I refer to is a *standard field*, which contains stars of known magnitudes which are used in the primary calibration.

2.5.2 TI Data

Where possible, frames were averaged together using the AVSIGCLIP routine in IRAF. This will average frames together, rejecting pixels which deviate from the mean by more than a specified number of standard deviations. Obviously, when only two frames were averaged, it was not possible to apply the AVSIGCLIP routine.

Combining frames changes the read out noise and gain of the new frame. The DAOPHOT user's manual (Stetson 1987a) gives the following formulae for when frames are averaged together

$$\begin{aligned} \text{Gain for N frames} &= \text{N} \times \text{Gain for 1 frame} \\ \text{Read out noise for N frames} &= \frac{\text{r/o noise for 1 frame}}{\sqrt{\text{N}}}. \end{aligned} \tag{2.1}$$

Gains and read out noise were calculated for each of the new program frames, by the use of equation 2.1. The IRAF task IMEXAMINE was used to calculate the FWHM of the stellar images on the frames, and the standard deviation of a sample of pixels constituting the sky. These results, for the TI program field frames, are summarized in Table 2.2.

TABLE 2.2: Characteristics of the TI program field frames

	No. of Constituent Frames	Exp. Time per Frame (seconds)	RON (e pixel^{-1})	Gain (e ADU^{-1})	Sky σ (ADU)	FWHM (arcsecs)
B	2	900	8.49	4.2	26	1.2
V	3	600	6.93	6.3	19	1.3
I	5	300	5.37	10.5	16	0.9

2.5.3 TEK Data

All frames were first debiased and flat fielded. Frames were combined together to increase the signal to noise ratio, as for the TI data, where possible. Characteristics of the three TEK program field frames built are shown in Table 2.3.

TABLE 2.3: Characteristics of the TEK program field frames

	No. of Constituent Frames	Exp. Time per Frame (seconds)	RON (e pixel^{-1})	Gain (e ADU^{-1})	Sky σ (ADU)	FWHM (arcsecs)
U	1	300	8.0	2.0	9	1.4
B	7	15	3.02	14	5.3	1.2
V	9	15	2.67	18	9.2	1.2

2.6 DAOPHOT

DAOPHOT (Stetson 1987b) is a suite of routines written specifically for the reduction of CCD frames containing crowded images of star fields. Each star will produce a point-spread function (PSF)[1] on the frame, the PSF of a star being much larger than its theoretical diffraction pattern (King 1971). The PSF is determined by the phenomena of atmospheric refraction, diffraction and scattering, as well as instrumental diffraction and scattering, it may also depend on telescope guiding errors. Due to the many variable factors, the PSF from one frame to the next will be different, making invalid the use of a universal PSF within a data set. A PSF has to be built for each frame on which profile-fitting photometry is required. DAOPHOT models the PSF by first fitting the central regions of a stellar profile with an analytic bivariate Gaussian function in

[1] The point-spread function is the two-dimensional brightness distribution produced on the focal plane of the detector by an unresolved source.

which the Gaussian acts as a first order approximation to the profile, and then a look up table of residuals from the Gaussian is calculated. Other programs along similar lines (*e.g.* Penny and Dickens 1986, Peterson *et al.* 1978, and Buonanno *et al.* 1983) model a PSF by using a flexible analytical function. There are advantages and disadvantages to both methods, and I refer the interested reader to Stetson (1987b) for a fuller discussion of these matters. A typical reduction of a frame using DAOPHOT involves first 'building' a PSF, using the least crowded stars on the frame as prototypes. The stars on the frame are then 'found' and split into groups, this being necessary because the reduction time for a group of N stars is $O(N^3)$, where as if the group is split up into ν subgroups, the reduction time is $O(N^3/\nu^2)$ (Stetson 1987b). DAOPHOT will simultaneously fit the stars within a group, using the PSF as the fitting profile. The stars thus fitted are subtracted from the frame, leaving stars which were 'missed' on the first find due, probably, to crowding. The finding routine is again employed to find the missed stars, and they are grouped and fitted. The two files containing the stars are concatenated and a final simultaneous fit is performed. This general procedure is what I will refer to as a *standard reduction* for the rest of this thesis.

After a standard reduction all of the recovered stars have profile-fitting magnitudes, which I shall refer to as ALLSTAR magnitudes for the rest of this thesis. The name ALLSTAR comes from a routine in DAOPHOT which groups and fits profiles to stars. The ALLSTAR magnitudes need to be calibrated to a standard system for much of the analysis.

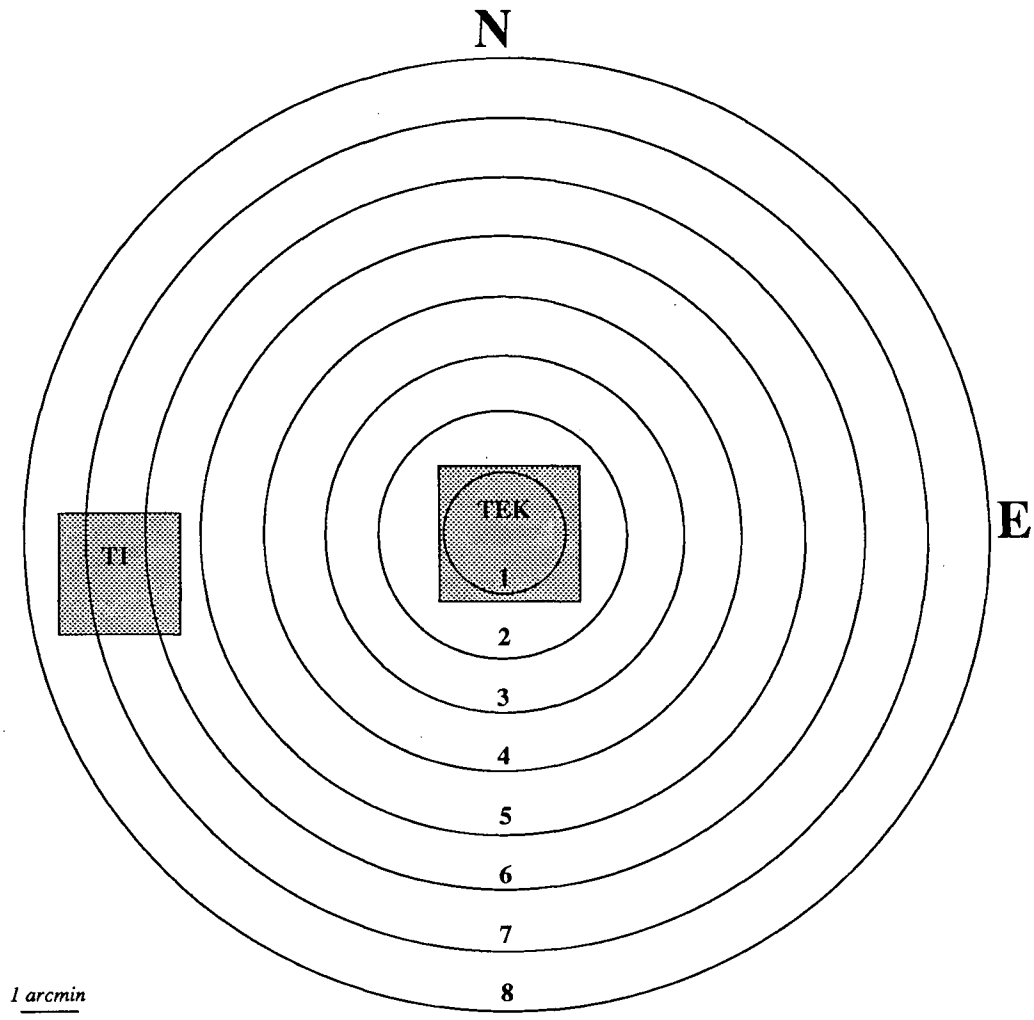

FIGURE 2.1. Location of the TI and TEK fields in NGC 3201

The location and relative sizes of the TI and TEK fields are shown. Concentric annuli indicate core radii. The core radius is 1.58 pc which, at the distance of NGC 3201, is equivalent to an angular width of 64 *arcsec*. The limiting radius, r_t, of NGC 3201 is 52.4 pc, which is equivalent to 33 core radii.

TABLE 2.4: Observing log for the TI data set

Object	Observation Number	Filter	Exposure (seconds)	Universal Time
		Night of May 22/23		
B dome flats	*nee*177 → *nee*191	*B*	90	< 23:17
Program field	*nee*195	*I*	20	23:17
Program field	*nee*196	*I*	600	23:20
Program field	*nee*197	*I*	600	23:27
Program field	*nee*198	*I*	600	23:34
Program field	*nee*199	*I*	600	23:45
Program field	*nee*200	*I*	600	23:52
Program field	*nee*201	*I*	600	23:58
A & L Stnds.	*nee*202	*I*	20	00:05
A & L Stnds.	*nee*203	*I*	20	00:09
A & L Stnds.	*nee*204	*B*	20	00:30
A & L Stnds.	*nee*205	*B*	60	00:32
Program field	*nee*206	*B*	60	00:36
Program field	*nee*207	*B*	900	00:43
Program field	*nee*208	*B*	900	01:00
Program field	*nee*209	*V*	60	01:29
Program field	*nee*210	*V*	600	01:31
Program field	*nee*211	*V*	600	01:43
Program field	*nee*212	*V*	600	01:54
PG1323 - A & B	*nee*213	*V*	5	02:16
PG1323 - C	*nee*214	*V*	20	02:26
PG1323	*nee*215	*V*	20	02:33
PG1323	*nee*216	*B*	20	02:37
PG1323	*nee*217	*I*	20	02:40
PG1323 - C	*nee*218	*I*	20	02:44
PG1323 - C	*nee*219	*B*	20	02:48
PG1323 - A & B	*nee*220	*B*	20	02:56
PG1323 - A & B	*nee*221	*I*	20	02:59
SA110 AM/AN/AO	*nee*250	*B*	20	08:19
SA110 AM/AN/AO (Focus)	*nee*251	*B*	20	08:23
SA110 AM/AN/AO	*nee*252	*V*	20	08:27

TABLE 2.4: (Continued) Observing log for the TI data set

Object	Observation Number	Filter	Exposure (seconds)	Universal Time
SA 110 AM/AN/AO	*nee*253	*B*	20	08:31
SA110 AM/AN/AO	*nee*254	*I*	20	08:35
SA110 AL	*nee*255	*I*	20	08:38
SA110 AL	*nee*256	*I*	10	08:43
SA110 AL	*nee*257	*B*	20	08:45
SA110 AL	*nee*258	*V*	20	08:48
SA110 CD & CC	*nee*259	*V*	15	09:21
SA110 CD & CC	*nee*260	*I*	10	09:25
SA110 CD & CC	*nee*261	*B*	20	09:30
SA110 CD & CC	*nee*262	*V*	20	09:33
SA110 CD & CC	*nee*263	*I*	10	09:37
SA110 CE & CF	*nee*264	*I*	10	09:43
SA110 CE & CF	*nee*265	*I*	5	09:45
SA110 CE & CF	*nee*266	*B*	20	09:47
SA110 CE & CF	*nee*267	*V*	20	09:50
SA113 492/493/495	*nee*268	*V*	10	09:54
SA113 492/493/495	*nee*269	*V*	10	09:59
SA113 492/493/495	*nee*270	*I*	5	10:01
SA113 492/493/495	*nee*271	*B*	10	10:04
V dome flats	*nee*276 → *nee*284	*V*	30	>10:04
I dome flats	*nee*285 → *nee*293	*I*	10	>10:04
	Night of May 23/24			
PG0918 - D	*nee*294	*I*	4	22:51
PG0918 - B	*nee*295	*I*	5	22:53
PG0918 - C	*nee*296	*I*	5	22:55
PG0918 - A	*nee*297	*I*	5	22:56
PG0918	*nee*298	*I*	5	22:58
PG0918	*nee*299	*B*	20	23:01
PG0918 - D	*nee*300	*B*	20	23:04
PG0918 - B	*nee*301	*B*	20	23:06
PG0918 - C	*nee*302	*B*	20	23:08
PG0918 - A	*nee*303	*B*	40	23:10
PG0918 - A	*nee*304	*V*	30	23:13
PG0918	*nee*305	*V*	20	23:16

TABLE 2.4: (Continued) Observing log for the TI data set

Object	Observation Number	Filter	Exposure (seconds)	Universal Time
PG0918 - D	*nee*306	*V*	20	23:18
PG0918 - B	*nee*307	*V*	30	23:20
PG0918 - C	*nee*308	*V*	30	23:22
Program field	*nee*309	*I*	30	23:50
Program field	*nee*310	*I*	300	23:52
Program field	*nee*311	*I*	300	00:08
Program field	*nee*312	*I*	300	00:15
Program field	*nee*313	*I*	300	00:21
Program field	*nee*314	*I*	300	00:28
Program field	*nee*315	*I*	300	00:34
Program field	*nee*316	*V*	300	00:42
Program field	*nee*317	*B*	300	00:50
Background field	*nee*318	*B*	120	01:07
Background field	*nee*319	*B*	900	01:11
Background field	*nee*320	*V*	120	01:29
Background field	*nee*321	*V*	600	01:36
Background field	*nee*322	*I*	60	01:56
Background field	*nee*323	*I*	450	02:00
Background field	*nee*324	*I*	450	02:08
Background field	*nee*325	*I*	450	02:17
Background field	*nee*326	*I*	450	02:26
PG1323 - A & B	*nee*336	*B*	20	04:00
PG1323	*nee*337	*B*	20	04:04
PG1323	*nee*338	*V*	15	04:07
PG1323 - A & B	*nee*339	*V*	15	04:09
PG1323 - A & B	*nee*340	*I*	5	04:12
PG1323	*nee*341	*I*	5	04:14
SA110 AM/AN/AO	*nee*366	*I*	5	08:31
SA110 AL	*nee*367	*I*	5	08:34
SA110 AL	*nee*368	*V*	20	08:37
SA110 AM/AN/AO	*nee*369	*V*	20	08:39
SA110 AM/AN/AO	*nee*370	*B*	20	08:42
SA110 AL	*nee*371	*B*	20	08:44
SA110 CE, CF	*nee*372	*B*	20	08:48

TABLE 2.4: (Continued) Observing log for the TI data set

Object	Observation Number	Filter	Exposure (seconds)	Universal Time
SA110 CC, CD	*nee*373	*B*	20	08:51
SA110 CC, CD	*nee*374	*V*	20	08:53
SA110 CE, CF	*nee*375	*V*	20	08:55
SA110 CE, CF	*nee*376	*I*	10	08:58
SA110 CC, CD	*nee*377	*I*	10	09:00
SA112 805	*nee*378	*I*	10	09:06
SA112 805	*nee*379	*V*	20	09:09
SA112 805	*nee*380	*V*	10	09:12
SA112 805	*nee*381	*B*	10	09:15

Notes to Table 2.4:
A & L Stnds: Alcaino and Liller (1984) Standard stars u, w, t and x
PG0918: Palomar Green Survey, Observatory standard (I. Thompson, Private Communication)
PG1323: Palomar Green Survey, Observatory standard (I. Thompson, Private Communication)
PG1323 - A: Noted to be variable; not used in the calibration.
SA110: Standard area, Landolt (1973)
SA112: Standard area, Landolt (1973)
SA113: Standard area, Landolt (1973)

TABLE 2.5: Observing log for the TEK data set

Object	Observation Number	Filter	Exposure (seconds)	Universal Time
		May 22/23		
Median of 5 *B* dome flats	None	*B*	60	< 22:25
Median of 5 *V* dome flats	None	*V*	10	< 22:25
U dome flats	*nn*1 → *nn*7	*U*	10, 15, 20, 25, 35, 50, 65	22:25 →22:30
		Night of May 27/28		
A & L Stnds.	*nn*299	*V*	60	23:38
A & L Stnds.	*nn*300	*V*	300	23:44
A & L Stnds.	*nn*301	*V*	300	23:52
A & L Stnds.	*nn*302	*V*	30	23:59
A & L Stnds.	*nn*303	*B*	30	00:02
A & L Stnds.	*nn*304	*B*	300	00:04
A & L Stnds.	*nn*305	*B*	300	00:12
A & L Stnds.	*nn*306	*U*	600	00:29
Program field	*nn*307	*U*	300	00:46
Program field	*nn*308	*B*	15	00:54
Program field	*nn*309	*B*	15	00:56
Program field	*nn*310	*B*	15	00:57
Program field	*nn*311	*B*	15	00:58
Program field	*nn*312	*B*	15	00:59
Program field	*nn*313	*B*	15	01:00
Program field	*nn*314	*B*	15	01:00
Program field	*nn*315	*B*	15	01:01
Program field	*nn*316	*B*	15	01:01
Program field	*nn*317	*B*	15	01:02
Program field	*nn*318	*B*	15	01:02
Program field	*nn*319	*B*	15	01:03
Program field	*nn*320	*V*	15	01:05
Program field	*nn*321	*V*	15	01:08
Program field	*nn*322	*V*	15	01:08
Program field	*nn*323	*V*	15	01:09
Program field	*nn*324	*V*	15	01:10
Program field	*nn*325	*V*	15	01:11

TABLE 2.5: (Continued) Observing log for the TEK data set

Object	Observation Number	Filter	Exposure (seconds)	Universal Time
Program field	*nn*326	*V*	15	01:20
Program field	*nn*327	*V*	15	01:21
Program field	*nn*328	*V*	15	01:21
Program field	*nn*329	*V*	15	01:22
Program field	*nn*330	*V*	15	01:23
	Night of May 29/30			
G162-66	*nn*355	*U*	10	23:13
G162-66	*nn*356	*U*	10	23:14
G162-66	*nn*357	*B*	5	23:16
G162-66	*nn*358	*B*	5	23:17
G162-66	*nn*359	*V*	5	23:19
G162-66	*nn*360	*V*	5	23:21
Program field	*nn*361	*V*	20	23:43
Program field	*nn*362	*V*	20	23:51
Program field	*nn*363	*V*	20	23:53
Program field	*nn*364	*B*	20	23:55
Program field	*nn*365	*B*	20	23:56
Program field	*nn*366	*B*	20	23:58
Program field	*nn*367	*B*	20	23:59
Program field	*nn*368	*B*	20	00:00
Program field	*nn*369	*U*	300	00:03
Program field	*nn*370	*U*	300	00:10
Cen A 3/6/9	*nn*378	*V*	5	01:24
Cen A 3/6/9	*nn*379	*V*	5	01:26
Cen A 3/6/9	*nn*380	*B*	5	01:27
Cen A 3/6/9	*nn*381	*B*	5	01:28
Cen A 3/6/9	*nn*382	*U*	100	01:28
Cen A 3/6/9	*nn*383	*U*	100	01:33
Cen A 2/5/8	*nn*384	*U*	100	01:39
Cen A 2/5/8	*nn*385	*U*	100	01:45
Cen A 2/5/8	*nn*386	*B*	5	01:49
Cen A 2/5/8	*nn*387	*B*	5	01:51
Cen A 2/5/8	*nn*388	*V*	5	01:52
Cen A 2/5/8	*nn*389	*V*	5	01:54

TABLE 2.5: (Continued) Observing log for the TEK data set

Object	Observation Number	Filter	Exposure (seconds)	Universal Time
PG1323	*nn*390	*V*	20	02:02
PG1323	*nn*391	*V*	20	02:04
PG1323	*nn*392	*B*	20	02:06
PG1323	*nn*393	*B*	20	02:08
PG1323	*nn*394	*U*	200	02:10
PG1323	*nn*395	*U*	150	02:15
SA113 492/493/495	*nn*435	*U*	100	09:41
SA113 492/493/495	*nn*436	*U*	100	09:43
SA113 492/493/495	*nn*437	*B*	5	09:47
SA113 492/493/495	*nn*438	*B*	5	09:48
SA113 492/493/495	*nn*439	*V*	5	09:49
SA113 492/493/495	*nn*440	*V*	5	09:50
Feige 108	*nn*441	*V*	5	09:53
Feige 108	*nn*442	*V*	5	09:54
Feige 108	*nn*443	*B*	5	09:55
Feige 108	*nn*444	*B*	5	09:58
Feige 108	*nn*445	*U*	20	10:01
Feige 108	*nn*446	*U*	20	10:02
SA112 805 & 822	*nn*447	*U*	20	10:09
SA112 805 & 822	*nn*448	*U*	40	10:10
SA112 805 & 822	*nn*449	*B*	5	10:11
SA112 805 & 822	*nn*450	*B*	5	10:12
SA112 805 & 822	*nn*451	*V*	5	10:13
SA112 805 & 822	*nn*452	*V*	4	10:14
SA112 805 & 822	*nn*453	*V*	4	10:15

Notes to Table 2.5:
A & L Stnds: Alcaino and Liller (1984), Standard stars u, w, t and x
G162-66: Giclas star, see Landolt (1973)
Cen A (NGC 5128), See Graham (1981)
PG1323: Palomar Green Survey, Observatory standard (I. Thompson, Private Communication)
Feige 108: See Landolt (1973)
SA113: Standard area, Landolt (1973)
SA112: Standard area, Landolt (1973)

Chapter 3
CALIBRATION

3.1 *Modus Operandi*

To place the photometry system of this thesis onto a standard system, transformation equations need to be derived. If a filter system had been used for the observations which closely resembled the standard system, then one would expect the magnitudes and colours of the systems to disagree by only zero point offsets. As the filters differ, it is necessary to calculate colour terms. Below is a synopsis of the photometry calibration.

The DAOPHOT task PHOT is used to evaluate aperture magnitude values of primary standards, a primary standard being a star with a hitherto known magnitude. PHOT locates the centre of a stellar image, and integrates the flux within a radius, returning a list of magnitudes, evaluated at different radii. Errors aside, the magnitude should converge as the radius increases and all the flux in the PSF is counted. The convergence value is the aperture magnitude of the star. Having aperture magnitudes for standard stars allows for transformation equations to be derived to convert aperture magnitudes to a standard system. In deriving the transformation equations it is important to have standards with a wide range in colour to help tie down the colour term in the transformation equations. The next step in the calibration is to perform aperture photometry on *secondary standards*; uncrowded stars in the field to be calibrated. For this a single frame is used so as to avoid any ambiguity over corrections for air mass and exposure time. Having aperture magnitudes for the secondary standards will then allow the standard magnitudes of these stars to be derived.

There are both advantages and disadvantages to using long or short exposure frames to obtain secondary standards. Short exposure frames will be less crowded, but at the expense of having a lower signal to noise ratio. Long exposure frames have a higher signal to noise ratio, but are more crowded. It is not possible to increase the signal to noise in the data frames, but it is possible to reduce the effects of crowding. This can be achieved by subtracting out non-secondary standards from the frame. The secondary standards are then used to determine the new zero points in the transformation equations for profile-fitting magnitudes to standard system magnitudes. *N.b.* The colour terms in the transformation equations for aperture and profile-fitting magnitudes will not change, only the offsets change as there is a different normalization. These equations can then be applied to all the profile-fitting magnitudes to determine standard magnitudes.

3.2 Aperture Photometry Transformations for the TI Data

Primary standards were observed on both the nights of May 22/23 and May 23/24 1988, refer to Table 2.4. These stars were used to derive the parameters in the transformation equations

$$\begin{aligned}(B-V) &= \alpha_{ap} + \beta(b_{ap} - v_{ap}) \\ (V-v_{ap}) &= \gamma_{ap} + \delta(B-V) \\ (V-I) &= \epsilon_{ap} + \zeta(v_{ap} - i_{ap}).\end{aligned} \tag{3.1}$$

Many of the frames used had 'multiple exposures', where the star(s) had been observed, the telescope shifted, and then reobserved on the same frame. Where this had been done, the aperture magnitude values measured were in excellent agreement with each other, and the value adopted was the mean of the measured values. The aperture magnitude values for the primary standards were corrected to an exposure time of one second and an air mass of zero atmospheres. This is the normalization for exposure and air mass that I adopt for the remainder of this thesis. The extinction coefficients used to correct for air mass were those as used by Landolt (1983) for the Cerro-Tololo Inter-American Observatory (CTIO), these values should be appropriate to Las Campanas due to the similar climatic conditions and altitudes of the observatories. The values used were

$$\begin{aligned}Q_y &= 0.172 \\ k_1 &= 0.111 \\ k_9 &= 0.087,\end{aligned} \tag{3.2}$$

where Q_y, k_1 and k_9 are the extinctions in V, $(B-V)$ and $(V-I)$ respectively.

The parameters and errors of the fits in this chapter were determined using OPDATA (Bennett 1989). No significant second order colour terms were found in the fits, and such terms were dropped from further consideration. After an initial fit to the data, the deviation from the fit was found for each point. A cleaning procedure was employed where any point having a deviation greater than twice the standard deviation of the distribution of all the points was rejected, on the premise that the point was an outlier and did not belong to the distribution. If the distribution is normal, it is expected that approximately one point in twenty will be unfairly rejected by this procedure. The standard deviation of the distribution is calculated with outliers included, and so is larger than the intrinsic standard deviation of the distribution, thus decreasing even further the chance of a point being unfairly rejected. The data were fitted again, excluding

the outliers, which are shown as open circles (Figures 3.1 and 3.2). The fits obtained are

$$\begin{aligned}(B-V) &= 0.583 \pm 0.004 + 1.211 \pm 0.006(b_{ap} - v_{ap}) \\ (V-v_{ap}) &= -(8.6 \pm 1.5) \times 10^{-2} + 9 \times 10^{-4} \pm 1.25 \times 10^{-2}(B-V) \\ (V-I) &= 0.876 \pm 0.008 + 0.97 \pm 0.01(v_{ap} - i_{ap})\end{aligned} \tag{3.3}$$

for the night of May 22/23, and

$$\begin{aligned}(B-V) &= 0.56 \pm 0.01 + 1.205 \pm 0.015(b_{ap} - v_{ap}) \\ (V-v_{ap}) &= -(9.36 \pm 1) \times 10^{-2} - 7.1 \times 10^{-3} \pm 1 \times 10^{-2}(B-V) \\ (V-I) &= 0.885 \pm 0.008 + 0.98 \pm 0.01(v_{ap} - i_{ap})\end{aligned} \tag{3.4}$$

for the night of May 23/24.

The parameters in the fits are consistent between the two nights at a one sigma level, with the exception of the zero point in the $(B-V)$ transformation, which is only marginally inconsistent. As the program field frames being used for the secondary standards came from both nights of observation (§2.5.2), I decided to combine all of the primary standards together and obtain transformation equations applicable to aperture photometry from both nights. An initial fit was performed on the combined data set and the aforementioned cleaning procedure employed. A fit was performed on the cleaned data (Figure 3.3), and the fits obtained were

$$\begin{aligned}(B-V) &= 0.58 \pm 0.01 + 1.19 \pm 0.01(b_{ap} - v_{ap}) \\ (V-v_{ap}) &= -(9 \pm 1) \times 10^{-2} \\ (V-I) &= 0.880 \pm 0.006 + 0.975 \pm 0.008(v_{ap} - i_{ap}),\end{aligned} \tag{3.5}$$

with the colour term being dropped from the $(V - v_{ap})$ transformation; it being consistent with zero when the errors are considered. That the colour term is small is an indication that the V filter used for these observations is congruous with the Johnson system V filter.

3.3 ALLSTAR Photometry Transformations for the TI Background Field

V Calibration

To calibrate the TI V background field, a colourless transformation equation was employed, *viz.*

$$(V - v_{als}) = \gamma_{als} + \delta(B-V), \tag{3.6}$$

with δ being set equal to zero, in accordance with equations 3.5.

I determined γ_{als} in two ways. The first was to select nineteen secondary standards in the background field and perform aperture photometry on them using the shorter exposure B and V frames, *nee*318 and *nee*320. The background field was uncrowded, and it was deemed unnecessary to subtract out neighbours. Aperture magnitude values obtained were normalized, the extinction coefficients used being those given in equation 3.2. Applying equations 3.5 to the aperture magnitudes, the Johnson B and V magnitudes for the nineteen secondary standard stars were obtained. The nineteen secondary standards were identified in the ALLSTAR file resulting from the standard reduction on the TI V background field which had been binned 2×2 (see §6.2) and a plot was made of $(V - v_{als})$ against $(B - V)$, see Figure 3.4. Two points were arbitrarily rejected on the premise that they were considered to be outliers, and not to belong to the intrinsic distribution values. The mean of the remaining seventeen points gave

$$\gamma_{als} \equiv \overline{(V - v_{als})} = 4.81 \pm 0.01, \tag{3.7}$$

with the error being the standard error, given by

$$\text{standard error} = \frac{\sigma}{\sqrt{(n-1)}}, \tag{3.8}$$

where σ is the standard deviation of the distribution and n is the number of points in the distribution.

The second way in which γ_{als} was determined was to repeat the above procedure, but using the longer exposure B and V frames, *nee*319 and *nee*321, for the aperture photometry. Again, it was deemed unnecessary to subtract out neighbours. A plot of $(V - v_{als})$ against $(B - V)$ is shown in Figure 3.5. Two points were dropped from consideration in evaluating the mean value of γ_{als}. The mean of the remaining seventeen values gave

$$\gamma_{als} \equiv \overline{(V - v_{als})} = 4.787 \pm 0.006, \tag{3.9}$$

the error being the standard error.

The two values for γ_{als} are in reasonable agreement, as anticipated. The latter value of γ_{als} has considerably less scatter in it, as expected from signal to noise considerations, and I adopted this value for the calibration of the binned background V fields.

I Calibration

The I background field goes deeper than the V background field. To calibrate the I background field a colourless transformation equation,

$$\mathrm{I} = i_{als} + \eta_{als}, \tag{3.10}$$

is required, otherwise only stars found on *both* the V and I frames can be calibrated by use of equations 3.5.

Aperture photometry magnitudes were evaluated on both the short and long exposure I frames, *nee*322 and *nee*323 respectively, for the same nineteen secondary standard as used in the V background field calibration. The frames were deemed sufficiently uncrowded as not to require neighbour subtraction. Aperture magnitude values obtained were normalized, using the extinction coefficients given in equation 3.2. The aperture photometry transformation equations for the TI data, equations 3.5, were applied to obtain I magnitudes for the nineteen secondary standards, with the short and long exposure aperture magnitudes being kept distinct.

The nineteen secondary standards were identified in the ALLSTAR file which had resulted from a standard reduction on the TI I background field, which had been binned 2×2 (see §6.2), and a plot was made of $(I - i_{als})$ against $(V - I)$, see Figures 3.4 and 3.5.

A least squares fit to the data points showed that there was an insignificant colour term. That the colour term was negligible indicated that the filter used for the observations was congruous with the Kron-Cousins I filter.

Using the short exposure (60 second) background field I obtained, after the rejection of three outliers,

$$\eta_{als} \equiv \overline{(I - i_{als})} = 3.74 \pm 0.01, \tag{3.11}$$

the error being the standard error. Similarly, the long exposure (450 seconds) TI I background field led, after the rejection of three outliers, to

$$\eta_{als} \equiv \overline{(I - i_{als})} = 3.756 \pm 0.005. \tag{3.12}$$

The two values were consistent with each other at the one sigma level, but the latter, obtained using stars with a higher signal to noise, has less scatter. I adopted the latter value for the calibration of the binned TI I background fields.

3.4 ALLSTAR Photometry Transformations for the TI Program Field

3.4.1 Secondary Standards

Seventeen uncrowded stars were selected on the TI program field frames to be secondary standards. The calibration of these stars, to a standard system, was achieved in two ways; by using both long and short exposure field frames.

To reduce the effects of crowding, a standard reduction was performed on each of the above frames to produce frames that contained only the seventeen secondary standards and anything which had been missed by the standard reduction. One must realize that profile fitting is never perfect: shot noise will be left where a star has been subtracted out, due to the increased number of photons in a stellar image. The method of neighbour subtraction does have its limitations.

Aperture photometry was performed on the secondary standard stars, and the aperture magnitudes thus obtained were normalized, the extinction coefficients used being those given in equation 3.2. Two stars were lost in the short exposure calibration, due to the B frame being displaced with respect to the V and I frames. A comparison of the aperture magnitude values obtained for the fifteen stars in common is shown in Figure 3.6. One sees good agreement for the brighter secondary standards, with the scatter increasing at the fainter end. Standard magnitudes were calculated by use of equations 3.5.

3.4.2 Calibration of the TI Program Field Frames

The seventeen secondary standards from §3.4.1 were identified in the ALLSTAR files resulting from standard reductions on the TI B, V and I program fields. The transformation equations for ALLSTAR photometry are

$$\begin{aligned}
(B - V) &= \alpha_{als} + 1.19 \pm 0.01(b_{als} - v_{als}) \\
(V - v_{als}) &= \gamma_{als} \\
(V - I) &= \epsilon_{als} + 0.975 \pm 0.008(v_{als} - i_{als}).
\end{aligned} \tag{3.13}$$

Values for α_{als}, γ_{als} and ϵ_{als} were determined for each secondary standard star, and plots made of the value against the appropriate colour index, (Figures 3.7 and 3.8). Outliers deemed not to belong to the distribution, and excluded from the fit, are indicated with open circles. One expects no colour gradient if the colour coefficient is correct; this is the case.

Values obtained using the short exposure secondary standards are

$$\begin{aligned} \overline{\alpha_{als}} &= 2.13 \pm 0.01 \\ \overline{\gamma_{als}} &= 4.83 \pm 0.02 \\ \overline{\epsilon_{als}} &= 0.17 \pm 0.005, \end{aligned} \tag{3.14}$$

whilst using the long exposure secondary standards gives

$$\begin{aligned} \overline{\alpha_{als}} &= 2.13 \pm 0.01 \\ \overline{\gamma_{als}} &= 4.82 \pm 0.005 \\ \overline{\epsilon_{als}} &= 0.18 \pm 0.01. \end{aligned} \tag{3.15}$$

With errors taken into account, these two sets of values are consistent with each other at the one sigma level. I adopted the latter set of values due to the generally smaller errors, which resulted in the transformation equations

$$\begin{aligned} (B-V) &= 2.13 \pm 0.01 + 1.188 \pm 0.01(b_{als} - v_{als}) \\ (V - v_{als}) &= 4.820 \pm 0.005 \\ (V-I) &= 0.18 \pm 0.01 + 0.975 \pm 0.008(v_{als} - i_{als}) \end{aligned} \tag{3.16}$$

for ALLSTAR photometry to standard system photometry on the TI program frames.

3.4.3 Calibration of the Binned TI Program Field Frames

To calibrate the binned *V* and *I* frames, which were used to construct the luminosity function, colourless transformation equations, see §3.3, were used. The seventeen secondary standards from §3.4.1 were identified in the ALLSTAR list which had resulted from a standard reduction on the *V* and *I* frames that had been binned 2 × 2 (see §6.2). Figures 3.9 and 3.10 show plots of $(I - i_{als})$ against $(V - I)$ and $(V - v_{als})$ against $(B - V)$. Open circles indicate points which were arbitrarily considered to be outliers, and were dropped from consideration.

Using the shorter exposure program fields, yields the transformation equations

$$\begin{aligned} \gamma_{als} &= \overline{(I - i_{als})} = 3.30 \pm 0.01 \\ \eta_{als} &= \overline{(V - v_{als})} = 4.444 \pm 0.006, \end{aligned} \tag{3.17}$$

while using the longer exposure program fields gives

$$\begin{aligned} \gamma_{als} &= \overline{(I - i_{als})} = 3.274 \pm 0.004 \\ \eta_{als} &= \overline{(V - v_{als})} = 4.425 \pm 0.005. \end{aligned} \tag{3.18}$$

The values of γ_{als} and η_{als} are reasonably consistent with each other at around the two sigma level. The standard deviations of the distributions obtained using the longer exposure frames are smaller than those for the shorter ones, and therefore have better defined means. I adopted the values obtained using the longer exposure frames for the calibration of the binned program field frames.

3.5 Error Propagation in the Transformation Equations

Using the error returned along with the ALLSTAR magnitude in DAOPHOT, it is possible to propagate errors and determine the errors in the calibrated colours and magnitudes. Writing

$$(B - V) = \alpha + \beta(b_{als} - v_{als}), \tag{3.19}$$

we have, by the addition of errors in quadrature,

$$\sigma^2_{(B-V)} = \sigma^2_{\alpha} + \sigma^2_{\beta(b_{als}-v_{als})}\,. \tag{3.20}$$

Now, Bevington (1969) gives that if

$$x = \pm auv, \tag{3.21}$$

then

$$\sigma^2_x = a^2v^2\sigma^2_u + a^2u^2\sigma^2_v + 2a^2uv\sigma^2_{uv} \tag{3.22}$$

with σ_{uv} being the covariance, defined as

$$\sigma^2_{uv} = \lim_{n \to \infty} \frac{1}{n} \sum [(u_i - \overline{u})(v_i - \overline{v})]. \tag{3.23}$$

Writing

$$x = \beta(b_{als} - v_{als}) \tag{3.24}$$

and

$$\begin{aligned} a &= 1 \\ u &= \beta \\ v &= (b_{als} - v_{als}), \end{aligned} \tag{3.25}$$

the covariance in the error term can be ignored as no correlation between β and $(b_{als} - v_{als})$ is expected. Hence

$$\sigma^2_{\beta(b_{als}-v_{als})} = \beta^2\sigma^2_{(b_{als}-v_{als})} + (b_{als} - v_{als})^2\sigma^2_{\beta}. \tag{3.26}$$

Using the addition of errors in quadrature I obtain

$$\sigma^2_{(B-V)} = \sigma^2_{\alpha} + \beta^2(\sigma^2_{b_{als}} + \sigma^2_{v_{als}}) + (b_{als} - v_{als})^2\sigma^2_{\beta}, \tag{3.27}$$

which is readily evaluated. The errors for the other magnitudes and colours can be propagated similarly.

The errors shown in the colour-magnitude diagrams and colour-colour diagrams of chapter 4 are calculated as above. They essentially reflect two components, one component being a calibration error, which can be regarded as an error in coordinate labels, the other error being an intrinsic error which, as expected, increases for fainter stars.

3.6 Aperture Photometry Transformations for the TEK Data

Observations of primary standard stars were made on the night of May 29/30 1990 (see Table 2.5). Using these standards, transformation equations from aperture photometry to Johnson photometry were derived. This was achieved by performing aperture photometry on the standard stars and normalizing for air mass and exposure time. The extinction coefficients used were

$$\begin{aligned} Q_y &= 0.172 \\ k_1 &= 0.111 \\ k_3 &= 0.290, \end{aligned} \tag{3.28}$$

where Q_y, k_1 and k_3 are the extinctions in V, $(B - V)$ and $(U - B)$ respectively. The first two of these values are from Landolt (1983), while the third is from Landolt (private communication). The $(U - B)$ extinction coefficient was adopted after finding a large discrepancy between the value reported by Landolt (1983) and that in the CTIO user manual. An initial fit was performed upon the data; points which had a deviation from the initial fit greater than two standard deviations

were deemed to be outliers and dropped from consideration (Figure 3.11). The transformation equations thus derived are

$$\begin{aligned}(B-V) &= 0.379 \pm 0.007 + 1.26 \pm 0.02(b_{ap} - v_{ap}) \\ (V-v_{ap}) &= -0.80 \pm 0.01 + -0.01 \pm 0.01(B-V) \\ (U-B) &= -1.55 \pm 0.02 + 0.90 \pm 0.01(u_{ap} - b_{ap})\ .\end{aligned} \tag{3.29}$$

The colour term in the $(V - v_{ap})$ transformation equation was considered small enough to be neglected. This is a result of having a V filter that is congruous with the Johnson V filter. The colour term was dropped and the mean of the points, excluding the outliers, was found, giving the transformation equation

$$(V - v_{ap}) = -0.81 \pm 0.01. \tag{3.30}$$

3.7 ALLSTAR Photometry Transformations for the TEK Data

3.7.1 Secondary Standards

Frames *nn*362, *nn*366 and *nn*370 are short exposure TEK program field frames, acquired on the same night as the standard fields, so it is legitimate to apply equations 3.29 to normalized aperture photometry on these frames.

Thirteen secondary standard stars were chosen which were common to all three short exposure program field frames, as well as to the program field frames from the night of May 27/28 1990, which were used to build the program frames. The frames were deemed to be too crowded for aperture photometry and so a standard reduction was performed on each frame to subtract neighbours. Johnson magnitudes were derived for these stars using the transformation equations derived in §3.6.

3.7.2 Calibration of the TEK Program Field Frames

To derive the ALLSTAR to Johnson transformation, it is necessary to redetermine the zero points in the aperture transformation equations, as in §3.4.2. The thirteen secondary standards were identified in ALLSTAR file resulting from a standard reduction on the frame and values were derived for α_{als}, γ_{als} and ϵ_{als} and were plotted against a colour index (Figure 3.12). Open circles indicate points deemed as not belonging to the distribution, which were dropped from

consideration. Taking the mean and standard error of the three distributions gives

$$\begin{aligned}(B-V) &= -0.28 \pm 0.02 + 1.26 \pm 0.02(b_{als} - v_{als}) \\ (V - v_{als}) &= 1.32 \pm 0.01 \\ (U-B) &= 0.63 \pm 0.02 + 0.90 \pm 0.01(u_{als} - b_{als}).\end{aligned} \tag{3.31}$$

Errors for Johnson magnitudes and colours were propagated and evaluated as outlined in §3.5.

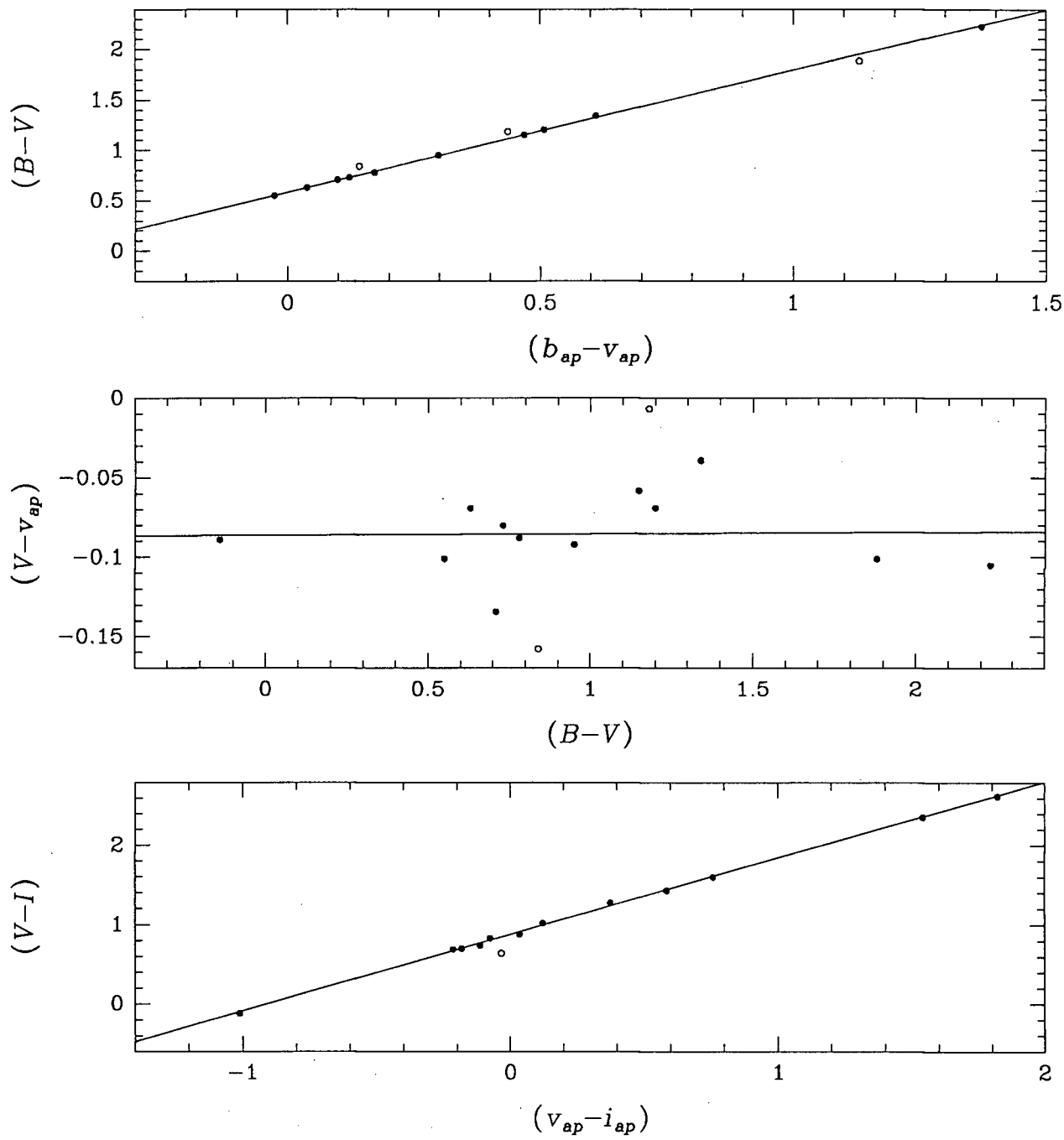

FIGURE 3.1. Aperture photometry transformations for the night of May 22/23 1988

Open circles indicate points which had deviations greater than 2σ from the fit to all the points, and were dropped from consideration, while the solid lines indicate the fits to the remaining points. The subscript *ap* refers to normalized aperture photometry magnitudes, while upper case denotes the standard system.

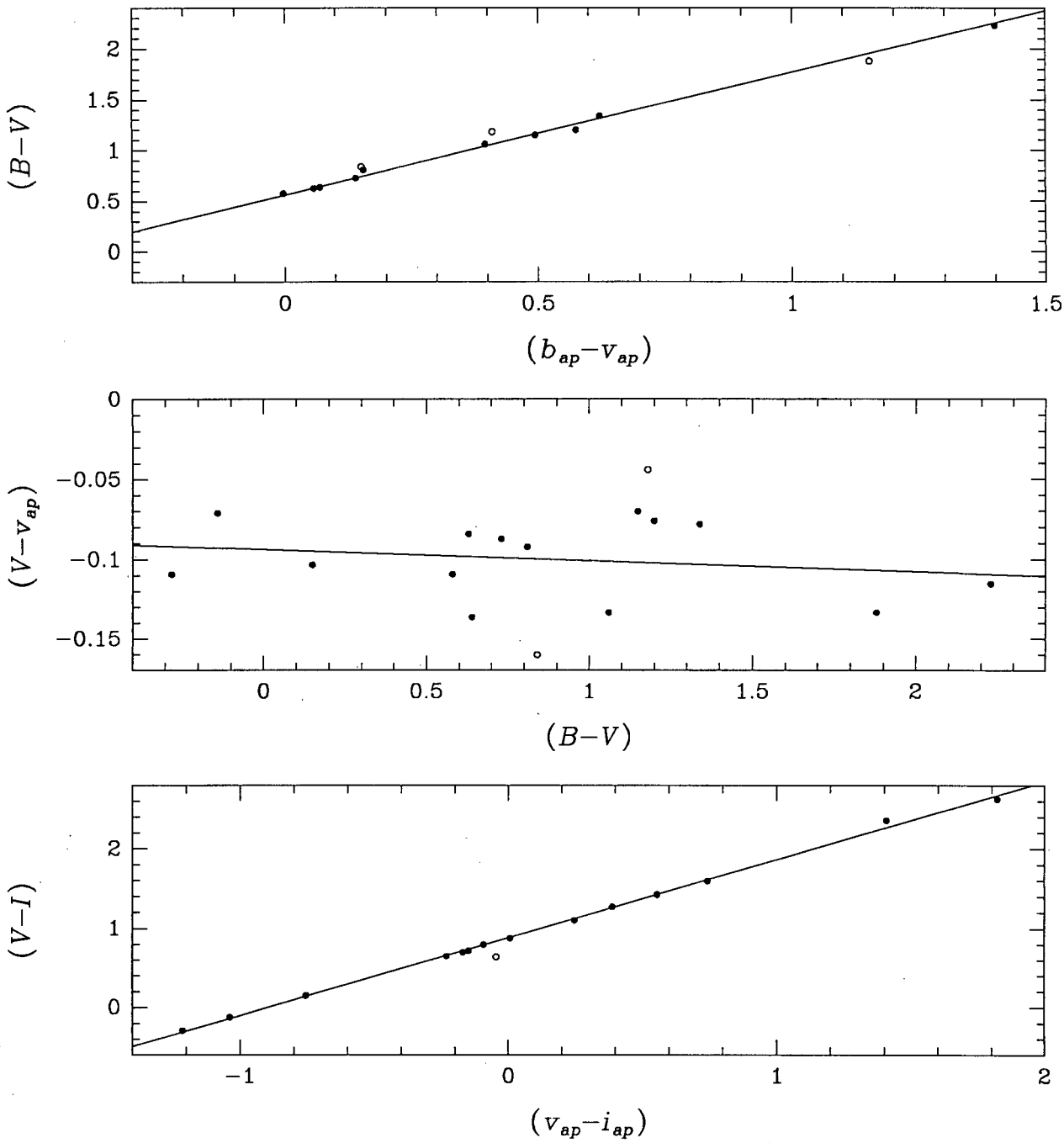

FIGURE 3.2. Aperture photometry transformations for the night of May 23/24 1988

Open circles indicate points which had deviations greater than 2σ from the fit to all the points, and were dropped from consideration while the solid lines indicate the fits to the remaining points. The subscript *ap* refers to normalized aperture photometry magnitudes, while upper case denotes the standard system.

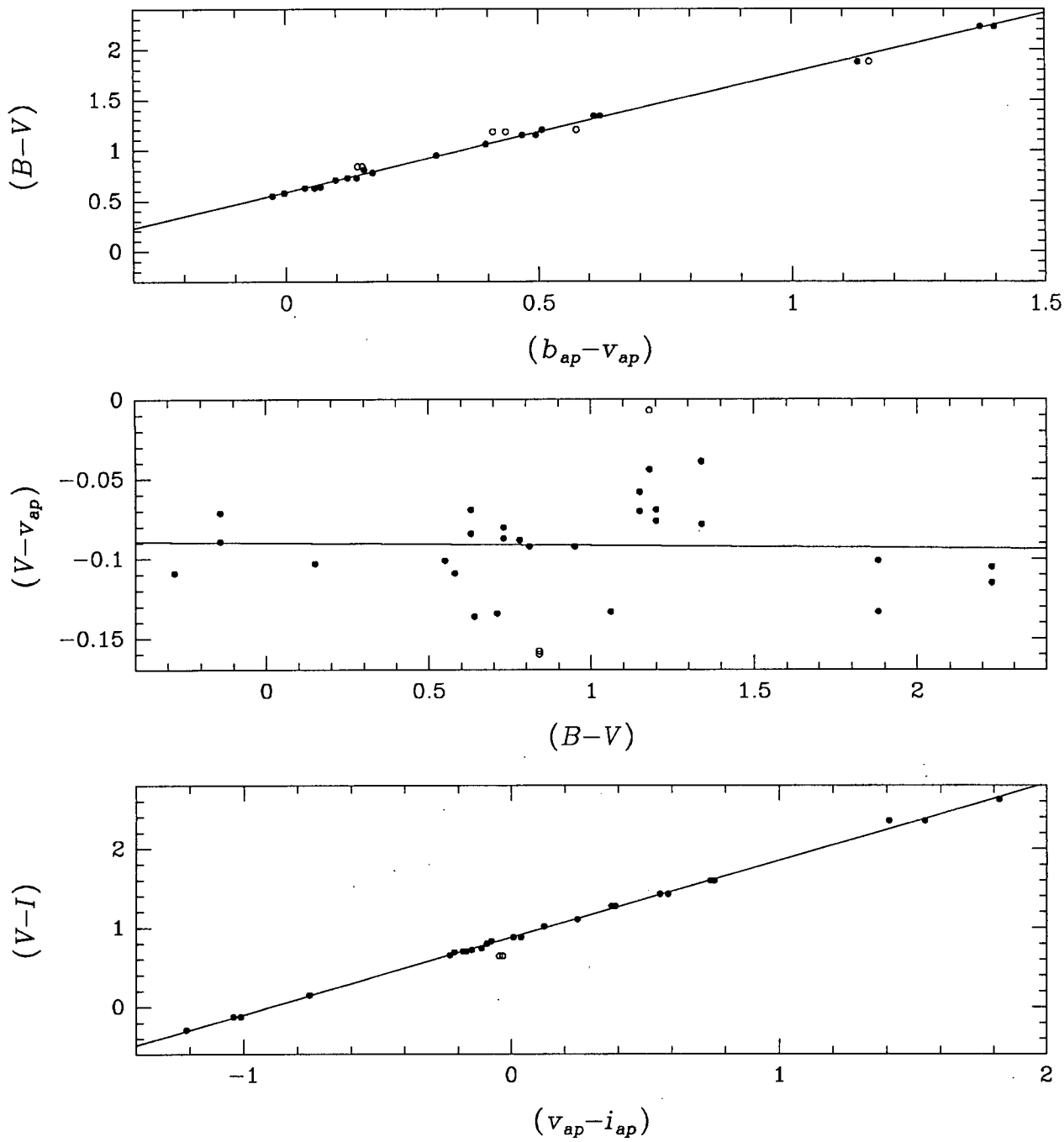

FIGURE 3.3. Aperture photometry transformations for the nights of May 22/23 and 23/24 1988

Open circles indicate points which had deviations greater than 2σ from the initial fit to all the points, and were dropped from consideration, while the solid lines indicate the fits to the remaining points. The subscript *ap* refers to normalized aperture photometry magnitudes, while upper case denotes the standard system.

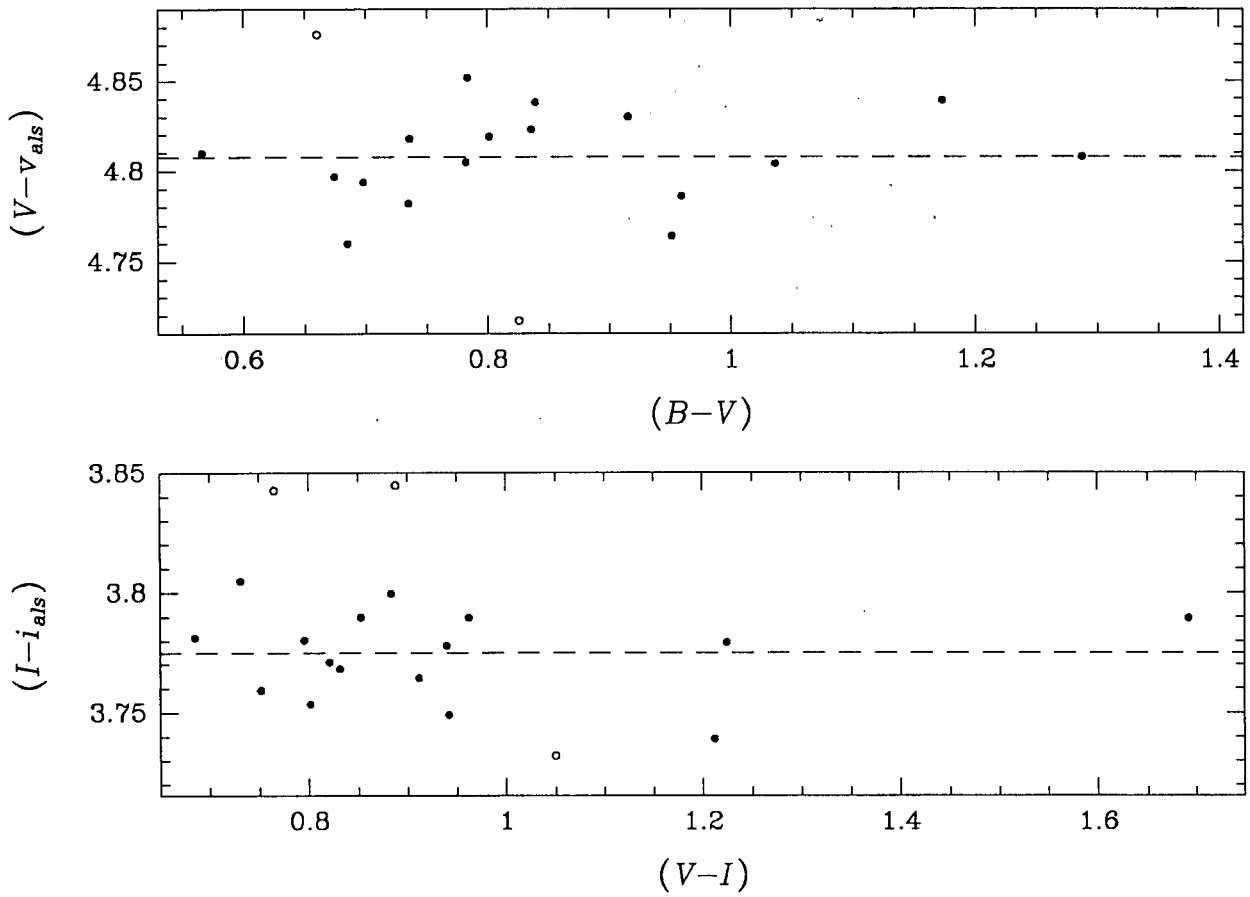

FIGURE 3.4. TI background field ALLSTAR zero points (short exposure frames)

Open circles indicate points dropped from consideration, and the dashed line indicates the mean value of the remaining points. The aperture magnitude values, used to derive the standard magnitudes, were determined using the frames *nee*318, *nee*320 and *nee*322. The subscript *als* refers to profile-fitting magnitudes, while upper case denotes the standard system.

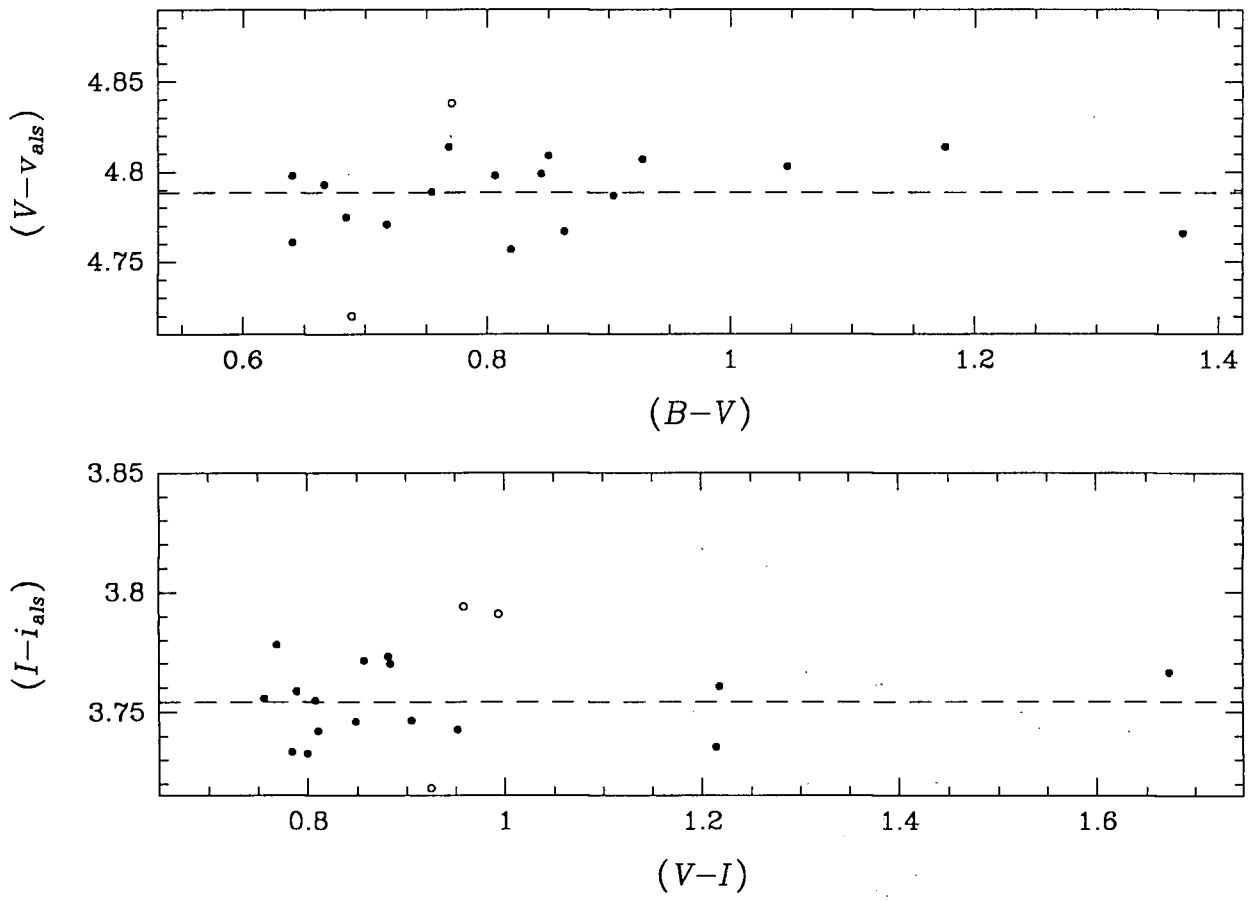

FIGURE 3.5. TI background field ALLSTAR zero points (long exposure frames)

Open circles indicate points dropped from consideration, and the dashed line indicates the mean value of the remaining points. The aperture magnitude values, used to derive the standard magnitudes, were determined using the frames *nee*319, *nee*321 and *nee*323. The subscript *als* refers to profile-fitting magnitudes, while upper case denotes the standard system.

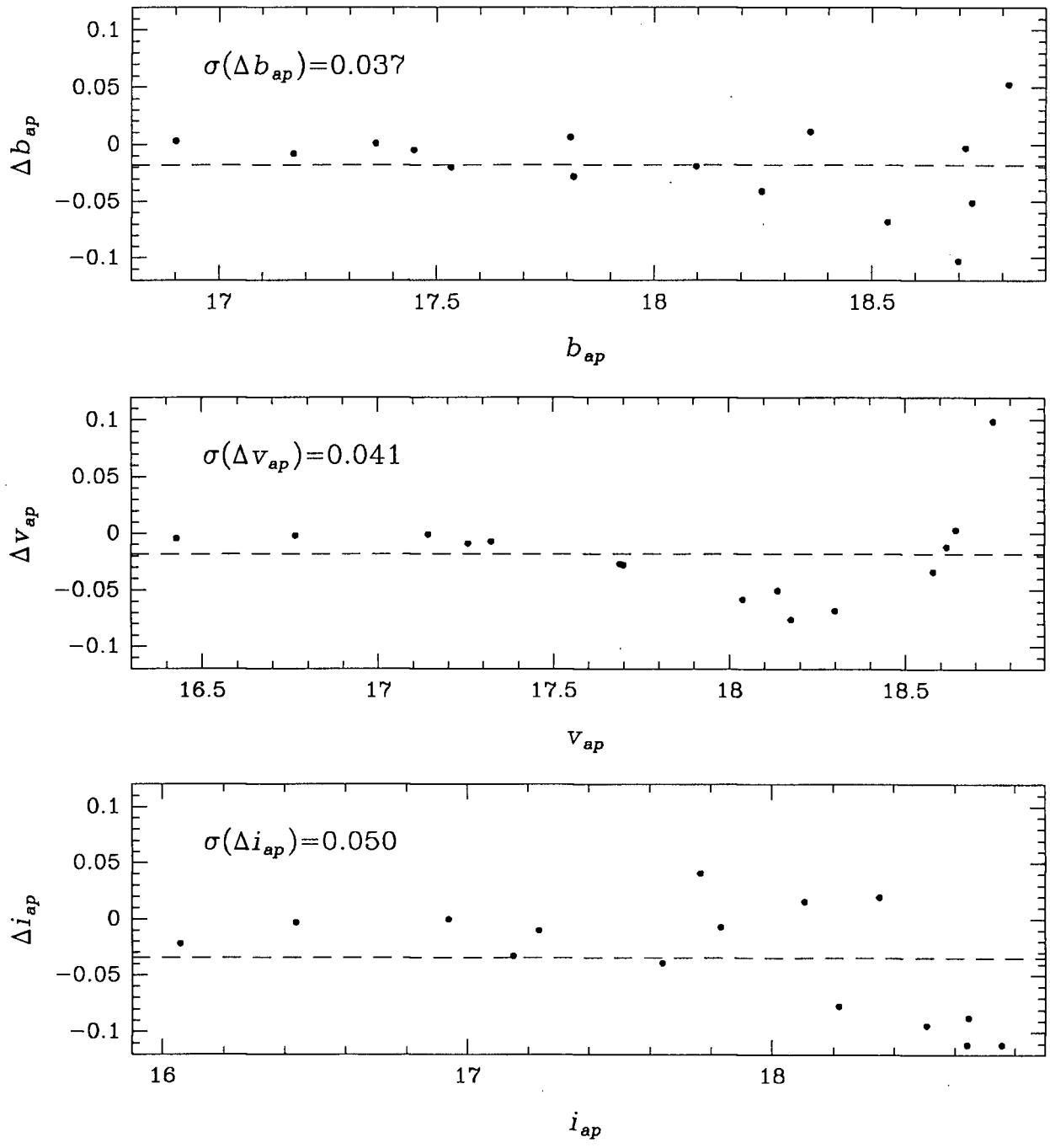

FIGURE 3.6. Comparison of aperture photometry between frames with long and short exposure times

Aperture magnitudes were normalized to an exposure time of 1 second and an air mass of zero. The difference between the magnitudes, Δ, is in the sense (long – short). The dashed lines indicate the mean values of the distributions, while their standard deviations are given in each panel.

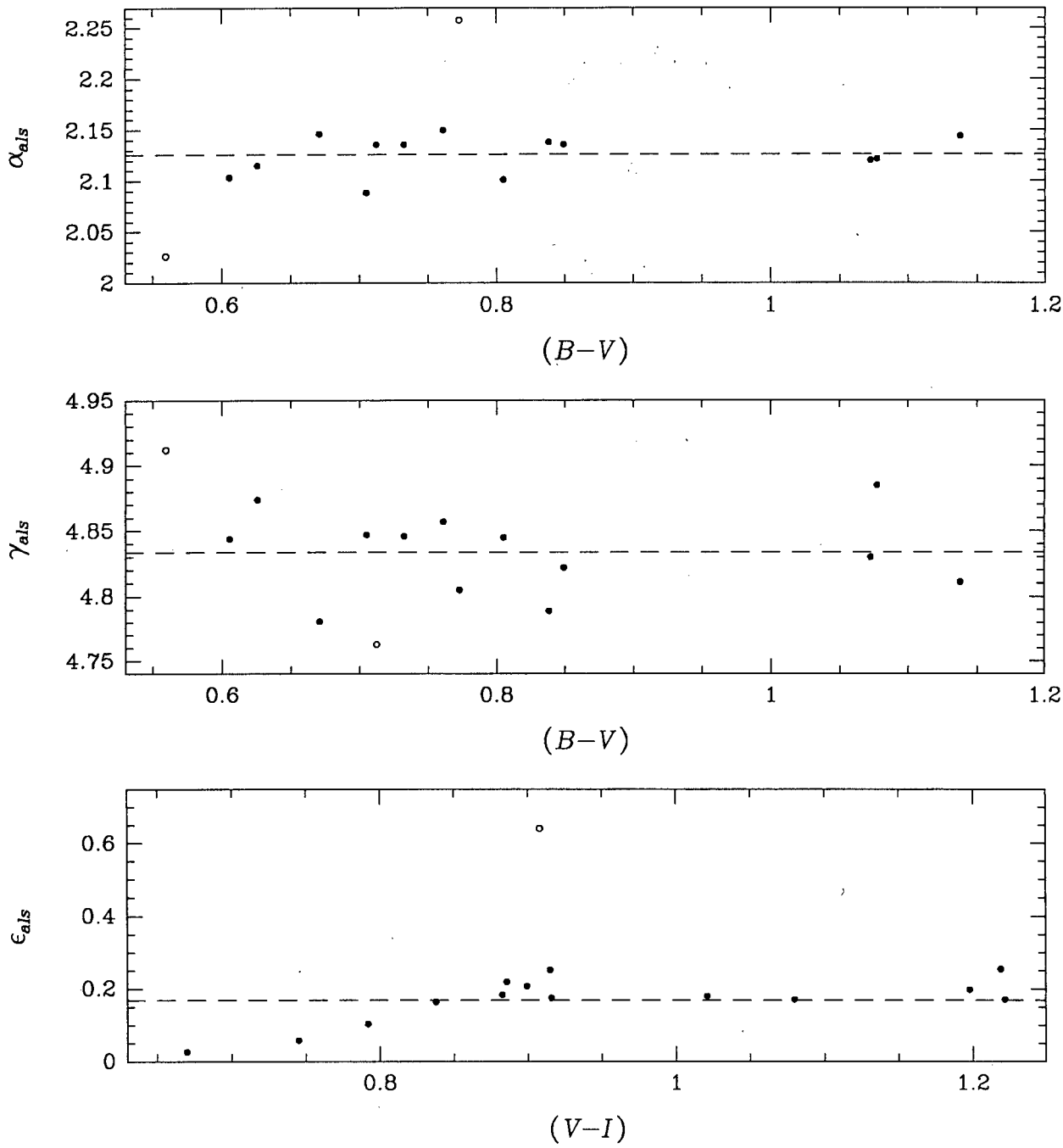

FIGURE 3.7. TI program field ALLSTAR zero points (short exposure frames)

Open circles indicate points deemed as outliers and dropped from consideration, and the dashed lines indicate mean values of the remaining points in each of the three panels. The zero points were derived using secondary standards on the TI program field frames *nee*206, *nee*209 and *nee*309. Upper case letters denote the standard system.

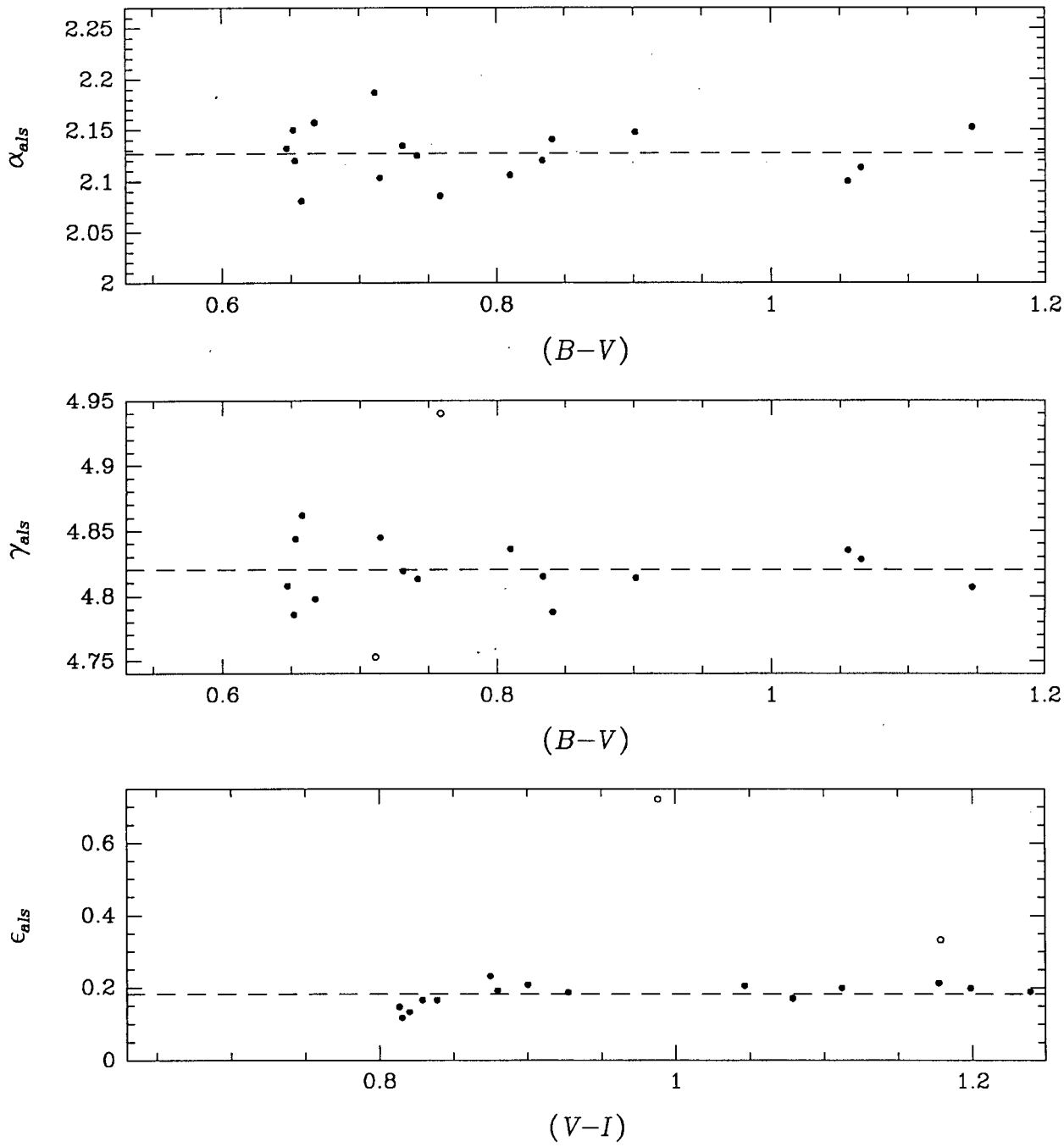

FIGURE 3.8. TI program field ALLSTAR zero points (long exposure frames)

Open circles indicate points deemed as outliers and dropped from consideration, and the dashed lines indicate mean values of the remaining points in each of the three panels. The zero points were derived using secondary standards on the program field frames *nee*207, *nee*211 and *nee*311. Upper case letters denote the standard system.

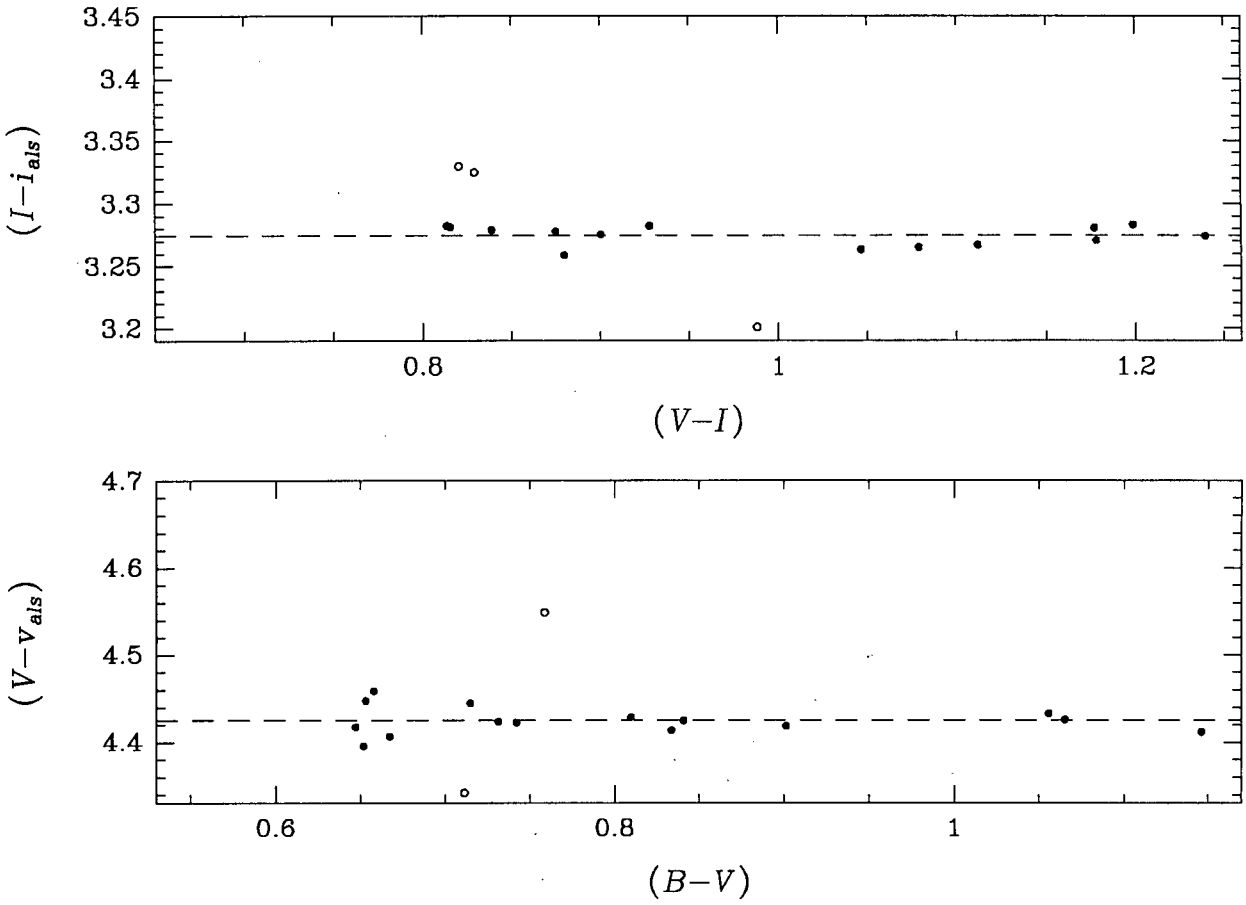

FIGURE 3.9. Colourless TI program field ALLSTAR zero points (long exposure frames)

Open circles were deemed as outliers and were dropped from consideration, and the dashed lines indicate mean values of the remaining points in each of the three panels. Aperture magnitude values were determined using the frames *nee*207, *nee*211 and *nee*311. The subscript *als* refers to profile-fitting magnitudes, while upper case is used to denote the standard system.

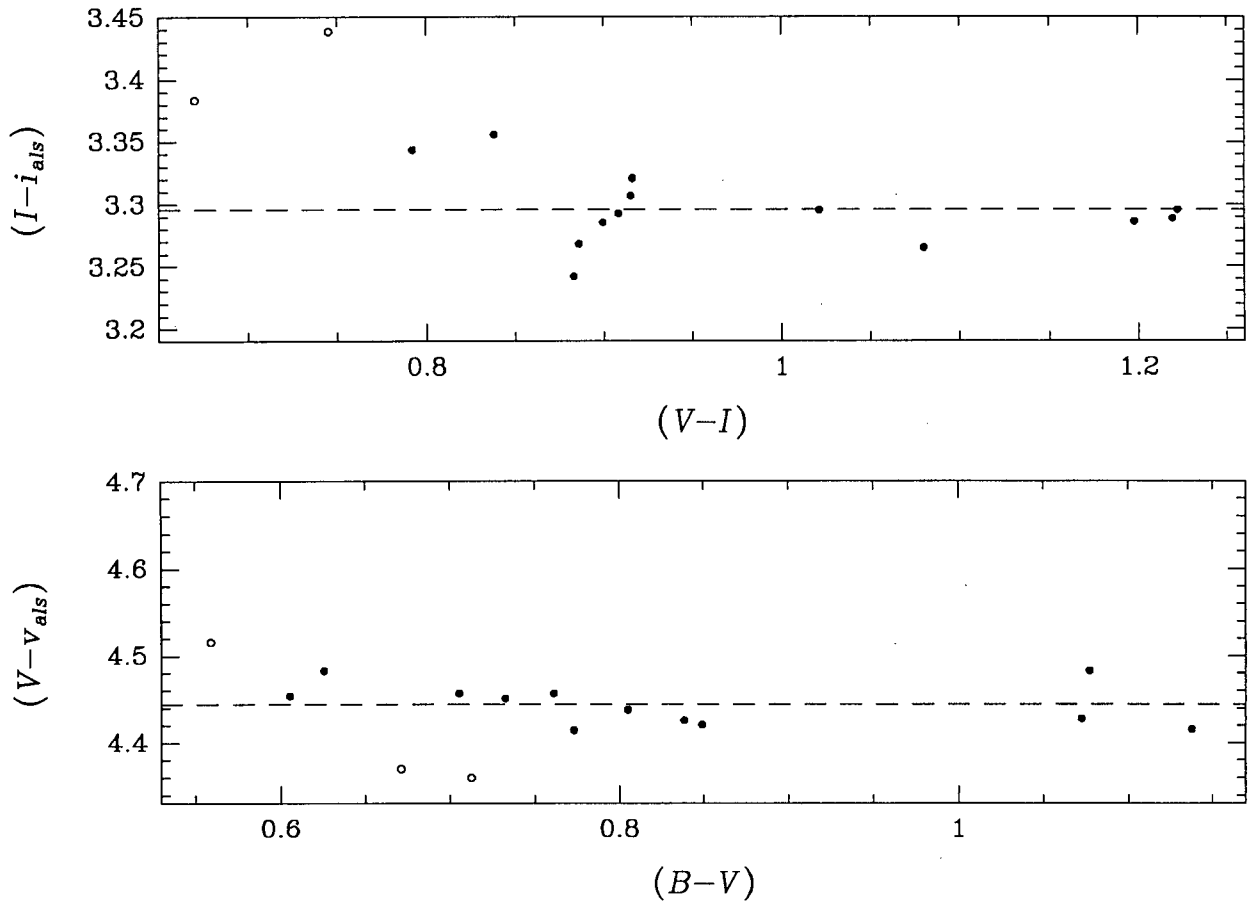

FIGURE 3.10. Colourless TI program field ALLSTAR zero points (short exposure frames)

Open circles were deemed as outliers and were dropped from consideration, and the dashed lines indicate mean values of the remaining points. Aperture magnitude values were obtained using the frames *nee*206, *nee*209 and *nee*309. The subscript *als* refers to profile-fitting magnitudes, while upper case is used to denote the standard system.

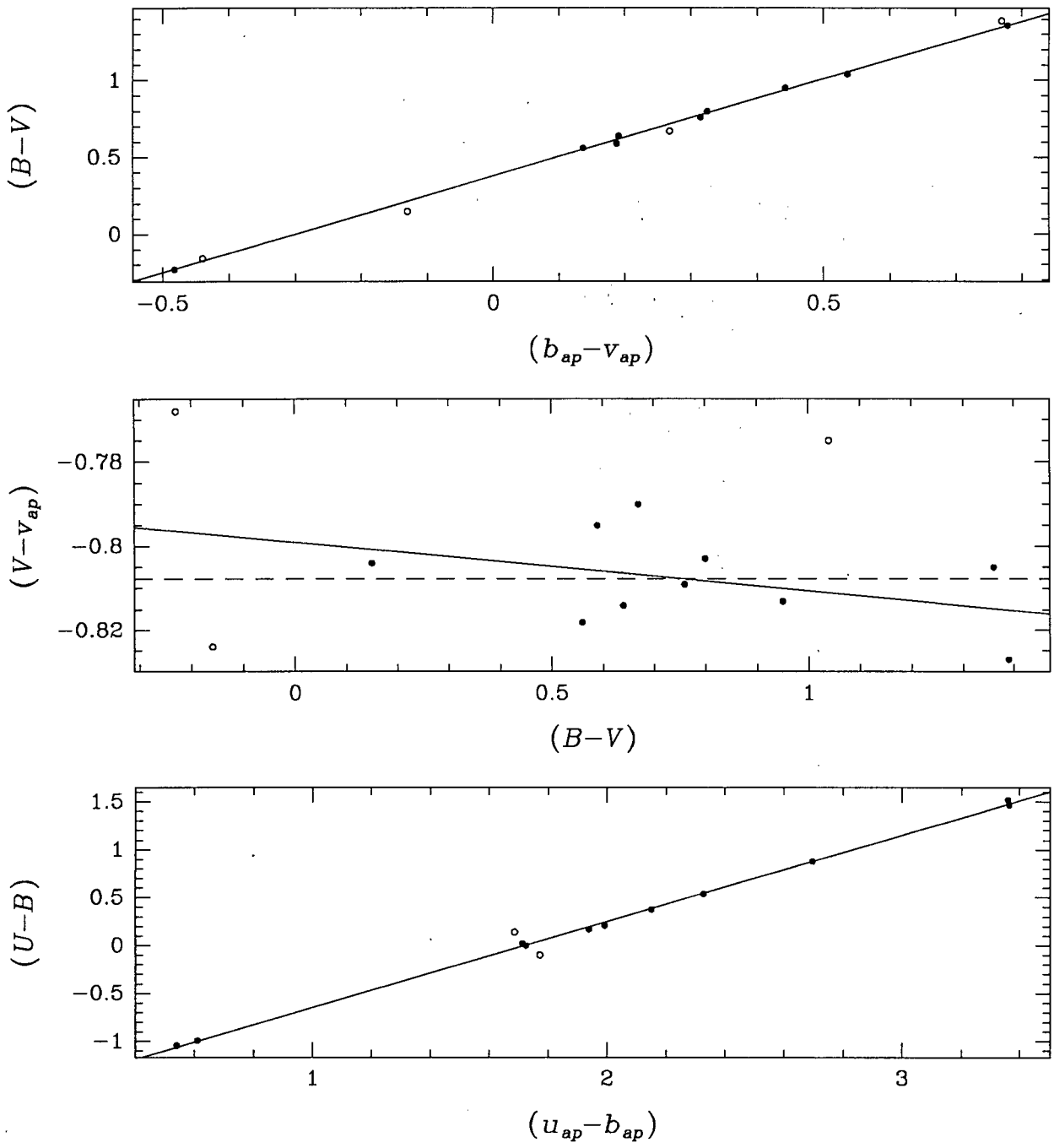

FIGURE 3.11. Aperture photometry transformations for the TEK data set

Open circles had deviations greater than 2σ from the fit to all the points, and were dropped from consideration, while the solid lines indicate the fits to the remaining points. The dashed line in the middle panel indicates the mean value of $(V - v_{ap})$ after the colour term is dropped in the fit. The subscript *ap* refers to normalized aperture photometry values, while upper case denotes the Johnson system.

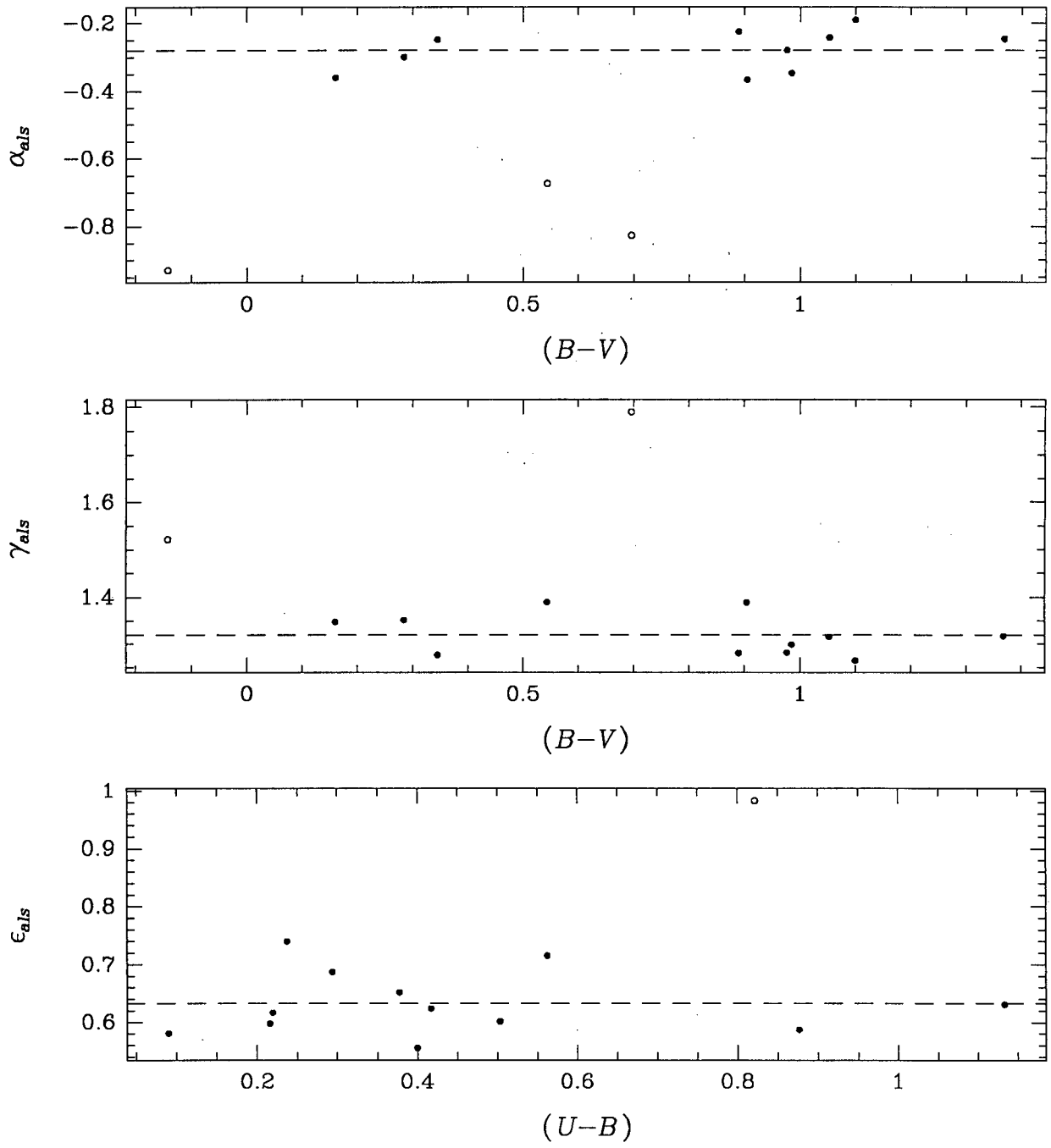

FIGURE 3.12. TEK program field ALLSTAR zero points

Open circles were deemed as outliers and dropped from consideration. The dashed line indicates the mean value of the remaining points in each of the three panels. Upper case denotes the standard system.

Chapter 4
COLOUR-MAGNITUDE AND COLOUR-COLOUR DIAGRAMS

4.1 Data Cleaning

Profile-fitting photometry can produce spurious results, e.g. a stellar image may have an unidentified neighbour in its profile which could cause the fitting to be poor. ALLSTAR returns, along with a magnitude, an estimate of the error in the magnitude. As one would generally expect, this error increases for fainter magnitudes, as the signal to noise ratio drops. If the data are cleaned by imposing an upper cut off for the error, it is found that fainter stars, with errors in an acceptable range, are rejected, while brighter stars, with relatively large errors, are accepted. To circumvent this, I employed PHOTSELECT, a program written by G. Drukier at the University of British Columbia. PHOTSELECT works by fitting a curve to the lower envelope of an error diagram, binning in magnitude, and evaluating the mean error in each bin. A 'mean multiplier' is chosen, and stars are rejected if their errors are larger than the mean multiplier multiplied by the mean error in the bin. Figures 4.1 and 4.2 show the effect of cleaning data using PHOTSELECT; note how much better delineated the blue stragglers are in the cleaner diagram.

4.2 Production of Diagrams

4.2.1 TI Data

The three program field frames which had been built for the TI data (see §2.5.2) had standard reductions performed upon them to yield ALLSTAR magnitudes for the stars. The finding thresholds used were determined by plotting a graph of detected objects against finding threshold, a steady rise in the number of detected objects is seen as the finding threshold is decreased, to a point where the shot noise in the sky starts being detected and the number of detections takes an abrupt upturn. The threshold values were chosen at the point where the sky shot-noise starts to be detected. Using a standard reduction, 544, 660 and 1229 stars were fitted on the TI *B*, *V* and *I* frames respectively.

The frames had linear displacements applied to translate them to a common origin. (*N.b.* As the telescope and its configuration were the same for all observations, one would expect linear

shifts in the X and Y coordinates only, *i.e.* scale changes or rotations are not expected, and were not allowed for.) The photometry files were cleaned to varying degrees (see §4.1) and local programs were utilized to match stars between frames and produce files with calibrated magnitudes and errors. Only stars which *were found on all three frames* were considered as real, helping to reduce spurious detections. Using mean multipliers of 2, 4 and 8 in the PHOTSELECT routine, the number of stars common to the three frames were 301, 335 and 364 respectively. One always expects fewer stars to be matched between frames; at faint magnitudes, where the incompleteness is high, only the intersection of the samples will be counted as real.

CMDs for $(B-V)$, $(B-I)$ and $(V-I)$ versus V, were plotted, along with the errors in the photometry (Figures 4.3, 4.4 and 4.5). It is apparent that the data just reaches the main sequence turn off, with the turnoff being poorly defined due to a lack of turn off stars and subgiants. With this caveat noted, the main sequence turn off is measured as lying at $V_{\rm TO}$=18.2 ± 0.2, $(B-V)_{\rm TO}$=0.65 ± 0.03, $(B-I)_{\rm TO}$=1.49 ± 0.02 and $(V-I)_{\rm TO}$=0.82 ± 0.03, as indicated by arrows in Figures 4.3, 4.4 and 4.5.

4.2.2 TEK Data

The program field U, B and V frames were reduced in a similar manner to the TI program field frames. Initially a lot of faint stars were left in the frames. To help clean up the subtracted frame, the finding thresholds were dropped and the frames reduced again. This provided a cleaner final frame and should improve the photometry by ensuring that neighbours do not contaminate the stars being fitted. The resulting ALLSTAR files were processed as above and, using mean multipliers of 1, 4 and 8, the number of stars matched between the frames were 1022, 2227 and 2553 respectively. A low value for the mean multiplier was found to give a well defined CMD. Using a low mean multiplier is valid as I expect a lot of contamination from poor fits, due to the crowding on the frame. A $(B-V)$ versus V colour-magnitude diagram is shown in Figure 4.2. It is apparent that the limit of reliable photometry is at approximately $17\overset{\rm m}{.}5$, the width of the main sequence increasing rapidly after this. Using the CMD to measure the main sequence turn off yields $V_{\rm TO}$=18.3 ± 0.3 and $(B-V)_{\rm TO}$=0.6 ± 0.03, as indicated by the arrows in Figure 4.2. The magnitude and colour of the turn off are poorly defined due to the large scatter.

4.3 Two-Colour Diagrams

The two-colour diagram considered in this work is a plot of the colour index $(U-B)$ against the colour index $(B-V)$. If the stars in the diagram were perfect black bodies, at different

temperatures, then they would define a diagonal sequence, similar to the reddening locus, in the two-colour plane. The 'S' shape in the two-colour diagram is caused mainly by absorption in the Balmer continuum, which causes the stars to be non-blackbody radiators.

4.3.1 Reddening

For spectral types O through B9, the reddening vector in the two-colour plane is given by

$$\frac{\mathrm{E}(U-B)}{\mathrm{E}(B-V)} = 0.72 + 0.005\mathrm{E}(B-V) \tag{4.1}$$

(Mihalas and Binney (1981), page 186). The colour term on the right hand side of the equation makes only a small contribution and is usually neglected for modest values of reddening. The cluster interstellar reddening can be determined by shifting the cluster fiducial along the reddening vector until the early spectral types coincide with an unreddened luminosity class V fiducial. Early spectral types are used as these stars are sufficiently hot that the metallicity does not affect their positions in the two-colour plane, unlike cooler stars. The stars which meet this requirement in the current data are the horizontal branch (HB) stars. Although not luminosity class V, the HB stars suffice for the purpose.

Figure 4.6 shows data from the TEK data and fiducials which have been reddened by $\mathrm{E}(B-V)$=$0\overset{\mathrm{m}}{.}16$, $0\overset{\mathrm{m}}{.}21$ and $0\overset{\mathrm{m}}{.}25$. There is a lot of scatter in the diagram and the HB stars do not appear to lie along a particular line. It has been suggested by Cacciari (1984) and Da Costa *et al.* (1981) that the reddening varies across the face of the cluster, but the magnitude of the effect proposed, $\Delta\mathrm{E}(B-V)$ $\sim 0\overset{\mathrm{m}}{.}03$, is too small to explain the scatter seen in the two-colour diagram.

Looking at Figure 4.2 one sees that the blue end of the HB starts to droop, and breaks off into what appear to be two branches. The HB of NGC 3201 does droop, as is clearly seen in Lee's Figure 7. With the paucity of stars on the HB, little can be said on its morphology. The bluest horizontal branch stars are critical in the determination of the reddening, and the spread in the HB causes the determination to be poor. No explanation is offered for the cause of this effect; some of the horizontal branch stars were blended, though they all subtracted from the frame cleanly. To elucidate the reddening via this method, a field is needed containing more horizontal branch stars; the small fields of CCDs are not congenial to providing this.

The reddening may also be determined by the use of field stars. Field stars that lie outside the galactic plane suffer the same absorption as the cluster. If the field stars are plotted on a two-

colour diagram, the reddening can be determined by working out the trajectories to translate the stars back onto the Population I luminosity class V fiducial, this of course assumes that the stars are Population I luminosity class V stars. There were no obvious field star candidates appearing on the CMD (Figure 4.2), and it was concluded that this method would not be of worth.

The value adopted for the interstellar reddening for the rest of this thesis was $0\overset{m}{.}21$ in accordance with the value given by Lee (1977), this value not being inconsistent with the determination of the reddening in this thesis.

4.3.2 Metallicity

Population II stars have a lower metallicity than Population I stars. The difference in metallicity means that the blue and ultraviolet atmospheric opacity in later type stars is less for Population II than for Population I. Metal-poor stars will consequently be found to lie above the metal rich stars in the two-colour diagram. The position of the cluster fiducial in the two-colour diagram will thus allow for an estimation of the metallicity. Figure 4.7 shows the main sequence and subgiant stars from the TEK frame, as defined in Figure 4.1, plotted in the two-colour plane. The data were corrected for the effects of interstellar reddening, and fiducials for metal abundances of zero and the Hyades abundance plotted. The quantity $\delta(U-B)_{0.6}$ is defined as being the height at which the data lies above the Hyades fiducial, at the intrinsic colour of $(B-V)_0$=$0\overset{m}{.}6$. The data shown in Figure 4.7 are of poor quality. An attempt was made to determine the metallicity from the available data by determining the excess at other colours, and then interpolating in the table given by Sandage (1969) to determine the excess at $(B-V)_0$=$0\overset{m}{.}6$.

A mean line through the data was drawn by eye, this was judged as being superior to simply finding the mean in a bin, due to the large number of outliers scattered to higher values of $(U-B)_0$. Values for δ were calculated and corrected as shown in Table 4.1 below.

TABLE 4.1: Corrections of δ to δ(0.6)

$(B-V)_0$	δ	M	Correction	δ(0.6)
0.35	0.12	0.54	1.19	0.14
0.40	0.12	0.54	1.19	0.14
0.45	0.14	0.61	1.18	0.17
0.50	0.10	0.42	1.09	0.11

A mean value of δ(0.6)=0.14 is obtained. To convert δ(0.6) to a value for metallicity, a calibration curve is required. I use the calibration curve as given by Richer and Fahlman (1986),

which results in the value $[Fe/H]_{IR}=-0.83$. The IR subscript indicates that the metallicity is on the scale as defined by Frogel, Cohen and Personn (1983). The derived value must be taken *cum gran salis*: this method of metallicity determination depends vitally on a good calibration and a reliable measure of reddening. A small error in $\delta(0.6)$ can lead to a large error in the metallicity determination due to the large gradient of the calibration curve. To obtain a metallicity of -1.4, a value of $\delta(0.6)=0.2$ would be required, which is not inconsistent with the data.

Other values determined for the metallicity of NGC 3201 are summarized in Table 4.2.

TABLE 4.2: Metallicity values for NGC 3201 from previous studies

[Fe/H]	Reference	Method
-1.2 ± 0.1	Lee (1977)	Two-Colour Diagram
-1.0	Pilachowski *et al.* (1980)	High Dispersion Spectra
-1.40 ± 0.06	Zinn (1980a)	Q_{39}: Integrated Light Index
-1.51 ± 0.02	Zinn (1980b)	Q_{39} (Calibration modified c.f. Zinn 1980a)
-1.4 ± 0.2	Da Costa *et al.* (1981)	Σ(W) and CMDs
-1.19 ± 0.05	Gratton (1982)	High Dispersion Spectra
-0.95 ± 0.2	Pilachowski *et al.* (1983)	High Dispersion Spectra
-1.41	Zinn and West (1984)	Q_{39}
-1.34	Grattton and Ortolani (1989)	High Dispersion Spectra
-0.83	This Work	Two-Colour Diagram

The metal abundance of globular clusters was recently a topic of debate in the literature. Results from early photographic high dispersion spectra (Pilachowski *et al.* 1983) and photometric indices (Zinn 1980a and 1980b, Zinn and West 1984) were in disagreement. The source of the discrepancy, in the case of NGC 3201, was the definition of 'metallicity', which includes numerous metals, as compared to specific quantities like [Fe/H] (Pilachowski, private communication). Recent high dispersion spectra, obtained using CCDs (*e.g.* Gratton and Ortolani (1989)), give more accurate results, which are in good agreement with results from photometry and low dispersion spectra. For subsequent work I adopt the canonical value of $[Fe/H]=-1.27 \pm 0.1$ ($Z=0.001$), in accordance with ALA89. This value is in reasonable agreement with the results from contemporary high-dispersion spectra studies and photometry indices.

4.4 Distance Modulus

To determine the distance modulus of a globular cluster, it is possible to make a comparison with field subdwarfs which have measured parallaxes. Lutz, Hanson and Van Altena (1988), using 50 field subdwarfs with accurate trigonometric parallaxes and spectroscopic [Fe/H] determinations, derive the formula

$$M_V(\pi) = 1.41 + 5.17(B - V) - 0.94[\mathrm{Fe/H}] \tag{4.2}$$

for a Population II fiducial. The distance modulus of NGC 3201 was determined by translating the subdwarf fiducial in V magnitude until it coincides with the cluster main sequence (Figure 4.8). The fiducial was fitted to the lower part of the NGC 3201 main sequence by eye, so as to avoid problems with outliers, field stars and the main-sequence turn off. A good fit was found for a distance modulus of $(m - M)_V = 14.2 \pm 0.15$, in agreement with the value derived by Lee (1977). This value is consistent with the assumption that $M_V(\mathrm{HB}) = 0^{\mathrm{m}}.6$; as shown in Figure 4.2.

4.5 Isochrone Fitting

4.5.1 Synthetic Isochrones

The isochrones used in this study are those of VB85 and are not enhanced for oxygen. By mass, oxygen constitutes half of all metals, even at solar abundance, and is an important source of opacity. Pilachowski, Sneden and Canterna (1980) report oxygen as being enhanced by a factor of two in NGC 3201 over normal solar abundances. Oxygen enhancement in globular clusters is believed to be a result of enrichment from Type II supernovae, possibly from Population III stars. At the time of writing there is some controversy over whether the use of oxygen enhanced isochrones will make any difference, as the other α-elements, *i.e.* Ne, Mg, Si, S and Ca may also have enhanced abundances. The use of oxygen enhanced isochrones leads to lower derived ages, whereas the use of isochrones, enhanced for all the α-elements, does not (Chieffi, Straniero and Salaris 1991). The isochrones used in the subsequent fittings are those of VB85 and use canonical values of Y=0.2 for the helium abundance and α=1.6 for the mixing length parameter. The isochrones are applicable to a metallicity of [Fe/H]=-1.27, see §4.3.2, and are scaled to solar abundance.

4.5.2 Deep CMDs

VB85 isochrones were superimposed on the CMDs, Figures 4.9, 4.10 and 4.12, the isochrones being corrected for a cluster having a reddening of $\mathrm{E}(B-V)$=$0\overset{\mathrm{m}}{.}21$, and a V distance modulus of 14.2, in accordance with §4.3.1 and §4.4. The value of total to selective absorption used was 3.1 in accordance with Savage and Mathis (1979). The equivalent reddenings for other colours were taken from Fahlman *et al.* (1989) and are given by

$$\begin{aligned} \mathrm{E}(V-I) &= 1.36\mathrm{E}(B-V) \\ \mathrm{E}(B-I) &= 2.36\mathrm{E}(B-V). \end{aligned} \tag{4.3}$$

To achieve coincidence of the synthetic isochrone with the zero age main sequence (ZAMS) in the $(B-V)$, V plane, (Figure 4.9), an offset in colour of $0\overset{\mathrm{m}}{.}07$ is required. There is a body of evidence (Hesser *et al.* 1987) to suggest that the VB85 isochrones are too blue by approximately $0\overset{\mathrm{m}}{.}03$ to $0\overset{\mathrm{m}}{.}04$, which may be attributable to the difficulties encountered in predicting $(B-V)$ from the temperature. The value adopted for the reddening is also open to question. Cacciari (1984) and Da Costa, Frogel and Cohen (1981) report a variable reddening across the face of NGC 3201 of the order $\Delta\mathrm{E}(B-V) \sim 0.03$. This may, in part, account for some of the large colour offset required to obtain a fit. Also, the possibility of undetected systematic calibration errors, such as caused by non-photometric conditions, can not be precluded.

Figure 4.10 shows the synthetic isochrones in the $(V-I)$, V plane. To obtain a fit to the ZAMS, the synthetic isochrones were corrected for distance modulus and reddening as above, except the equivalent reddening in $(V-I)$ was derived from equation 4.3 above. In this case, a colour offset of $-0\overset{\mathrm{m}}{.}01$ in $(V-I)$ was applied to the isochrones.

Figure 4.12 shows the synthetic isochrones on the $(B-I)$, V plane. The isochrones were corrected for the distance modulus and had an equivalent reddening in $(B-I)$ applied to them and a colour offset in $(B-I)$ of $0\overset{\mathrm{m}}{.}05$ was applied to make the isochrones coincide with the ZAMS.

4.5.3 Age Determination from Deep CMDs

Cluster dating via isochrone fitting is an art with many caveats. To be able to date a cluster one needs to know accurately the distance modulus, the cluster reddening, the cluster metallicity as well as having data with a good calibration. The input to the synthetic models is still very uncertain; no one is sure what abundance ratios to use, or whether the mixing length parameter is correct for stars unlike the sun, and there appears to be problems in translating the isochrones

from the theoretical to observational planes as mentioned above. Given all of this, a quixotic attitude is also required.

With the above pitfalls noted, I state that NGC 3201 appears to be around 15 ± 2 Gyr old, though I place little confidence in this value given the above and noting the lack of subgiant and main sequence turn off stars to allow for discrimination between the isochrones. The subgiant branch of the synthetic isochrones do not appear to fit the data at all, though the brighter stars probably are not all subgiants; if they were they would form a tight sequence instead of having the large spread in colour and magnitude which is seen. The stars seen are probably field stars. I back up this claim by presenting the CMD for a background field in Figure 4.11. The background field is the one as discussed in chapter 6. The studies of ALA89 indicate an age of 16 ± 3 Gyrs for NGC 3201. Figure 4.13 shows points defining the V, $(B-V)$ main sequence of NGC 3201 from the studies of ALA89. It is immediately obvious that the morphologies of the isochrones and data are not similar, and the diagram clearly demonstrates the subjective nature of isochrone fitting. For example, at $V < 17\overset{\text{m}}{.}5$ the fiducial of ALA89 appears to fit the 16 Gyr isochrone well, while for $17\overset{\text{m}}{.}5 < V < 18\overset{\text{m}}{.}5$ the fiducial fits the 14 Gyr isochrone. For $V > 19\overset{\text{m}}{.}0$ the fiducial does not fit the isochrones.

In conclusion, I state that my age estimate based on synthetic isochrone fitting is 15 ± 2 Gyr. This is in agreement with the value reached by ALA89, though I feel that the ALA89 data may be questionable given the morphology of the derived CMD. I can state that the morphology of the CMDs from the present study agrees with the synthetic isochrones.

4.5.4 Shallow CMDs

VB85 isochrones were superimposed on the $(B-V)$, V CMD resulting from the TEK data, (Figure 4.14). The isochrones were corrected for a cluster having a reddening of $E(B-V)=0\overset{\text{m}}{.}21$ and a V distance modulus of 14.2, in accordance with §4.3.1 and §4.4. To obtain coincidence of the giant branch of the synthetic isochrone with the data, it was found necessary to apply a colour offset to the isochrones of $0\overset{\text{m}}{.}04$. The possible reasons for this are discussed in §4.5.2. It is hard to draw any solid conclusions from the data, due to the ill-defined main sequence. It appears that the age is around 16 ± 2 Gyr; this being consistent with the value derived in §4.5.3.

4.5.5 Combined CMDs

For completeness, a montage of the data in Figures 4.2 and 4.3 was plotted, (Figure 4.15). No allowance was made for possible zero point errors in the calibration or possible differential

reddening effects; there is a possibility that the fiducial sequences are misaligned. No stars were common to the two frames (Figure 2.1), and so it was not possible to find a common zero point.

VandenBerg, Bolte and Stetson (1990) discuss and implement a technique for determining relative ages of clusters with similar metallicities. The technique does not require the cluster reddening or distance modulus to be known, it only requires that a well defined fiducial exists for the cluster. The technique works by utilizing the fact that the difference in colour between the main sequence turn off and the giant branch is an age sensitive parameter. One chooses a fiducial cluster, and then aligns the cluster fiducial in colour by matching the main sequence turn offs, and in magnitude by matching a point slightly redder than the turn off. Differences in the position of the giant branch can then be interpreted in terms of age differences.

Figure 4.3 shows the cleaned CMD derived from the TI data. As can be seen, the main sequence turn off is barely defined, and there is no giant branch. Figure 4.2 shows the cleaned CMD derived from the TEK data. Although the giant branch is reasonably well defined, the main sequence turn off is very noisy and it would be foolhardy to extract a fiducial sequence from it. An attempt was made to implement the technique, but was abandoned as being futile due to problems in defining the main sequence turn off. VandenBerg *et al.* (1990) state that an uncertainty in $(B-V)$ of $\pm\ 0\overset{\mathrm{m}}{.}02$ leads to an uncertainty in age of $\pm$ 2 Gyrs, and so, clearly, a better defined sequence is required to implement this technique with any degree of credulity.

For the rest of this thesis, an age of 16 Gyr is adopted for NGC 3201.

4.6 Binaries

Evidence, from photometry techniques, for binary stars in globular clusters has been found, e.g. McClure *et al.* (1985) found photometric evidence for binaries in E 3, as did Bolte (1988) and Sato, Richer and Fahlman (1989) for NGC 288 and M12 respectively. On the other hand, some studies show absolutely no evidence for the existence of binaries in other clusters. Binary stars are important in the dynamical consideration of globular clusters as they can provide a heating mechanism to reexpand the cluster core after gravothermal collapse.

From Figures 4.2 and 4.3 there is no obvious evidence for an equal-mass binary sequence. Binary stars would manifest themselves as a sequence displaced upwards by approximately $0\overset{\mathrm{m}}{.}75$ magnitudes (for stars of equal mass). Whether one would expect to find binaries in the outer field is doubtful; mass segregation would tend to cause the heavier binaries to migrate to the cluster core. It has been shown by Spitzer and Mathieu (1980) that if initially 10 per cent of the stars in a globular cluster are binaries, then the density of binaries in the cluster core would

rapidly rise to 50 → 100 per cent. Hence, to investigate whether NGC 3201 has a large number of binaries, a study of the cluster centre, extending down the main sequence, would be beneficial.

Photometric techniques for detecting binaries will underestimate the binary abundance as systems with large mass ratios, or with sub-luminous companions will be undiscovered. Griffin *et al.* (1988) found numerous binary systems, recognized by radial velocity variations, lying along the main sequence in the Hyades. Griffin *et al.* (1988) find that approximately one third of the binaries are well separated from the main sequence, indicating that the detection efficiencies for binaries via photometry will be similar. It can be demonstrated (Richer 1991, preprint) that if the cluster were to be entirely composed of binaries, with a spectrum of mass ratios, then it may be hard to spot the binary candidates from the errors in the photometry. Given this, it may be hasty to reject the presence of binaries in NGC 3201 based solely on the current data. A more thorough study looking carefully at the main-sequence width and errors is needed.

4.7 Blue Stragglers

Figure 4.1 clearly shows a sequence of blue stragglers. The blue stragglers are seen as an extension of the zero age main sequence beyond the main sequence turn off. Many explanations have been proposed for the formation of blue stragglers, and I point the interested reader to Leonard (1989), and references therein, for a contemporary discussion of proposed formation mechanisms. Figure 4.16 shows the location of the blue stragglers on the field.

If blue stragglers are coalesced binaries then they would be expected to be more massive than other cluster members and therefore maybe more centrally concentrated, due to mass segregation effects, provided that their ages are longer than the cluster relaxation time. To test this hypothesis, a comparison of the central concentration of blue stragglers and subgiants is made on the TEK frame. The subgiants are chosen to have the same magnitude range as the blue stragglers so that the two sets of stars are similarly incomplete, and any bias due to magnitude dependent crowding (Nemec and Harris 1987) is avoided. Using the selection criterion for blue stragglers that ($0\overset{m}{.}2 < (B-V) < 0\overset{m}{.}6$) and ($16 < V < 18$), there were 18 candidates, while 141 subgiants were selected with the criteria that ($0\overset{m}{.}6 < (B-V) < 1\overset{m}{.}0$) and ($16 < V < 18$). A graph of cumulative fraction against the logarithm of the radial distance is shown in Figure 4.17. It appears, from Figure 4.17, that the blue stragglers are more centrally concentrated than the subgiants. To quantify this hypothesis the Kolomogorov-Smirnov (K-S) test is used. The K-S statistic will test the null hypothesis that the distributions are the same, against the alternative that they are different. The K-S statistic is given by

$$D = \max_{-\infty < x < \infty} |S_{N_1}(x) - S_{N_2}(x)|, \tag{4.4}$$

for two cumulative distributions, where $S_{N_1}(x)$ and $S_{N_2}(x)$ are the two cumulative distribution functions (Press *et al.* 1987). The function

$$Q_{ks}(\lambda) = 2 \sum_{j=1}^{\infty} (-)^{j-1} e^{-2j^2\lambda^2} \tag{4.5}$$

allows for the calculation of the significance of the result. The significance level of an observed value of D (as a disproof that the distributions are the same) is

$$Q_{ks}\left(\sqrt{\frac{N_1 N_2}{N_1 + N_2}}\ D \right), \tag{4.6}$$

where N is the number of points in the distributions (Press *et al.* 1987).

For the distributions under consideration, D was calculated to be 0.407. The significance level of this result was calculated to be $\sim$0.01, *i.e.* there is a one per cent chance that the two samples were drawn from the same distribution. From this I conclude that *the blue stragglers in the TEK field are more centrally concentrated, at a confidence level exceeding 99 per cent, than the subgiants.*

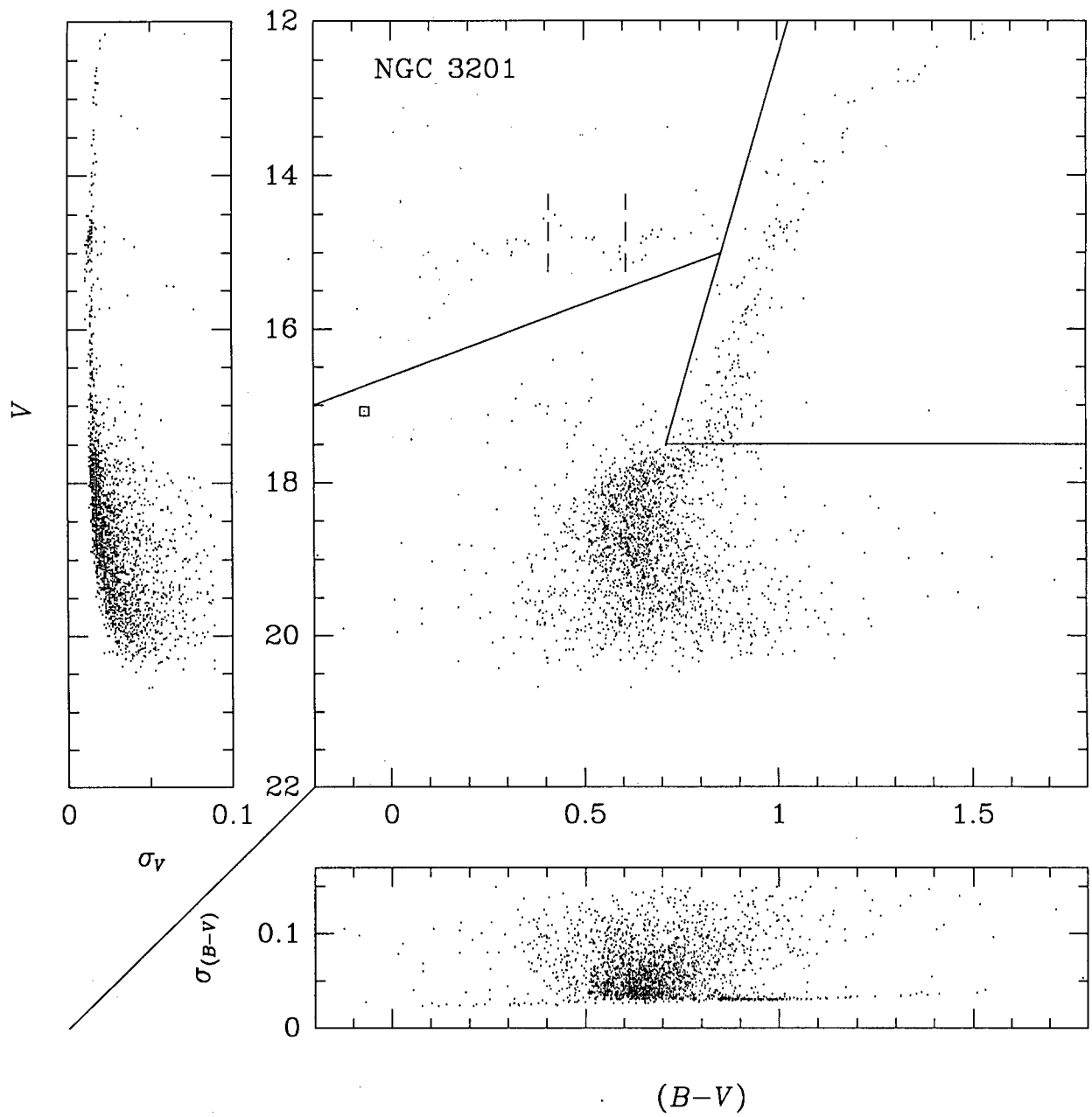

FIGURE 4.1. Shallow CMD, with slight cleaning, showing divisions made to distinguish classes of star

The upper left region defines the horizontal branch stars, the upper right region the giants and the lower division is for the main sequence and subgiant branch stars. Dashed lines indicate the RR-Lyrae gap as defined by Lee (1977). The data were cleaned using PHOTSELECT (§4.1) with a mean multiplier of 8. The square indicates Lee's unusual star (see chapter 5).

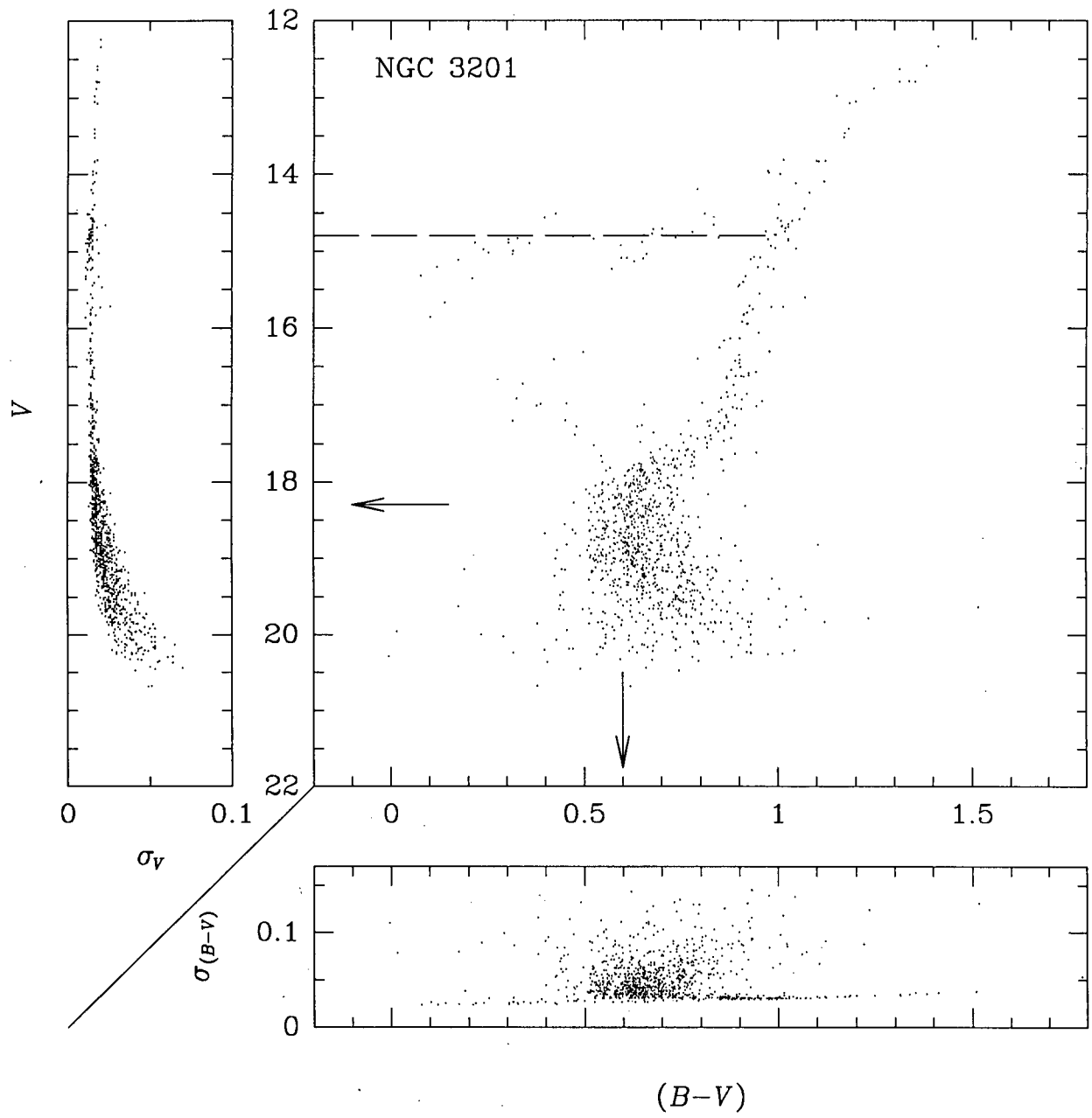

FIGURE 4.2. Shallow CMD with cleaning

The data were cleaned using a mean multiplier of 1 in the PHOTSELECT routine (see §4.1). Arrows indicate the values chosen for the main sequence turn off. The dashed line indicates a magnitude of 14 $^{\rm m}\!.$8, the expected magnitude of the horizontal branch, assuming M_V(HB)=0 $^{\rm m}\!.$6 and $(m-M)_V$=14 $^{\rm m}\!.$2.

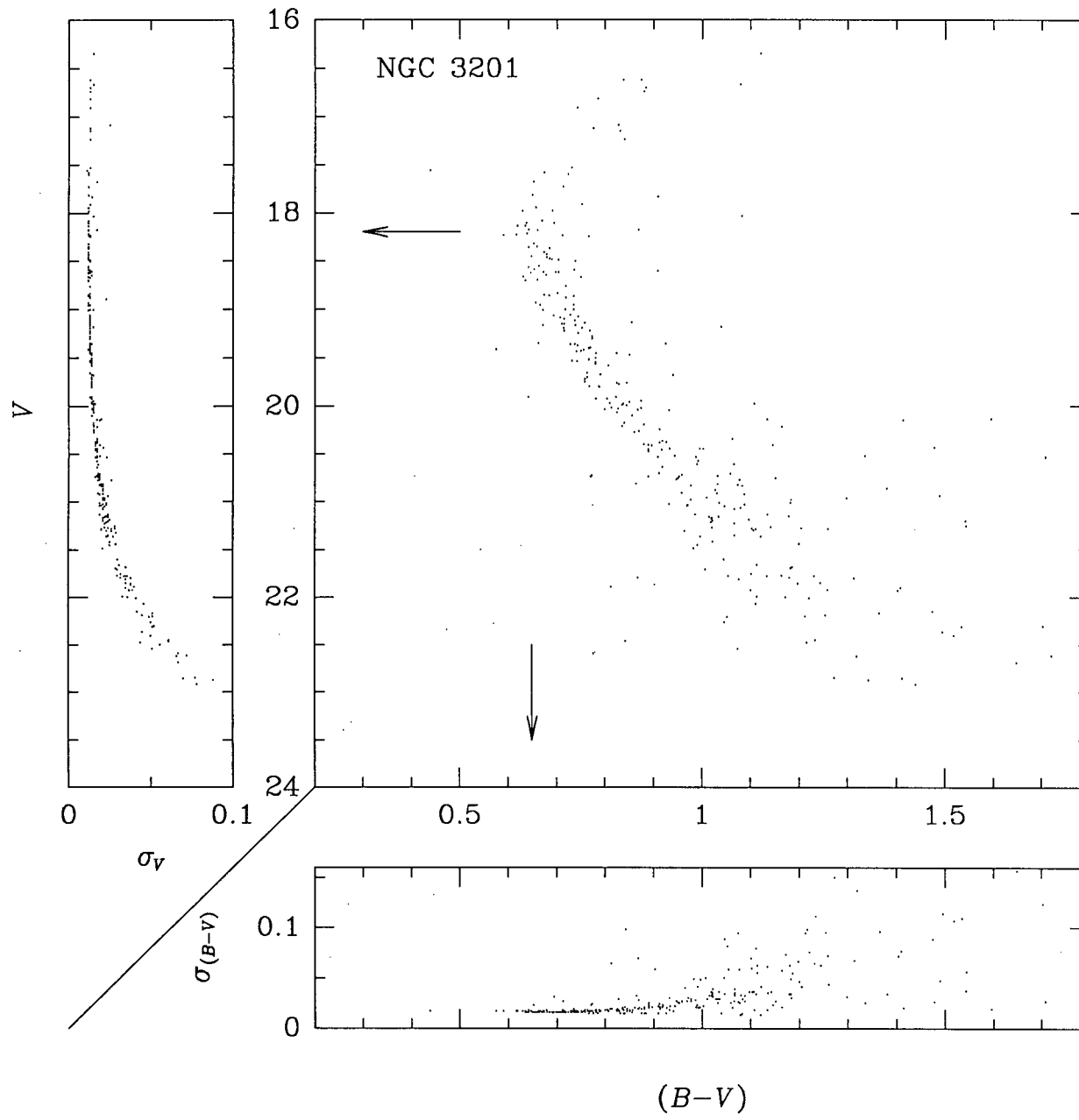

FIGURE 4.3. Deep $(B-V)$ CMD

The data were cleaned using a mean multiplier of 2 in the PHOTSELECT routine (see §4.1). Arrows indicate the values chosen for the main sequence turn off.

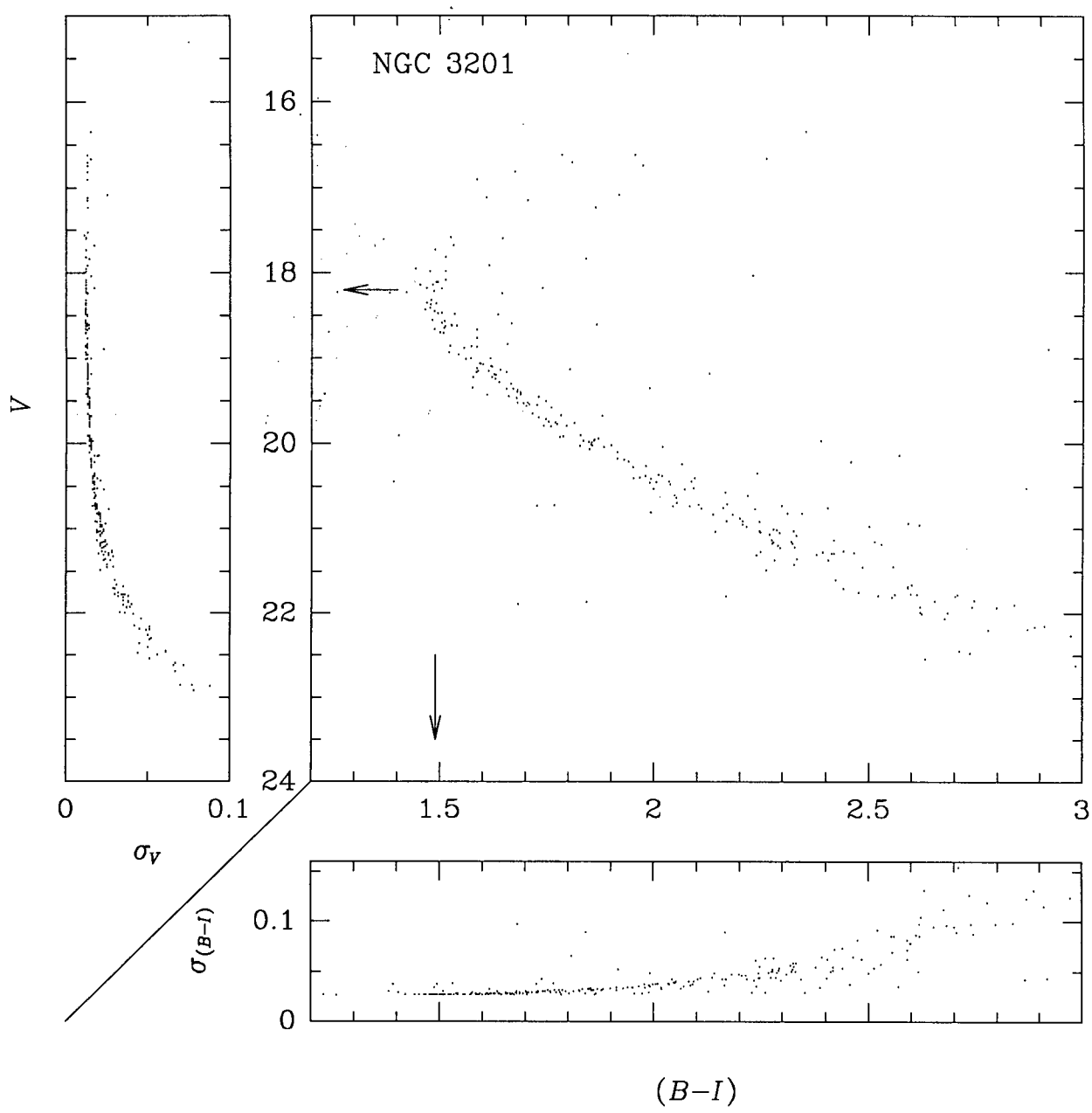

FIGURE 4.4. Deep $(B-I)$ CMD

The data were cleaned using a mean multiplier of 2 in the PHOTSELECT routine (see §4.1). Arrows indicate the values chosen for the main sequence turn off.

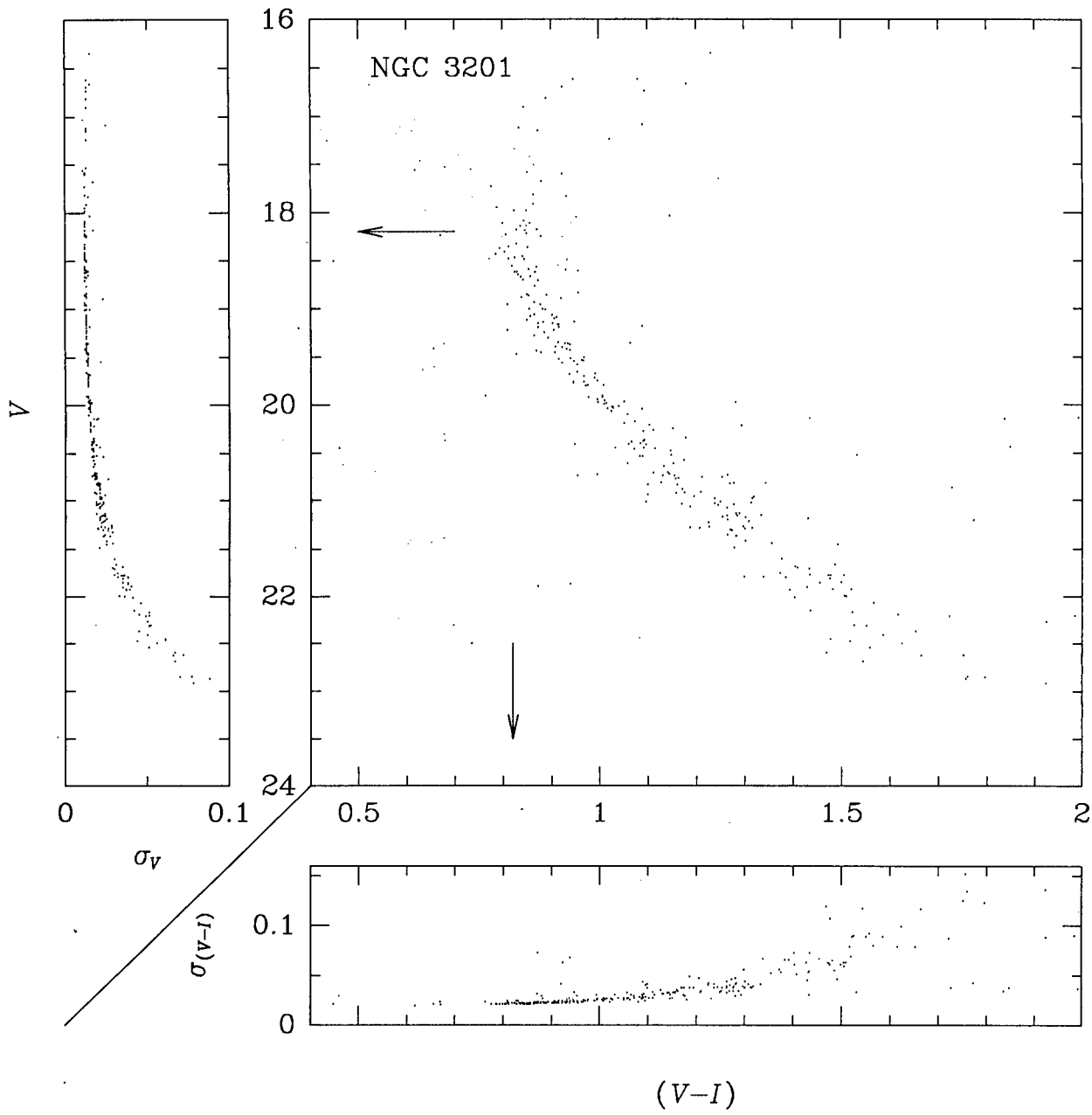

FIGURE 4.5. Deep $(V - I)$ *CMD*

The data were cleaned using a mean multiplier of 2 in the PHOTSELECT routine (see §4.1). Arrows indicate the values chosen for the main sequence turn off.

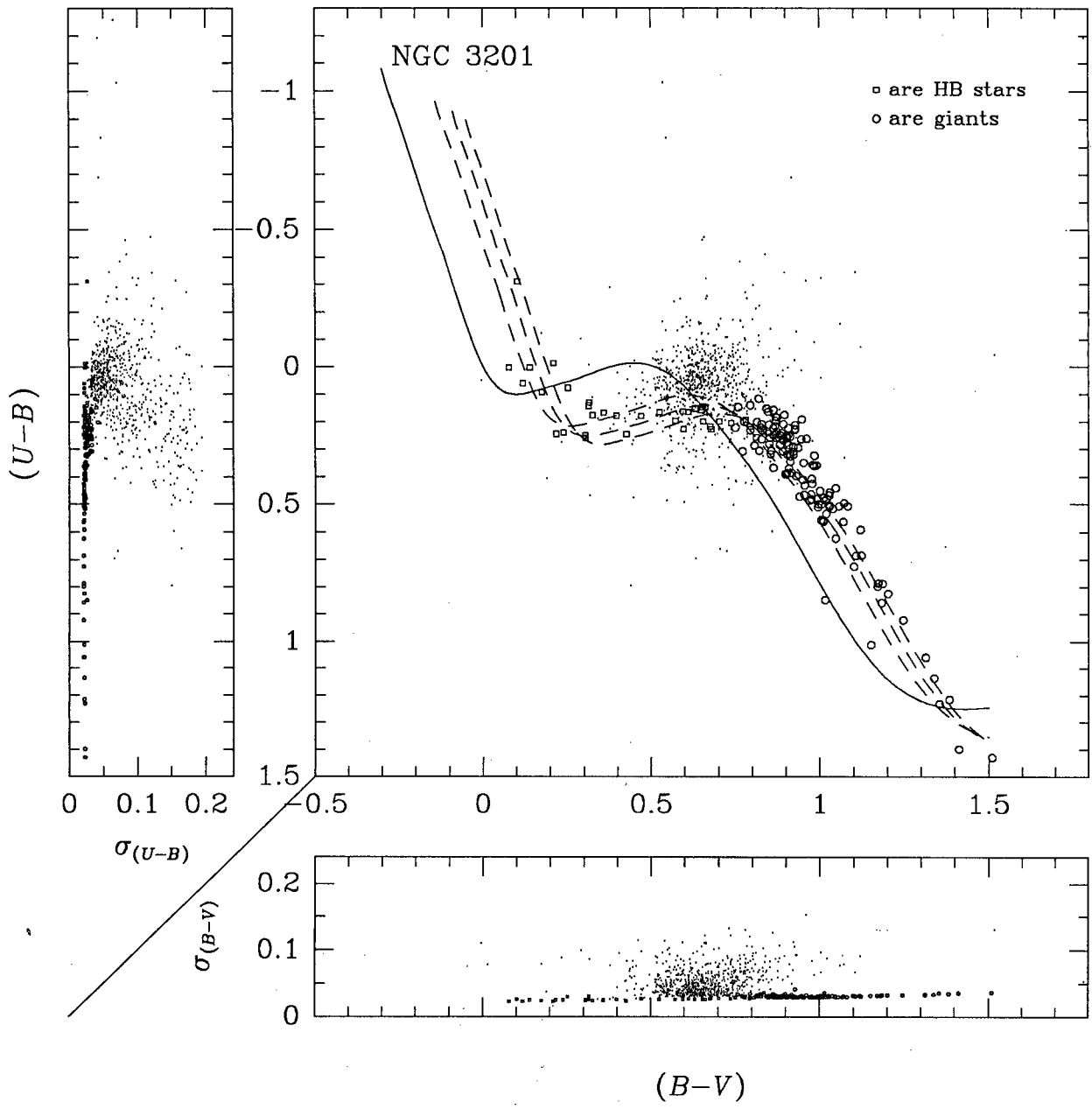

FIGURE 4.6. Two-colour diagram for the TEK program field, with luminosity class V fiducials

Horizontal branch stars, giants and main sequence/subgiant branch stars, as defined in Figure 4.1, are indicated. The solid curve is the unreddened Population I luminosity class V two-colour fiducial (Mihalas and Binney 1981), whilst dashed curves represent the same fiducial reddened by the amounts $0\overset{m}{.}16$, $0\overset{m}{.}21$ and $0\overset{m}{.}25$. The data were cleaned using a mean multiplier of 1 in the PHOTSELECT routine (see §4.1).

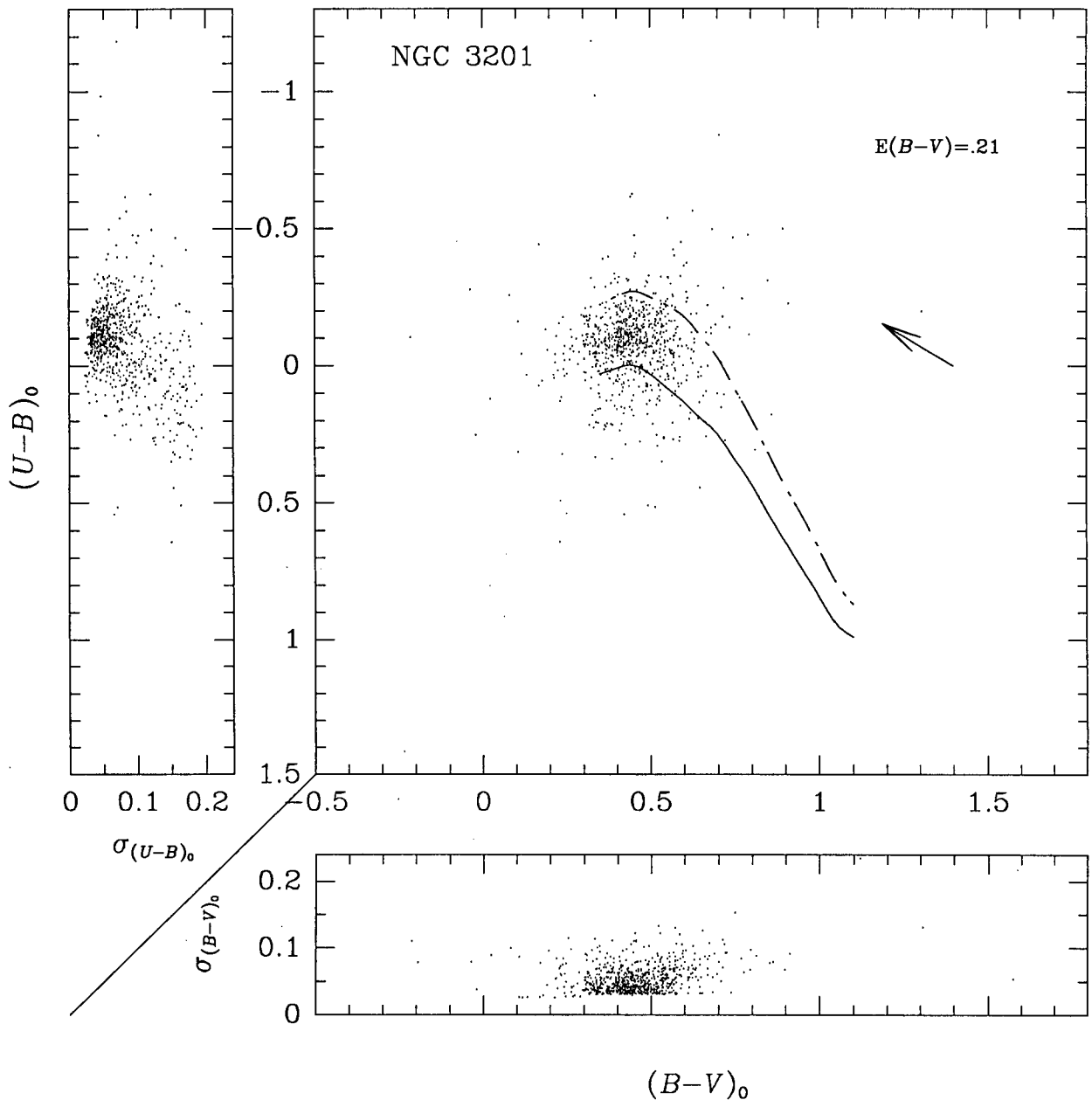

FIGURE 4.7. Two-colour diagram for the TEK program field, with minimum and maximum abundance fiducials

The diagram contains main sequence and subgiant stars only, as defined in Figure 4.1. The solid line is the Hyades fiducial sequence, while the dashed line represents the minimum abundance fiducial (Sandage 1969). The colours of the stars have been corrected for reddening by amounts $\mathrm{E}(B-V)$=0$^{\mathrm{m}}$.21 and $\mathrm{E}(U-B)$=0$^{\mathrm{m}}$.153. The data were cleaned using a mean multiplier of 1 in the PHOTSELECT routine (see §4.1).

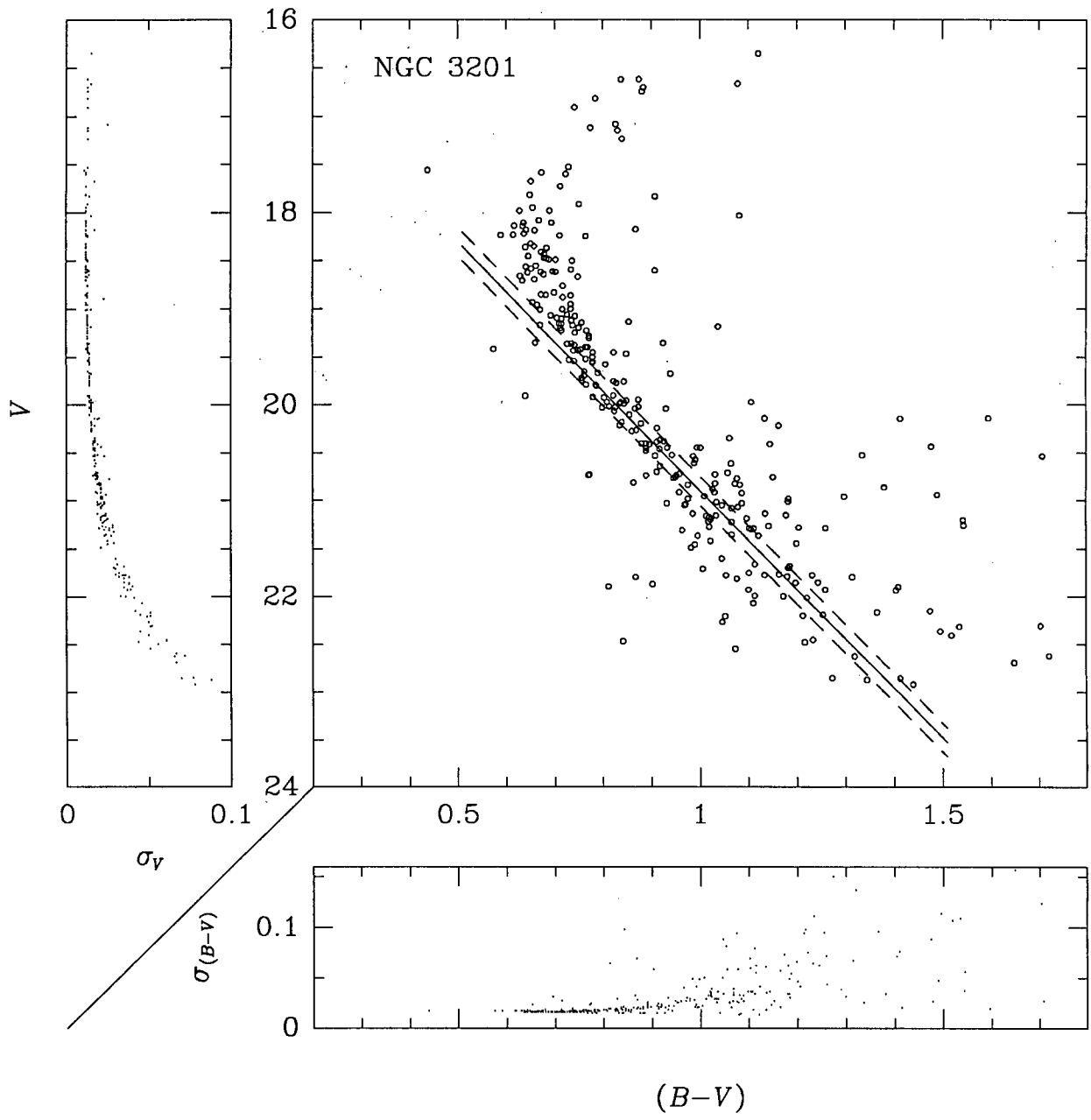

FIGURE 4.8. Deep $(B-V)$ CMD of NGC 3201 with a subdwarf fiducial imposed

The subdwarf fiducial is from Lutz, Hanson and Van Altena (1988). The fiducial, corrected for a *V* distance modulus of 14.2, is shown as a solid line, while fiducials with distance moduli of $14.2 \pm 0\overset{\mathrm{m}}{.}15$ are shown as dashed lines. The subdwarf fiducial was appropriate for a metallicity of [Fe/H]=−1.27 and had been reddened by $\mathrm{E}(B-V)=0\overset{\mathrm{m}}{.}21$.

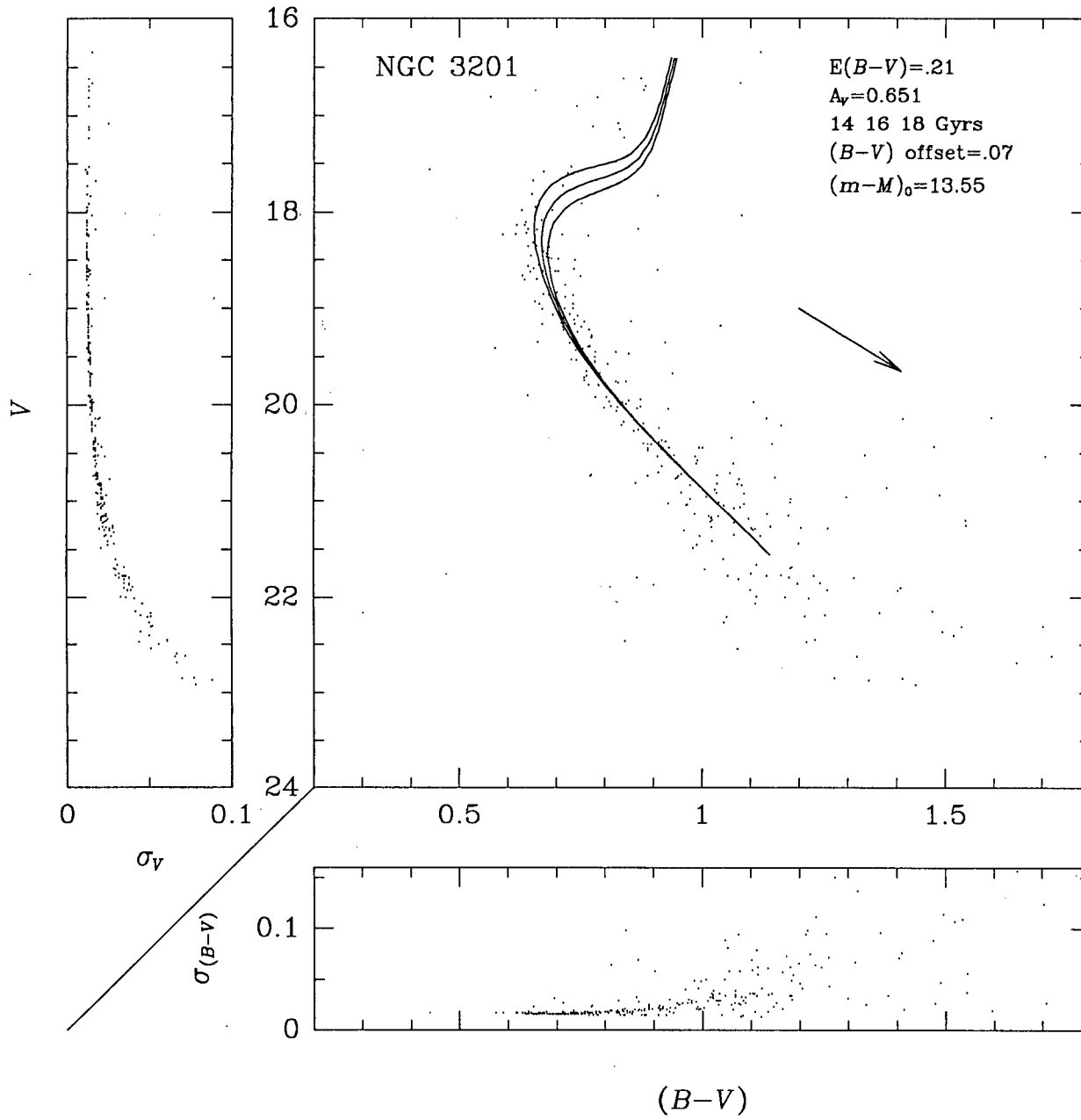

FIGURE 4.9. Deep $(B-V)$ CMD with VB85 isochrones imposed

The isochrones are for stellar models with α=1.6, [Fe/H]=−1.27, and Y=0.20 and have been reddened by $\mathrm{E}(B-V)$=0 $^{\mathrm{m}}$.21 and corrected for the distance modulus of NGC 3201. The data were cleaned using a mean multiplier of 2 in the PHOTSELECT routine (see §4.1).

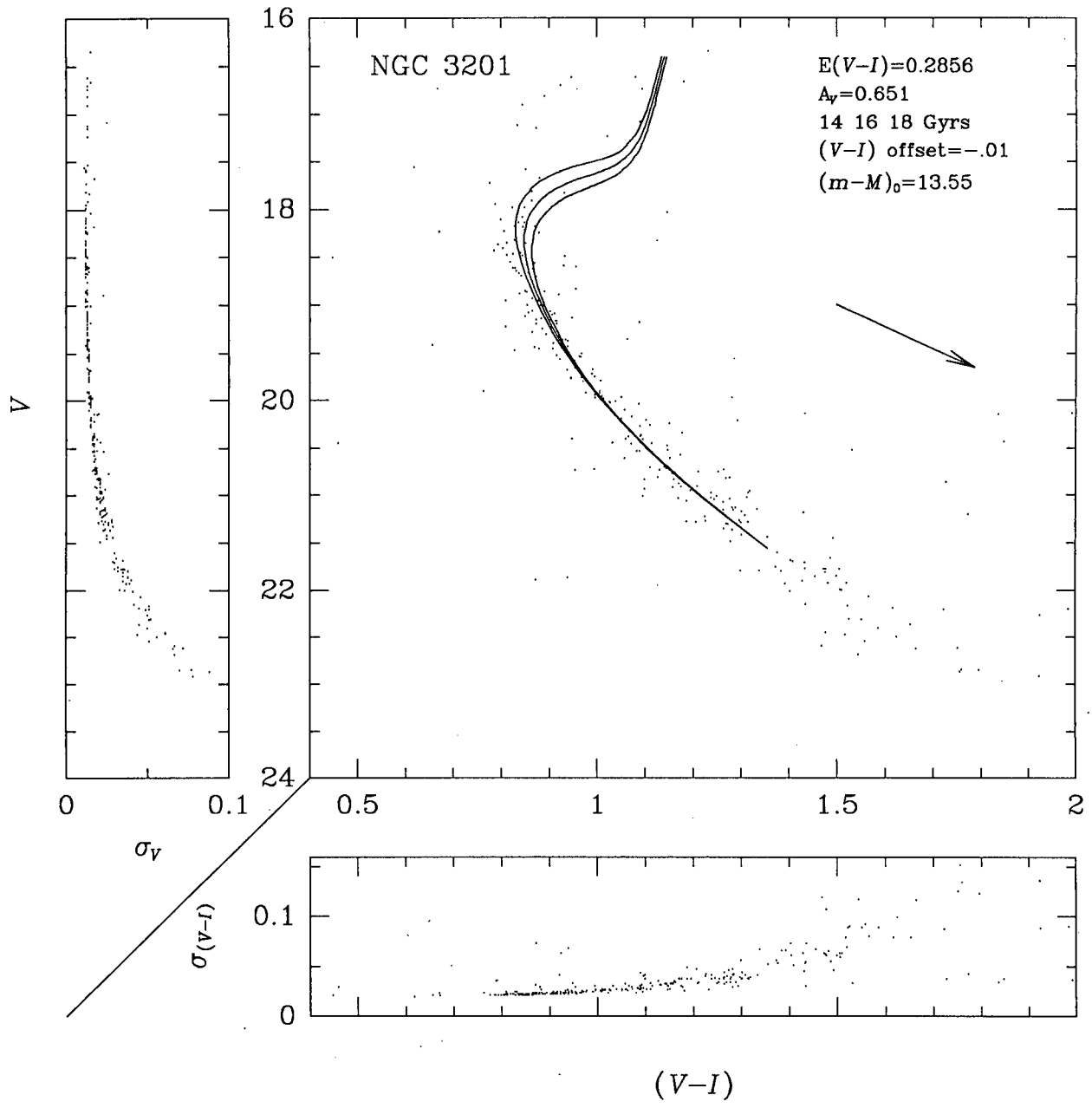

FIGURE 4.10. Deep $(V-I)$ CMD withVB85 isochrones imposed

The isochrones are for stellar models with α=1.6, [Fe/H]=−1.27, and Y=0.20 and have been reddened by $\mathrm{E}(V-I)$=0 $^{\mathrm{m}}$.286 and corrected for the distance modulus of NGC 3201. The data were cleaned using a mean multiplier of 2 in the PHOTSELECT routine (see §4.1).

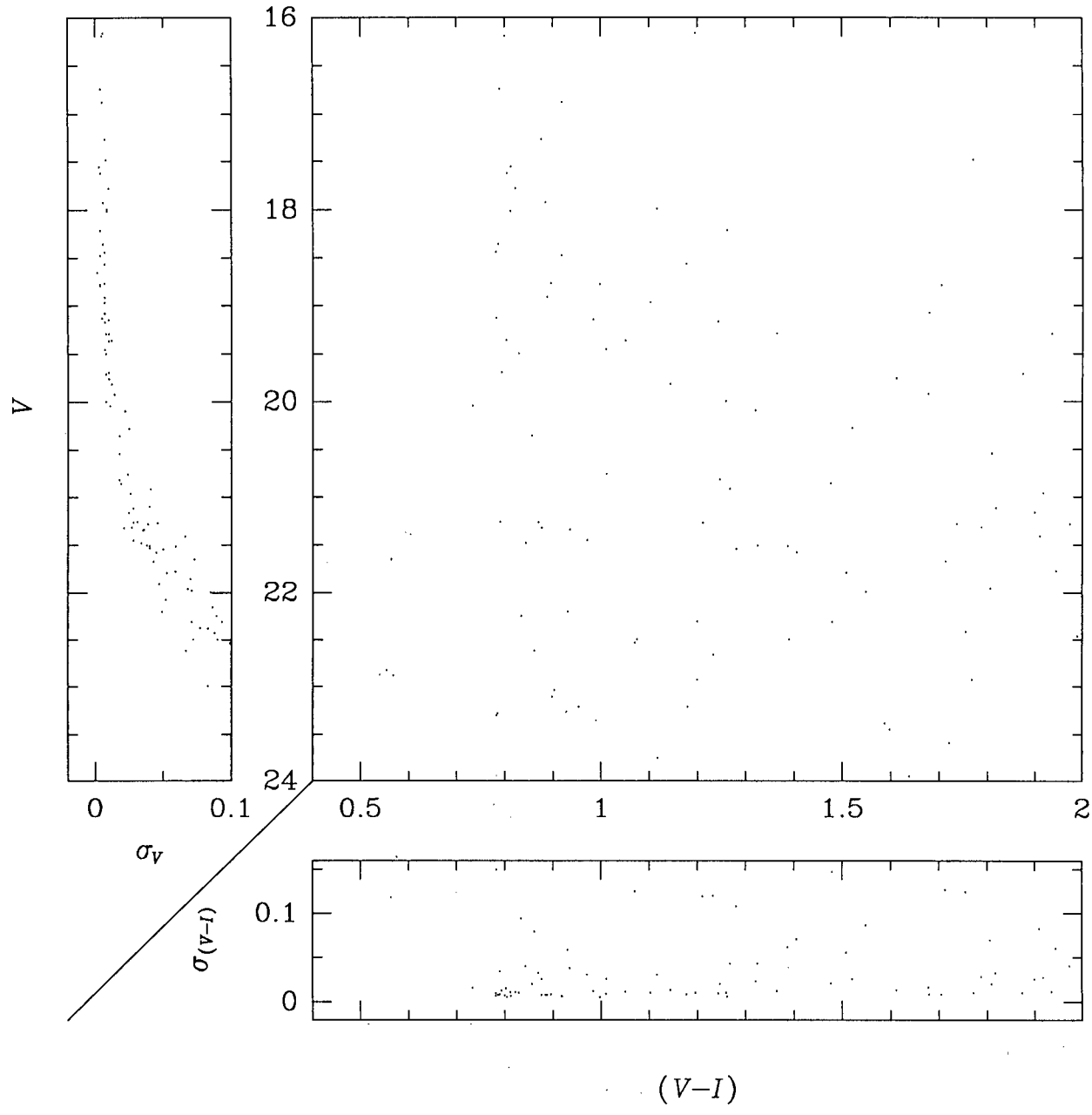

FIGURE 4.11. Deep $(V - I)$ CMD for a background field near NGC 3201

Background fields in *V* and *I* were reduced, and stars found were calibrated and matched. The errors shown are those returned by ALLSTAR, being added in quadrature for $(V - I)$.

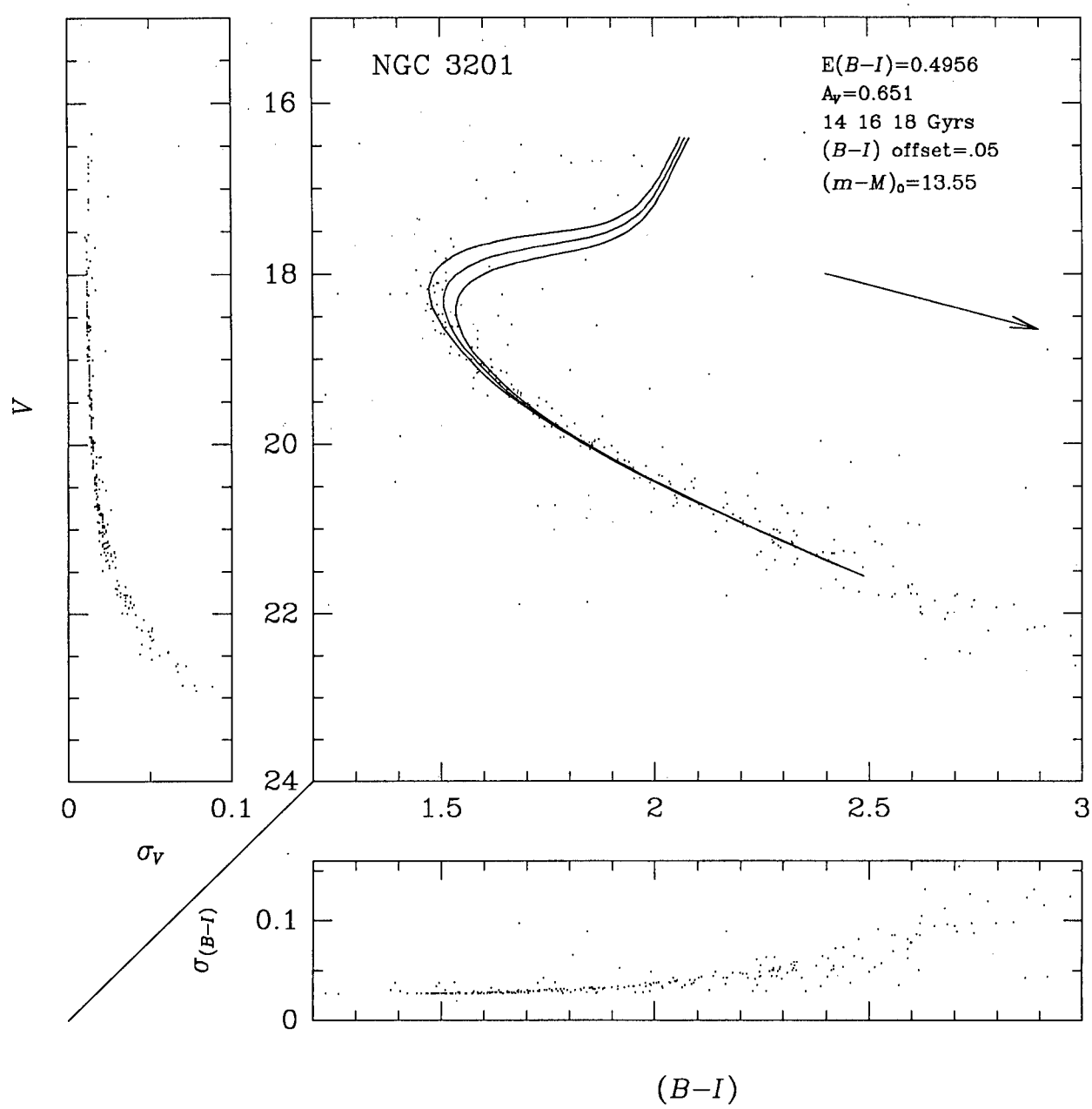

FIGURE 4.12. Deep $(B-I)$ CMD with VB85 isochrones imposed

The isochrones are for stellar models with α=1.6, [Fe/H]=−1.27, and Y=0.20 and have been reddened by $\mathrm{E}(B-I)$=0 $^{\mathrm{m}}$.496 and corrected for the distance modulus of NGC 3201. The data were cleaned using a mean multiplier of 2 in the PHOTSELECT routine (see §4.1).

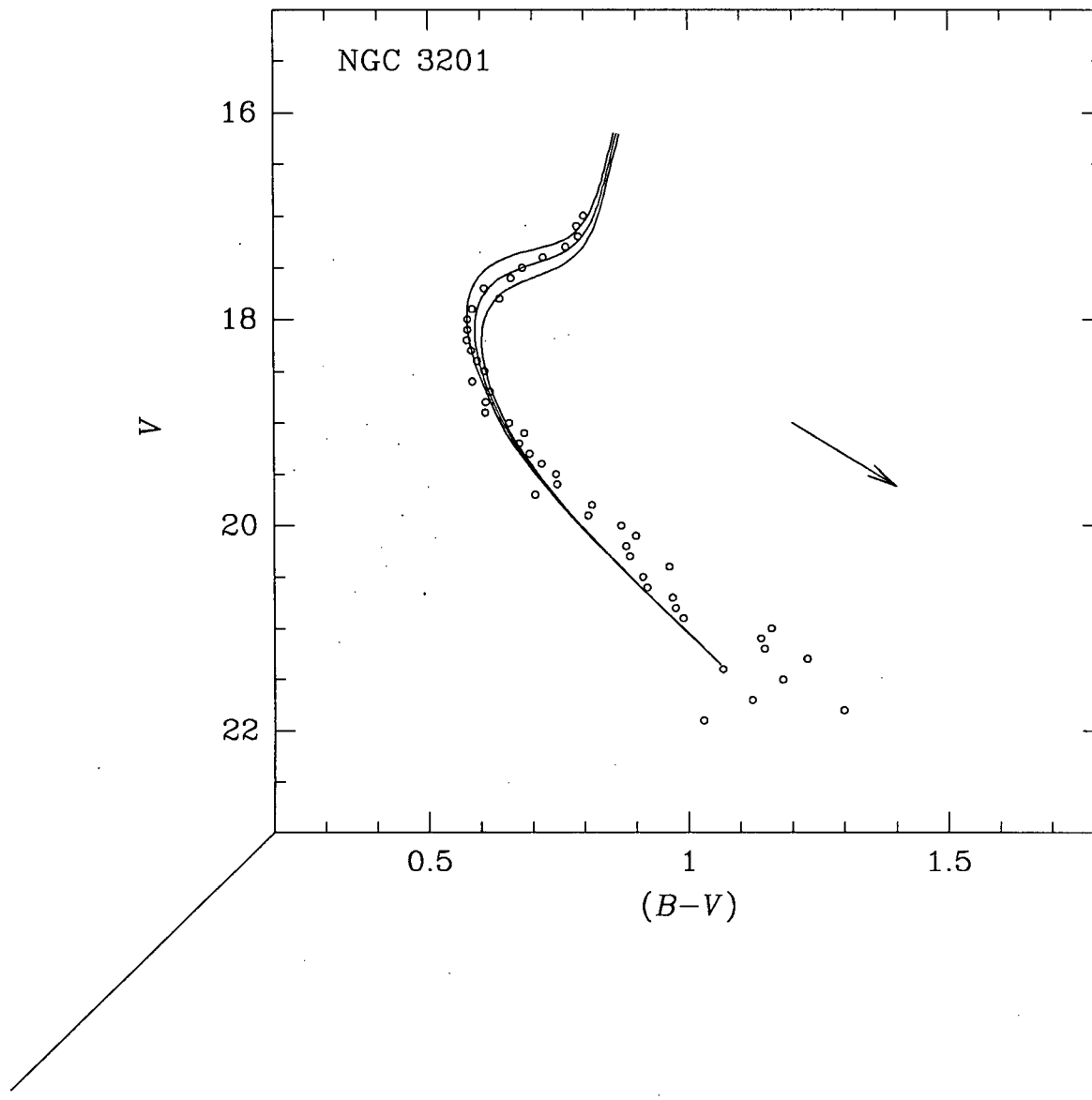

FIGURE 4.13. The $(B-V)$ CMD of ALA89

The open points are the mean values of colour taken at every $0^{\rm m}.20$. The solid lines are VB85 isochrones which have had the reddening and distance modulus adopted by ALA89 applied to them.

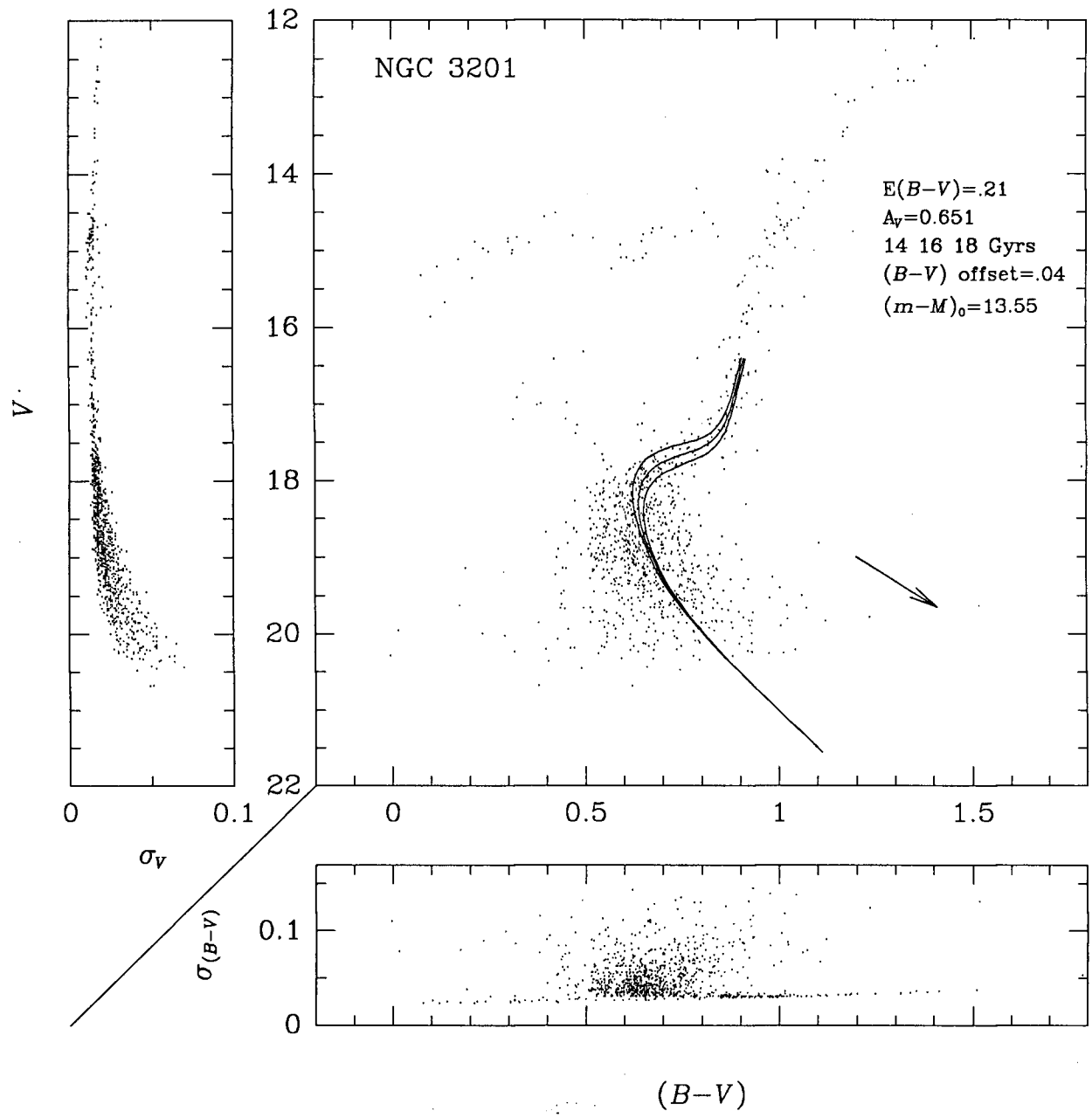

FIGURE 4.14. Shallow $(B-V)$ CMD with VB85 isochrones imposed

The isochrones are for stellar models with α=1.6, [Fe/H]=−1.27, and Y=0.20 and have been reddened by $\mathrm{E}(B-V)$=0$^{\mathrm{m}}$.21 and corrected for the distance modulus of NGC 3201. The data were cleaned using a mean multiplier of 1 in the PHOTSELECT routine (see §4.1).

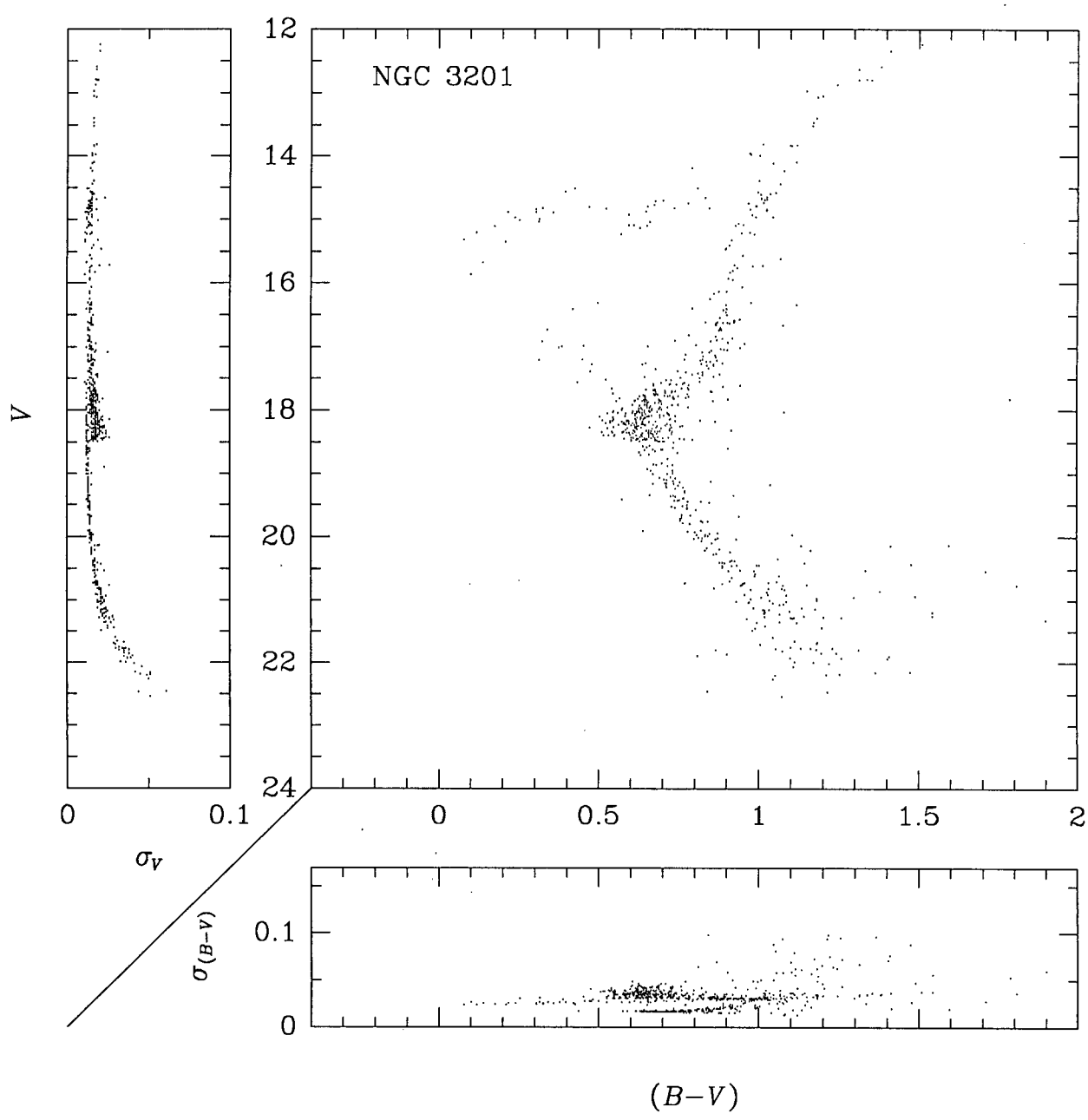

FIGURE 4.15. Combined $(B-V)$ CMD for TI and TEK data sets

The diagram is a montage of the data from Figures 4.2 and 4.3. The TEK data were only included for *V* magnitudes brighter than $18\overset{m}{.}5$.

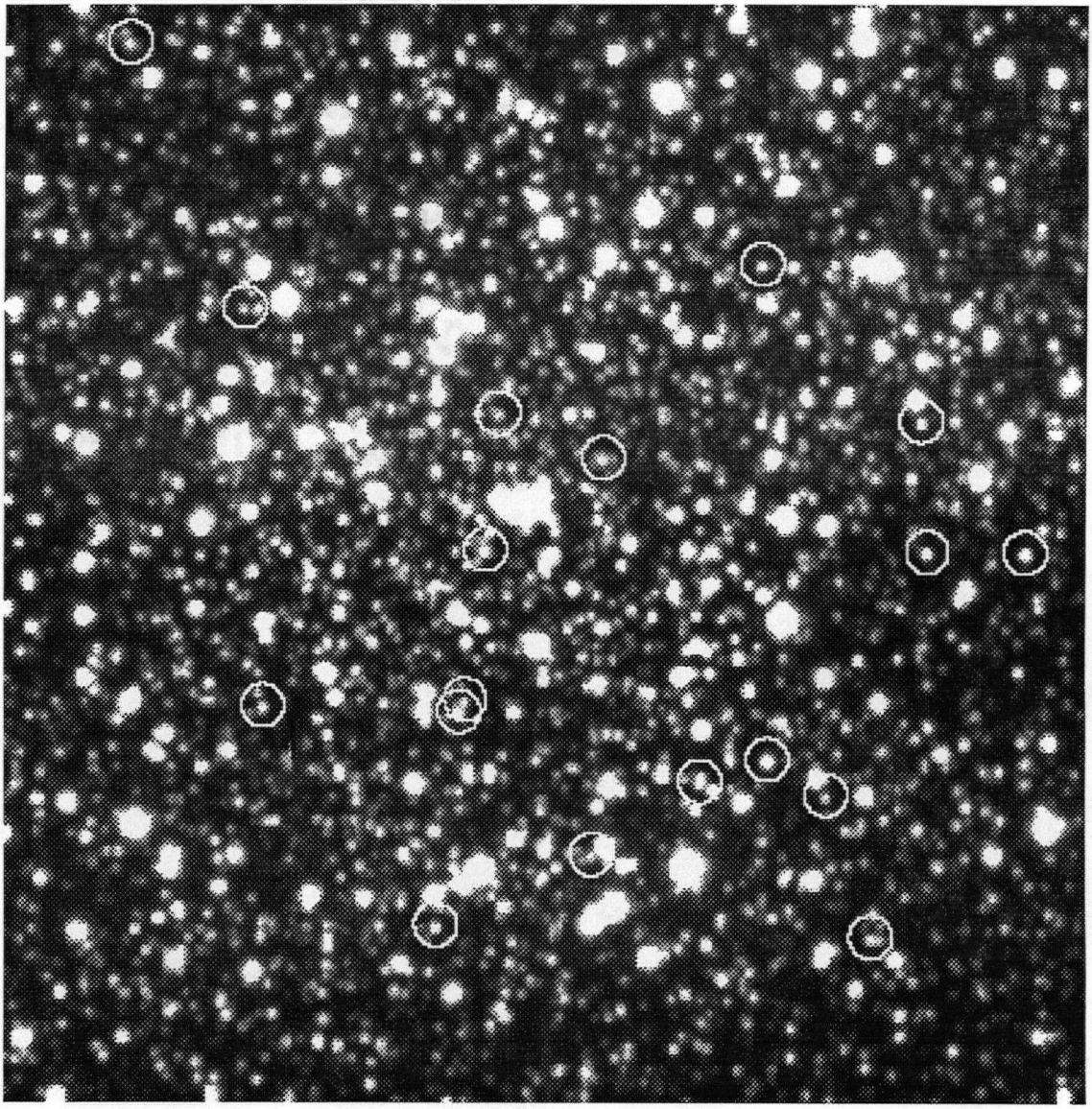

FIGURE 4.16. Location of blue stragglers on the TEK program field

The circles in the diagram are centred on blue stragglers. The image is a *V* image of the TEK program field.

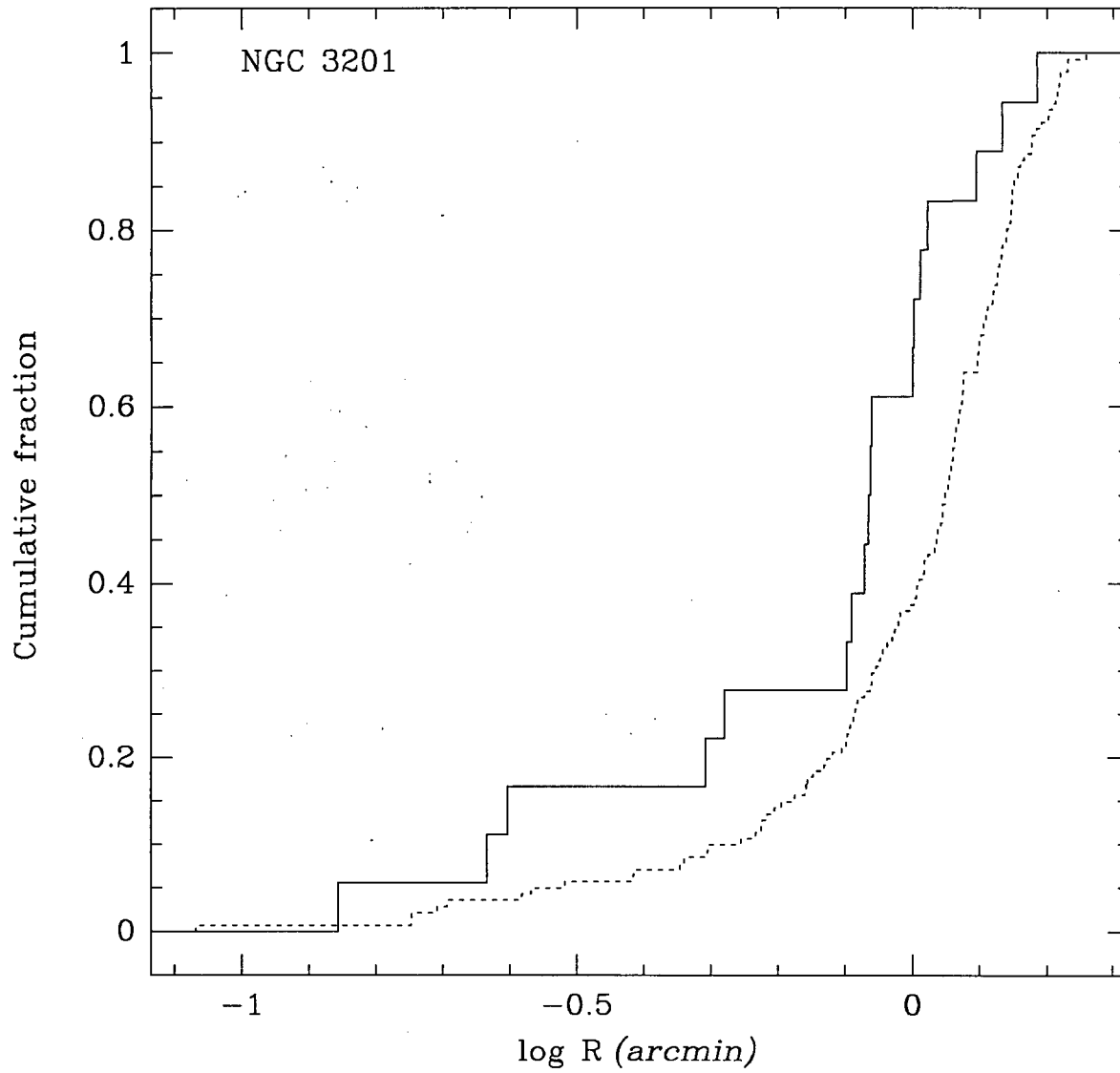

FIGURE 4.17. Cumulative distributions of blue stragglers and subgiants in the TEK program field

The ordinate is the cumulative fraction, while the abscissa is the logarithm of the radial distance in *arcmins*, the cluster centre being defined according to Lee (1977), *i.e.* the centre of the concentric circles on Figure 5.2. The solid line represents the blue stragglers and the dashed line is for the selected subgiants.

Chapter 5
LEE'S UNUSUAL STAR

5.1 Observations

Lee (1977) reports an unusual star, with a large UV excess, located towards the centre of NGC 3201. He measures the star as having V=15$^{\rm m}\!.$89, $(B-V)$=0$^{\rm m}\!.$78 and $(U-B)$=$-$0$^{\rm m}\!.$90. Lee's Unusual Star (LUS) was located on the TEK field, and is shown in U, B and V band images in Figure 5.1. Close examination of the U band image showed LUS to be blended with a neighbour, which can be visually resolved on the B and V frames. Analysis of the U image showed that LUS corresponded to the lower of the two stars; the centre of the combined images corresponding to the centre of the lower star. My photometry on LUS yields the values V=17$^{\rm m}\!.$08, $(B-V)$=$-$0$^{\rm m}\!.$07 and $(U-B)$=$-$0$^{\rm m}\!.$94. Figure 4.1 shows the location of LUS in the colour-magnitude plane, it is not seen in Figure 4.2 due to rejection by the PHOTSELECT routine. The errors returned by ALLSTAR were around 0$^{\rm m}\!.$01 for each of the three magnitudes, and LUS was likely rejected due to its larger errors compared with other objects in the same magnitude range.

My photometry is in stark contrast to the values as reported by Lee, except for the $(U-B)$ colour. To see whether systematic differences between the photometry could explain the anomaly, stars common to both data sets were identified (Figure 5.2) and the difference in colour/magnitude were plotted against colour/magnitude (Figure 5.3). Figure 5.3, shows clearly that the discrepancies are not attributable to systematic differences between the photometry. It is interesting to note the relationships between Lee's photometry and that of the present study. The differences may be attributable to Lee having difficulty in obtaining a good sky estimate in the crowded frame of the cluster centre, the effect of the sky becoming more pronounced at fainter magnitudes, as seen in the lower panel of Figure 5.3. At V=17$^{\rm m}\!.$0 with my system, I expect, by extrapolation, Lee to obtain $V\sim$16$^{\rm m}\!.$7 with his system. Lee reports having a plate limit of $V\sim$16$^{\rm m}\!.$3 and therefore I would not have expected him to have detected LUS. From a close examination of Lee's (1977) Figure 9 showing LUS, it is not at all clear which star is being selected, and I believe that the discrepancy in the photometry may be due to a mismatch by Lee.

5.2 Nature of the Ultraviolet Excess Object

Assuming the object to lie out of the galactic plane, and applying reddening corrections applicable to NGC 3201, intrinsic colours of $(B-V)_0$=$-0\overset{m}{.}28$, $(U-B)_0$=$-1\overset{m}{.}09$ and $(U-V)_0$=$-1\overset{m}{.}37$ are obtained. Assuming LUS to be a cluster member, and correcting for the adopted distance modulus of NGC 3201, an absolute magnitude of M_V=$2\overset{m}{.}88$ is derived. The $(B-V)_0$ and $(U-B)_0$ colours correspond to a spectral class of approximately B0, and hence an effective temperature of around 30,500 °k (Mihalas and Binney 1981). It is interesting to speculate on the nature of LUS. The colours of LUS are consistent with it being a white dwarf. If the object is assumed to be a cluster member, then it is too luminous to be a white dwarf, though the possibility of LUS being a field white dwarf cannot be excluded. Hot subdwarfs have been seen in the globular clusters M4 and M71 by Drukier *et al.* (1989). Hot subdwarfs, along with the central stars of planetary nebula, appear to be the progenitors of white dwarfs. The origin of hot subdwarfs is still speculative, and I point the interested reader to Heber (1986) for further discussion. The possibility of LUS being a hot subdwarf seems a reasonable one: Greenstein and Sargent (1974) determined a mean absolute magnitude for sdB's of M_V=$+3\overset{m}{.}1$ with a dispersion of less than a magnitude, while Heber (1986) determined an average absolute magnitude of M_V=$+4\overset{m}{.}1 \pm 0\overset{m}{.}8$ for sdB/sdOB stars. Downes (1986) determined absolute magnitudes of M_V=$(5\overset{m}{.}0/5\overset{m}{.}3) \pm 1\overset{m}{.}4$ for sdB's, depending on the intrinsic colour adopted. Some other less likely possibilities are listed below.

1.) Quasar: LUS is probably too blue to be a quasar. Richer and Fahlman (1988) state that mean QSO colours are $(U-V)$=$-0\overset{m}{.}6$ with very few bluer than $(U-V)$=$-0\overset{m}{.}8$.

2.) Blue drooper: The horizontal branch of NGC 3201 does appear to drop at an uncorrected colour of $(B-V)$=$0\overset{m}{.}2$ (Figure 4.1). Whether LUS is a blue drooper is open to debate: the paucity of stars between it and the horizontal branch provides a strong case against the notion.

3.) Blue straggler: LUS is too blue, and appears quite distinct from the observed blue stragglers.

To summarize, LUS is probably either a field white dwarf or a hot subdwarf. To make the distinction, a spectrum of LUS is needed.

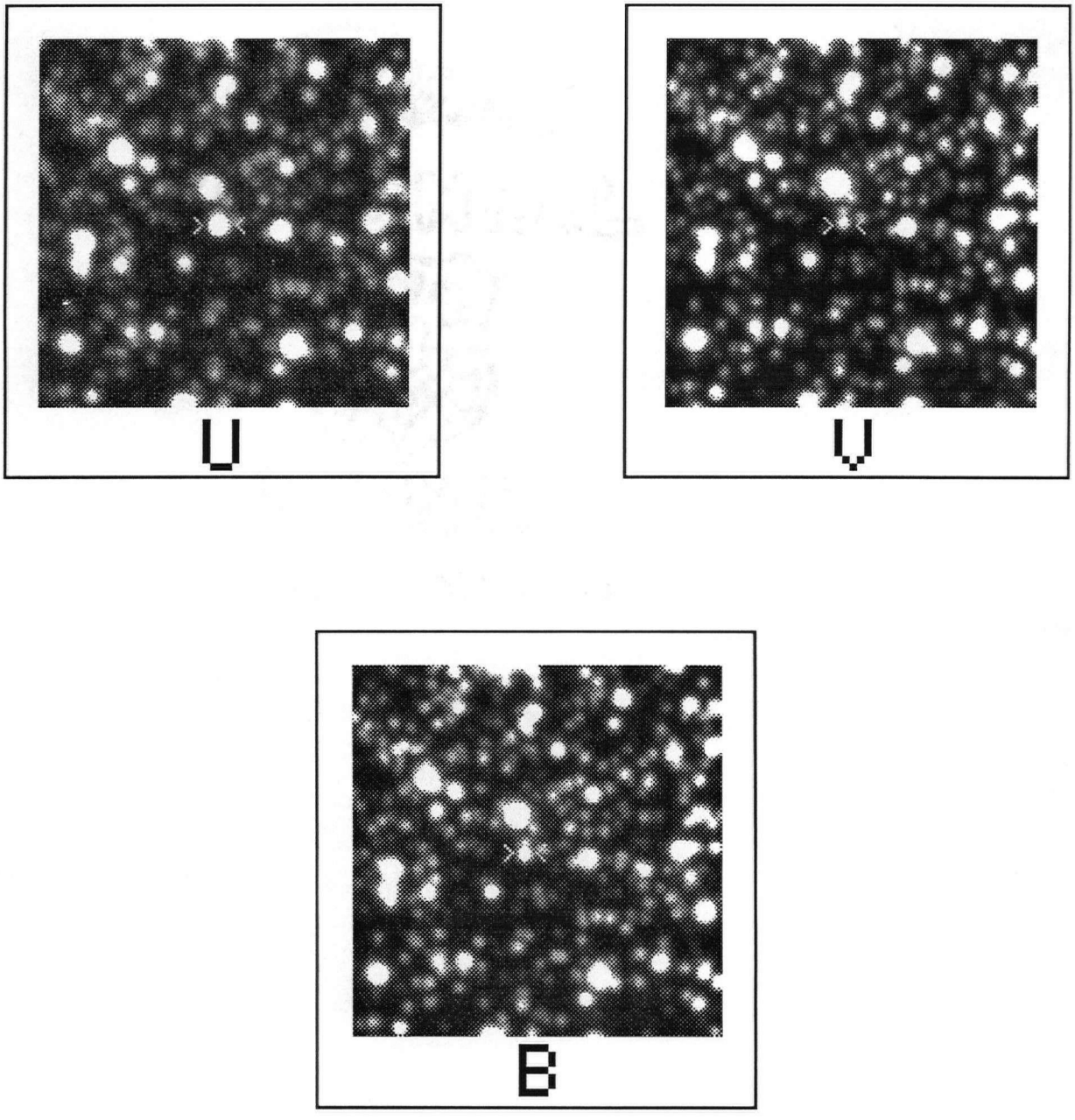

FIGURE 5.1. Lee's unusual star

The star in question is shown between the inequality signs. The letters below the images indicate the filter, and are *U*, *V* and *B*, clockwise from top left, respectively.

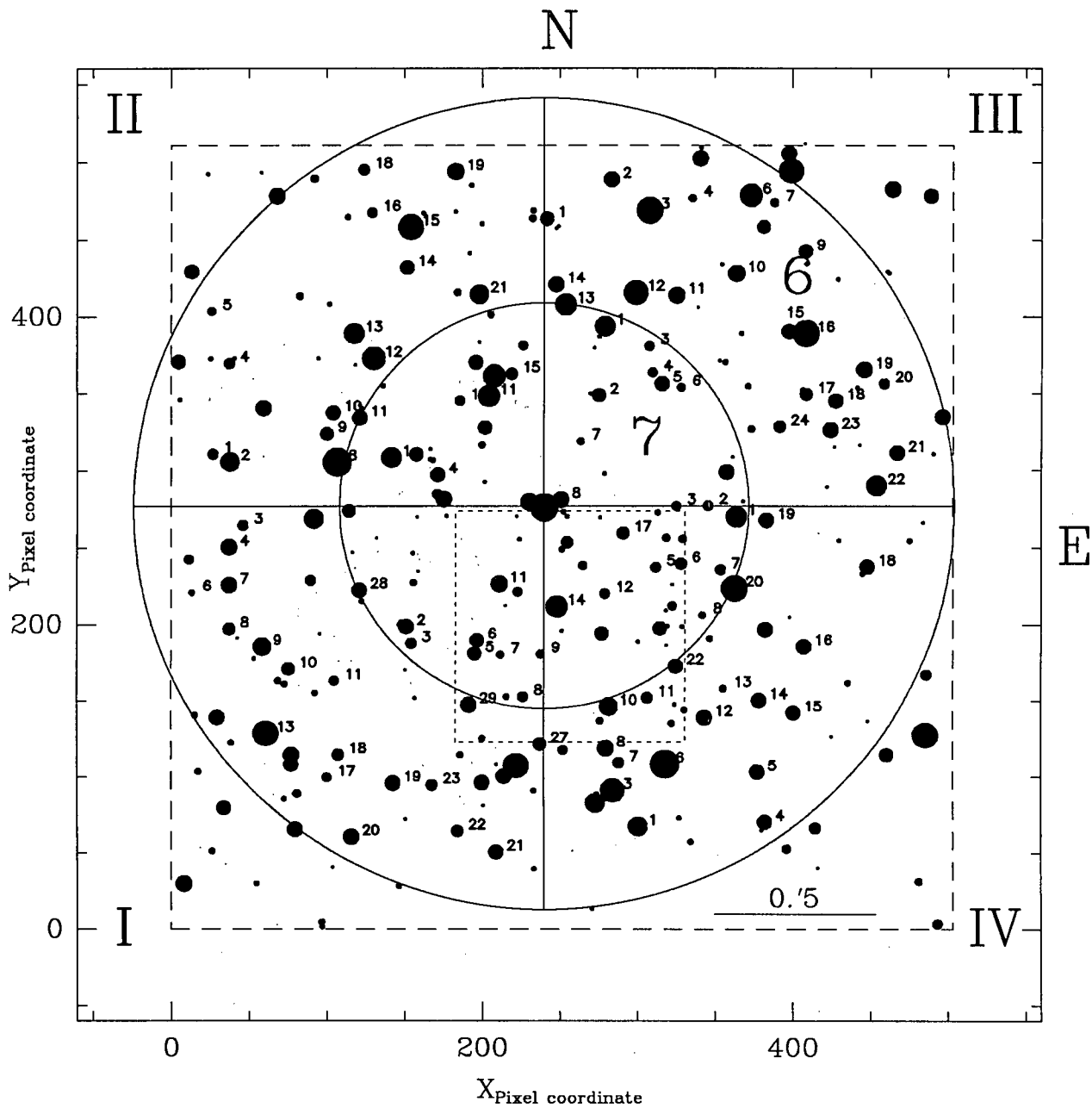

FIGURE 5.2. Finding chart for the TEK program field

The notation in the diagram is similar to that of Lee (1977), with the exception of the pixel coordinates. The dashed line indicates the extent of the TEK program field, while the dotted line indicates the location of the region in Figure 5.1. The numbered stars are used in the comparison of the current photometry with that of Lee's (1977).

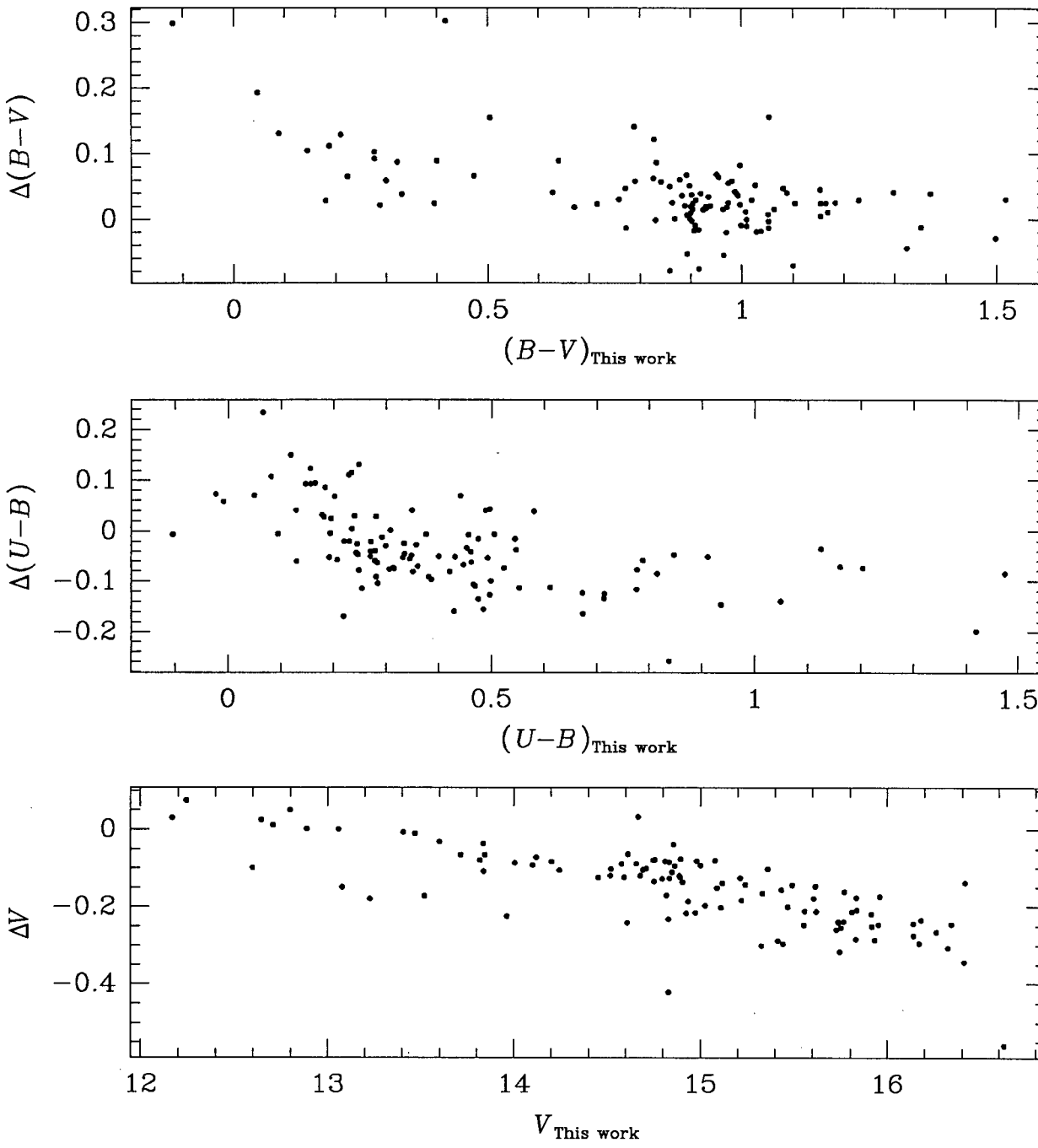

FIGURE 5.3. Comparison with the photometry of Lee (1977)

A comparison between the magnitudes and colours derived from the TEK data for stars in common with the photometry of Lee (1977). The difference, Δ, is in the sense (Lee value – This work).

Chapter 6
STAR COUNTS IN NGC 3201

6.1 Motivation

'The whole is more than the sum of its (luminous) parts'. So it would seem with galaxies anyway. There is now a growing body of evidence, mainly from galactic rotation curves, that a major part of the mass in the Galaxy is locked up in non-luminous matter, generically known as *dark matter*. If the mass function of a globular cluster can be traced to the hydrogen burning limit and is found to be still steeply rising, then it can be inferred that a large amount of the cluster mass is locked up in brown dwarfs. It has been shown (Fich and Tremaine 1990) that the dark matter needed to obtain the Galactic rotation curve can be modeled as a spherical halo of radius 35 kpc. It is believed (Larson 1976, Searle and Zinn 1978) that most globular clusters were destroyed at an early epoch of the Galaxy, their stars now constituting part of the halo. It is tempting to hypothesize that the halo mass function will be similar to cluster mass functions, both the halo and globular clusters belonging to Population II, and also that clusters contain brown dwarfs. Brown dwarfs could then constitute the dark matter needed to account for the galactic rotation curve, and hence aid in demystifying the dark matter enigma.

It has been shown (Richer and Fahlman 1991) that at large core radii in a globular cluster, the mass function of the less massive stars, $\mathcal{M} < 0.4\mathcal{M}_{\odot}$, will have a slope resembling that of the initial mass function (IMF), provided the cluster has not been extensively tidally stripped and that King models are reasonable approximations to globular cluster kinematics, as appears to be the case. The IMF, in the models of Larson (1986), depends critically on the temperature-density relationship of the gas out of which the stars formed. Knowledge of cluster IMFs may thus help place constraints on the physical properties of the gas in the early universe. If a relationship between cluster metallicity and mass function is proved to exist (McClure *et al.* 1986), then this would demonstrate that it is easier to form low mass stars in metal-poor environments, though contemporary thinking errs away from such a relationship.

The luminosity function, which is a first step in deriving the mass function, helps provide a check on the theory of low mass stars. The interior physics of low mass stars is very sensitive to the atmosphere, but the input physics of cool atmospheres is very uncertain. It is believed that a steepening of the mass-luminosity relationship will occur for stars with $\mathcal{M} < 0.5\mathcal{M}_{\odot}$. This

will be reflected in the luminosity function of the cluster, and hence the luminosity function will provide a check on the theory of cool stellar atmospheres.

6.2 Production of Frames for ADDSTAR Tests

The V and I program fields from the TI data were binned 2 × 2, increasing the signal to noise ratio in the images. When binning one must ensure that the stellar profiles are at least still critically sampled, otherwise problems will be encountered with profile-fitting. Standard reductions were performed upon the two binned frames, and IMEXAMINE was used to determine the standard deviation of the sky. The finding threshold was initially set to approximately 3.5 times the sky sigma, but was dropped to a lower value for two of the fields when it was found that fainter stars were not being recovered.

Frames of the background field, located at $\alpha_{1988}=10^{h}\ 38^{m}\ 08^{s}$ and $\delta_{1988}=-46°\ 22'\ 23''$, were taken in V and I (see observations *nee*320 → *nee*326). Observation *nee*321 was binned 2 × 2 to produce the V background frame, whilst observations *nee*323 → *nee*326 were registered, combined and binned 2 × 2 to produce the I background frame.

The parameters for these frames are summarized below.

TABLE 6.1: Characteristics of frames used for ADDSTAR tests

	RON (e pixel^{-1})	Gain (e ADU^{-1})	Sky σ (ADU)	Threshold (ADU)	FWHM (arcsecs)
V Program	3.46	25.2	5	12	1.6
I Program	2.69	42	4.3	14	0.9
V Background	6	8.4	10.5	35	1.3
I Background	3	33.6	7	20	1.1

6.3 Synthetic Star Tests

The efficiency with which stars are recovered from crowded data frames is not known *a priori*, it will depend, *inter alia*, on the crowding in the frame, the PSF profile (and hence seeing and guiding) and routines employed in the reduction. These factors affect the efficiency in ways that are hard to determine analytically. To overcome this lack of knowledge, a Monte Carlo technique is employed, where synthetic stars are added into a data frame, and then the data frame is reduced to determine the efficiency with which stars are found. The DAOPHOT routine, ADDSTAR, will generate synthetic stars, with the appropriate Poisson shot noise, and

add them to a data frame. The luminosity function (LF) of the stars used for the ADDSTAR tests should be as similar as possible to the true LF, so that the correction factors calculated will be applicable to the real stars in the frame. Consider, for example, what will happen if real stars are biased to one side of a bin, and a correction is calculated with an even distribution of synthetic stars across the bin, with the finding efficiency rapidly changing, *viz.*: the correction applied will be erroneous. Ideally, one would guess the form of the LF, add n per cent of this LF into the frame, evaluate the corrections and deduce a corrected LF. One would then iterate on this method, adding in n per cent of the latest corrected LF until convergence of the LF was found. This method was deemed inappropriate, due to the exorbitant amount of computing time required. In lieu of iteration, a "Guessed Luminosity Function" (GLF) was produced. The GLF was created by performing a standard reduction on the frame under question, and producing its uncorrected LF. For the brighter stars on the frame, it is a good assumption that they are all recovered. The turnovers seen in uncorrected LFs (see, for example, Figure 6.3) were assumed, and later found, to be due to the inefficiency in the recovery of the fainter stars. To generate the GLF I extrapolate the LF of the bright end to the faint end assuming, *a priori*, that the turnover is due to incompleteness in the recovery of the fainter stars. Having the GLF then allows a file to be generated containing stars at an n per cent level of the GLF, with a random spatial distribution on the frame. ADDSTAR is then used to add the stars into a frame, and the new frame has a standard reduction performed upon it to determine the efficiency with which the synthetic stars are recovered.

When a synthetic star is recovered, it is possible to make a comparison of its recovered magnitude with its added magnitude. This was done for both the V and I binned program fields, and is shown in Figure 6.1. One notices the scatter to be fairly symmetrical at brighter magnitudes, but at fainter magnitudes there is a tendency for the recovered magnitude to be larger, *i.e.* fainter than the added magnitude. This is contrary to what is expected, one would expect the stars to be recovered at brighter magnitudes, due to them being on noise spikes. No explanation is offered, though it does seem to be the case for stars with $I > 23\overset{m}{.}0$. A star was only counted as a recovery if the difference between its added and recovered magnitudes was smaller than $0\overset{m}{.}7$, in accordance with Fahlman *et al.* (1989).

6.4 Robustness of the Technique

To determine the robustness of the Monte Carlo technique, it was decided to see what effect adding stars at varying levels would have on the corrected LF. A GLF was generated for the

binned *I* frame, and ADDSTAR tests were performed at the 5, 25, 75 and 100 per cent levels of adding. Figure 6.2 shows the *I* frame with these various levels of stars added, while Figure 6.3 shows the derived uncorrected luminosity functions for these frames. Fewer of the fainter stars are found on the more crowded frame, as can be seen from the middle panel of Figure 6.6. Note that in the middle panel there is a point for which more stars are found on the crowded frame, I attribute this to counting noise: at the faint magnitude associated with the point, only about sixty stars are recovered. Figure 6.4 shows the recovery efficiency for stars on the frames. Comparing the 5 per cent and the 100 per cent add levels, see Figure 6.6, it is seen that in the less crowded frame stars are recovered with a higher efficiency, as expected. Figure 6.5 shows the corrected luminosity functions derived using the frames. The 75 per cent and 100 per cent diagrams show a sharper upturn at faint, $I > 18\overset{m}{.}0$, magnitudes where the incompleteness is high. *viz*: The corrected luminosity functions for the crowded frames contain more faint stars than the corrected luminosity functions for the less crowded frames, as shown in the lower panel of Figure 6.6. I propose that this is due to noise spikes being detected; the probability of detecting a noise spike *is not* that of finding a star, the stellar image being a distributed function. As the higher add levels are more incomplete (Figure 6.4) a larger incompleteness correction is applied to the same noise spikes, hence causing the sharper upturn. Comparing the 5 per cent and the 100 per cent corrected luminosity function graphs, it is seen that the less crowded frame *goes deeper* than the more crowded frame. The derived LFs for these two frames are in good agreement up to where the completeness drops below 50 per cent.

From these tests it was concluded that adding stars at a 10 per cent level will not adversely affect the derived LF, the differences between 5 per cent and 100 per cent only becoming manifest at faint magnitudes where the incompleteness is high. All subsequent results were derived by adding synthetic stars to the frames at the 10 per cent level.

6.5 Comparison with the Bahcall and Soneira Galaxy Model

The Bahcall and Soneira (1980, 1984) Galaxy model consists of an exponential disk, representing Population I stars, and a de Vaucouleurs spheroid for modeling the Population II stars. Symmetry is assumed about a north-south direction and also the direction of the galactic centre. Ratnatunga and Bahcall (1985) calculated the expected number of field stars in the direction of 76 globular clusters with $|b| > 10°$ using the above model. NGC 3201, with a galactic latitude of $8\overset{\circ}{.}64$ is not included, and the authors give the below warning.

"The estimates given for the 32 globular clusters with $20° > b > 10°$ and for all fields with $V > 22$ must be used with special caution because these regions are outside the galactic latitude or apparent magnitude range over which the galaxy model has been tested."

With these facts noted, a comparison is made. The corrected counts are shown in Table 6.2. The counts for the clusters NGC 2808 and NGC 6101 were multiplied by 4.6, so as to have the same sky coverage as the TI frame.

Figure 6.7 shows stars which were matched between the TI background field I and V frames, along with the magnitude bins as used by Ratnatunga and Bahcall, and the incompleteness in V each bin. The completeness corrections were calculated using PSFs, and so should be applied to stars only, not noise. To try and ensure this was happening, the stars were counted in two ways. The column headed *unmatched* is the corrected number of stars counted in each V bin, and is susceptible to noise contamination at the faint end. The *matched* column is the number of stars in each V bin *which were also found on the I frame.* By setting this criterion, a lot of noise is rejected and the counts should be more reliable. The I data are fairly complete to around $22\overset{m}{.}0$; the last V bin may have too few stars due to incompleteness in I. The stars in the last V bin span a range of $20\overset{m}{.}5 < I < 25\overset{m}{.}0$, and it is not obvious how to correct for this incompleteness. The matched and unmatched counts show good agreement in all but the last two bins. The discrepancy is vindicative of noise contamination in the last two bins.

TABLE 6.2: Comparison of counts with the Bahcall and Soneira model

Range in V	NGC 3201, Background Field l=280°.34, b=10°.54		NGC 2808 l=282°, b=−11°.3	NGC 6101 l=317°, b=−15°
	unmatched	*matched*		
$13 < V < 15$	0	0	0.92	1.012
$15 < V < 17$	4	4	3.588	3.864
$17 < V < 19$	19	19	11.5	11.96
$19 < V < 21$	26	26	22.08	23.26
$21 < V < 23$	79	53	33.58	37.26
$23 < V < 25$	1806	230	59.8	64.4

Comparing the counts for NGC 2808 and NGC 6101, one sees that they are similar. When symmetry considerations are taken into account, the Galactic coordinates of the TI background field differ from those of NGC 2808 less than NGC 2808 differs from NGC 6101. With this observation the assumption is made that the NGC 3201 counts should be similar to those of NGC 2808. This is approximately seen for $13\overset{m}{.}0 < V < 21\overset{m}{.}0$, but divergence is seen thereafter. One

has to be careful about drawing conclusions as the model was never meant for the low galactic latitudes of NGC 3201, though I tentatively suggest that the Bahcall and Soneira model predicts too few faint stars at low galactic latitudes. Fahlman, Richer and VandenBerg (1985) found a similar effect for M15, with l=25° and b=27°, where too few faint stars were predicted by the Bahcall-Soneira standard Galaxy model. The divergence from the models is a clear warning *not to use the model to correct for faint background stars.*

6.6 Mass-Luminosity Relationships

A mass-luminosity relationship (MLR) is a relationship between magnitude, in this case V or I, and stellar mass. The MLR, like an isochrone, is dependent on the stellar model, *i.e.* the luminosity is not only a function of mass. The MLR will change as the cluster ages, and will also be a function of metallicity, mixing length parameter, helium content and other less significant factors. The MLR I adopt for the Johnson V band in this work is that of Drukier *et al.* (1988), which was obtained using a 16 Gyr VB85 isochrone, and points which extend the relationship down to $\mathcal{M} = 0.15\mathcal{M}_{\odot}$ (Figure 6.8). The MLR is applicable to stars with a metallicity of [Fe/H]=−1.27.

The I band MLR was derived by using the MLR of Fahlman *et al.* (1989) and the models of VB85. Points were read off the Fahlman *et al.* MLR, and splined to points from the VB85 16 Gyr isochrone. It was found that to ensure a smooth transition between the two sets of points, the brighter end of the Fahlman *et al.* relationship had to be truncated, see Figure 6.9. The Fahlman *et al.* relationship was derived from LFT (Luyten Five Tenths Catalogue, Luyten 1955) subdwarfs, observed by Rodgers and Eggen (1974), and the models of D'Antona (1987). I refer the interested reader to Fahlman *et al.* for more details. The I band MLR adopted was applicable to Population II stars of intermediate metallicity, and an age of 16 Gyr. Figure 6.10 shows the effect of having alternate ages for the MLR, and it is seen that changing the age of the cluster will not have a large effect for stars less massive than $0.7\mathcal{M}_{\odot}$. The MLRs are applicable only to main sequence stars.

6.7 Error Propagation in ADDSTAR Tests

To derive the mass function in the program field it is necessary to count the stars in magnitude bins. The stars actually counted on a frame have to be corrected for incompleteness. Denoting N_C as the number of cluster members in a particular bin, we have $N_C = N_F - N_B$ with N_F and N_B being the field and background counts in the same magnitude bin, after being corrected for

incompleteness. Denoting IC as the incompleteness correction and RC as the raw counts,

$$\begin{aligned} \mathrm{N_F} &= \mathrm{IC_F} \times \mathrm{RC_F} \\ \mathrm{N_B} &= \mathrm{IC_B} \times \mathrm{RC_B}. \end{aligned} \tag{6.1}$$

Propagation of errors leads to the expression

$$\sigma_{\mathrm{N}} = \left(\left(\frac{\sigma_{\mathrm{IC}}}{\mathrm{IC}} \right)^2 + \left(\frac{\sigma_{\mathrm{RC}}}{\mathrm{RC}} \right)^2 \right)^{\frac{1}{2}}, \tag{6.2}$$

for either the field or background frames. The error in the raw counts is given by the Poissonian counting error, $\sqrt{\mathrm{N}}$.

The statistics of ADDSTAR tests are described well by the binomial distribution (Bolte 1987). The standard deviation of the binomial distribution is given by

$$\sqrt{\mathrm{np}(1-\mathrm{p})}, \tag{6.3}$$

where n is the number of trials, equivalent to number of stars added, and p is the probability of success, equivalent to the number of stars recovered divided by the number of stars added. Defining $\mathrm{N_A}$ as the number added, and $\mathrm{N_R}$ as the number recovered then yields

$$\sigma(\mathrm{N_R}) = \mathrm{N_R} \sqrt{\left(\frac{1}{\mathrm{N_R}} - \frac{1}{\mathrm{N_A}} \right)} \quad . \tag{6.4}$$

Defining IC as $\left(\frac{\mathrm{N_R}}{\mathrm{N_A}} \right)$,

$$\left(\frac{\sigma_{\mathrm{IC}}}{\mathrm{IC}} \right)^2 = \left(\frac{\sigma_{\mathrm{A}}}{\mathrm{N_A}} \right)^2 + \left(\frac{\sigma_{\mathrm{R}}}{\mathrm{N_R}} \right)^2 \quad . \tag{6.5}$$

The number of stars added to the frame is a known quantity and so σ_{A} will be zero. Having the error in the incompleteness corrections will then allow the errors in the background and field counts to be determined. These errors are added in quadrature to determine the error in $\mathrm{N_C}$.

The error in $\frac{dN}{d\mathcal{M}}$ is evaluated by dividing the error in the true counts by the width of the mass bin. The MLR is assumed to have no error, and so $d\mathcal{M}$ is also assumed to be error free.

6.8 The Mass Function

The derived LFs from the program fields consist of two components; a cluster component and a field component. The field component consists of background and foreground objects not associated with the cluster. To determine the true cluster LF, it is necessary to produce a LF for the background fields and then, assuming the background distribution to be homogeneous and hence the background contribution to the program frame to be similar to the background frame, subtract the background LF from the program field LF. This procedure should automatically make corrections for galaxy contamination; the same finding routines are employed on both frames.

Taking $E(B-V)$=0$^{m}\!.$21 and $(m-M)_V$=14$^{m}\!.$2 for NGC 3201, the absorption in the V band will be

$$A_V = R_V \times E(B-V) = 0.65, \tag{6.6}$$

where R is taken to be 3.1, in accordance with Savage and Mathis (1979). This yields a true distance modulus of 13$^{m}\!.$55 for NGC 3201. Cohen *et al.* (1981) give that

$$A_I = 0.6 \times A_V, \tag{6.7}$$

the application of which then gives $(m-M)_I$=13$^{m}\!.$94.

Applying the colourless transformation equations (§3.4.3) to ALLSTAR magnitudes from the V and I program fields and correcting the values for the appropriate distance modulus yields absolute magnitudes for the cluster members.

The V and I background frames were reduced using standard reductions, and GLFs were built. The frames had ADDSTAR tests, at a 10 per cent level of the GLF, performed upon them. The ALLSTAR magnitudes of objects detected on the background frame were calibrated to standard magnitudes (§3.3), and corrected for the appropriate distance modulus, V or I, of the cluster. This ensured that the background stars appeared in appropriate magnitude bins to allow the calibrated program field counts to be corrected. Cluster counts were derived by applying incompleteness corrections to the magnitude bins, and then subtracting the background counts from the field counts. At bright magnitudes, where there is a paucity of stars, it is possible for the cluster count to be negative due to the effects of small number statistics.

The quantity ϕ is defined as

$$\phi \equiv \frac{d\mathrm{N}}{d\mathcal{M}} \ , \tag{6.8}$$

with N representing number of stars and $\mathcal{M}$ representing mass. The quantity ϕ is a continuous function, though I only derive the mean value in a bin. To obtain ϕ for a bin, the mass at the bin ends is evaluated, and the change in mass is derived. The number of stars in the bin is then divided by the change in mass to yield a value for ϕ.

Mass functions were derived from the V and I frames in two ways. The first way was to count the stars in magnitude bins, the bins having a width of $0\overset{\mathrm{m}}{.}5$ and an interval of $0\overset{\mathrm{m}}{.}25$ so that the bins overlap. A bin width of $0\overset{\mathrm{m}}{.}5$ was chosen as a compromise between resolution and Poisson-counting noise. This produced the mass functions shown in Figures 6.11 and 6.12. Figure 6.13 shows the two mass functions superimposed. These mass functions have been corrected for background counts, and points were only plotted if the uncorrected number of cluster stars was larger than ten. Comparing the mass functions derived using the V and I frames, one notices considerable differences between them, for example the two minima seen in the 'I mass function', located at approximately -0.2 and -0.4 in $\log_{10}\left(\frac{\mathcal{M}}{\mathcal{M}_\odot}\right)$, which do not appear in the 'V mass function'. One would intuitively not expect there to be a difference since the same stars are being counted.

A possible explanation of this anomaly may be that the star colours are inconsistent with the MLRs. To check this, a synthetic isochrone was generated by evaluating V and I magnitudes at equal masses on the two MLRs. The isochrone was plotted in the $(V-I)$, I plane, along with the calibrated data from a standard reduction on a binned V frame and a binned I frame, see Figure 6.14. One sees that the synthetic isochrone is a good fit to the data. The fact that the isochrone fits the data to its limiting magnitude lends credence to the MLRs of Fahlman *et al.* (1989) and Drukier *et al.* (1988), especially as the extensions to the VB85 isochrones, for each of the MLRs, were derived in alternate ways.

To make a more direct comparison between the two mass functions, it was decided to bin on the mass interval, as opposed to the magnitude interval so that, bin jumping aside, *exactly* the same stars would be counted in the same bins.

The magnitude intervals corresponding to mass intervals of $0.05\mathcal{M}_\odot$ were calculated using the V and I MLRs. Stars on the program and background frames were counted in these bins, and the applicable corrections were derived by considering the stars added and recovered from

each of these bins. Figures 6.15 and 6.16 show the two mass functions derived in this way before any background corrections, and Figures 6.17 and 6.18 show the mass functions after the background corrections. One immediately notices that the two minima seen in the '*I* mass function' are still present and still do not appear in the '*V* mass function' for both the corrected and uncorrected mass functions. To explain these anomalies between the mass functions, plots were made of *I* magnitude against *V* magnitude of stars in both the field and background frames (Figures 6.19 and 6.20). The results from a single reduction are expected to be very similar to the average of the results of twenty reductions, the number of ADDSTAR tests used to derive the mass function. These graphs show the magnitude equivalent of equally spaced mass bins, and the completeness corrections applied in each bin. The stars found in boxes running from bottom left to top right are stars which are located in the correct bins in both colours, whereas stars located in the off-diagonal boxes have 'bin jumped'. Bin jumping is inevitable using bins, and will not have an adverse effect on the results *provided* that the scatter is symmetrical about bin intersections. A calibration error may cause the points to be asymmetric. It is hard to decide whether such an error exists in the present data, but it appears not. Considering the third bin, which shows a discrepancy between the mass functions, one sees that, assuming all the completeness corrections to be unity,

$$\begin{aligned} V: \quad & N_C = C_d + 20 \\ & N_B = B_d + 3 \end{aligned} \tag{6.9}$$

$$\begin{aligned} I: \quad & N_C = C_d + 14 \\ & N_B = B_d + 14. \end{aligned}$$

In the above notation, N represents the total number of stars in the cluster or background bin, while $(C/B)_d$ is the number of stars in the 'on-diagonal' box, indicated by the intersection of the arrows in Figures 6.19 and 6.20. Before correcting for background counts, the third *I* bin has a deficit of six stars as compared to the third *V* bin, this is sufficient to explain the discrepancies seen between the mass functions in figures 6.15 and 6.16. After correcting for background counts, the number of stars in the third mass bin, derived using the *V* data will be

$$(C_d - B_d) + 20 - 3,$$

while for the *I* data it is

$$(C_d - B_d) + 14 - 14.$$

The anomaly, far from being corrected, is now worse. The difference between the two values is sufficient to explain the lower value seen in the third bin of the background corrected mass function that was derived using the *I* data.

The anomaly between the two mass functions is caused by asymmetrical scattering and stars with 'wrong' colours, for which the MLRs are not applicable. If the stars on the 'off-diagonal' bins were not to be counted, on the premise that their colours are inconsistent with the isochrone, and therefore the MLR is not applicable to them, then stars with genuine scatter would be lost, especially at bin intersections and at fainter magnitudes. If one is to count the off diagonal stars then the validity of the MLR to these stars must be questioned. For this thesis, it was decided that off-diagonal stars would be counted.

6.9 Implications of the Mass Function

The mass function of NGC 3201 is found to have a similar morphology to previously derived mass functions (e.g. see Richer *et al.* 1991, henceforth RFBFST). In common with RFBFST, an upturn is found in the mass function for stars with $\mathcal{M} < 0.4\mathcal{M}_{\odot}$. Fitting the three points corresponding to masses less than $0.4\mathcal{M}_{\odot}$, for which the completeness is greater than 50 per cent, yields a value for x of approximately 1.9. If the last point shown in Figure 6.18 were to be taken into consideration, the mass function would be found to be more steeply rising, but the validity of this last point must be questioned due to its large incompleteness. *No evidence whatsoever is seen for a flattening of the mass function at lower masses.* Assuming the last point to be valid, I can state that no downturn is seen in the mass function down to a mass of approximately $0.2\mathcal{M}_{\odot}$. An extension of the mass function into the brown dwarf region[1] is then suggested by continuity arguments; there being no known reason for a cut off in the star formation at the hydrogen burning limit.

Table 6.3 is from RFBFST, with the addition of NGC 3201. The value of x is for $\mathcal{M} < 0.4\mathcal{M}_{\odot}$, while the third column is the half-mass relaxation time, $T_{1/2}$, from Binney and Tremaine (1987), and the fifth and sixth columns are the concentration parameter, c, and metal abundance, [M/H], taken from Webbink (1985). The entry in the fourth column, T_D, is what RFBFST term as the "time until destruction" and is the inverse of the "destruction rate" for the cluster, as calculated by Aguilar, Hut and Ostriker (1988).

---

[1] In the Population II regime, the hydrogen burning limit is believed to lie in the range $0.09\mathcal{M}_{\odot} \leq \mathcal{M}_{\rm min} \leq 0.11\mathcal{M}_{\odot}$ (D' Antona 1987).

TABLE 6.3: Properties of clusters with derived mass functions extending well below $0.4\mathcal{M}_{\odot}$

Cluster	x	log $T_{1/2}$	T_D	c	[M/H]
M13	2.7	9.40	7.1	1.4	−1.6
NGC 6752	2.5	8.94	7.1	1.6	−1.6
ω Cen	2.1	9.96	6.7	1.2	−1.6
NGC 3201	1.9	9.14	6.25	1.55	−1.6
M 5	1.3	9.44	4.5	1.8	−1.6
NGC 6397	0.9	8.47	2.5	1.6	−2.0
M 71	0.5	8.35	2.9	1.1	−0.5

RFBFST conclude from the six clusters in their study that there is no correlation between the mass function slope and the concentration parameter or the metallicity. This conclusion weighs heavily against the McClure (1986) effect where a correlation between x and [Fe/H] is proposed. RFBFST suggest that there is a weak correlation between x and the half-mass relaxation time, and a strong correlation between x and the destruction time. It is seen that the results for NGC 3201 provide no contradiction between these correlations. Figure 6.21, adapted from RFBFST, shows plots of the destruction time and the half-mass relaxation times against x.

A possible interpretation of the results is that all globular clusters start with mass function slopes of approximately three, which are modified due to dynamical processes (RFBFST). Mass segregation is faster in clusters with short relaxation-times, resulting in an enhancement of low-mass stars in the outer parts of the cluster. The lower-mass stars are preferentially stripped when the cluster transits the Galactic plane. This can explain the positive correlation seen between half-mass relaxation time and mass-function slope; clusters with larger half-mass relaxation times have lost fewer of their low-mass stars. A stronger correlation between 'time until destruction' and x would then be anticipated, as T_D takes account of *all* the processes thought to be important in modifying the MF of the cluster.

The derived MF slopes of globular clusters can be taken as lower limits on the slope of the IMF. If the halo mass-function is similar to that of the globular clusters, then it will also have a steep slope at low masses. Extrapolation of the halo mass-function into the brown dwarf region suggests a large population of brown dwarfs in the halo, and hence a large mass-to-light ratio. A large mass-to-light ratio in the halo would have a significant bearing on Galactic structure.

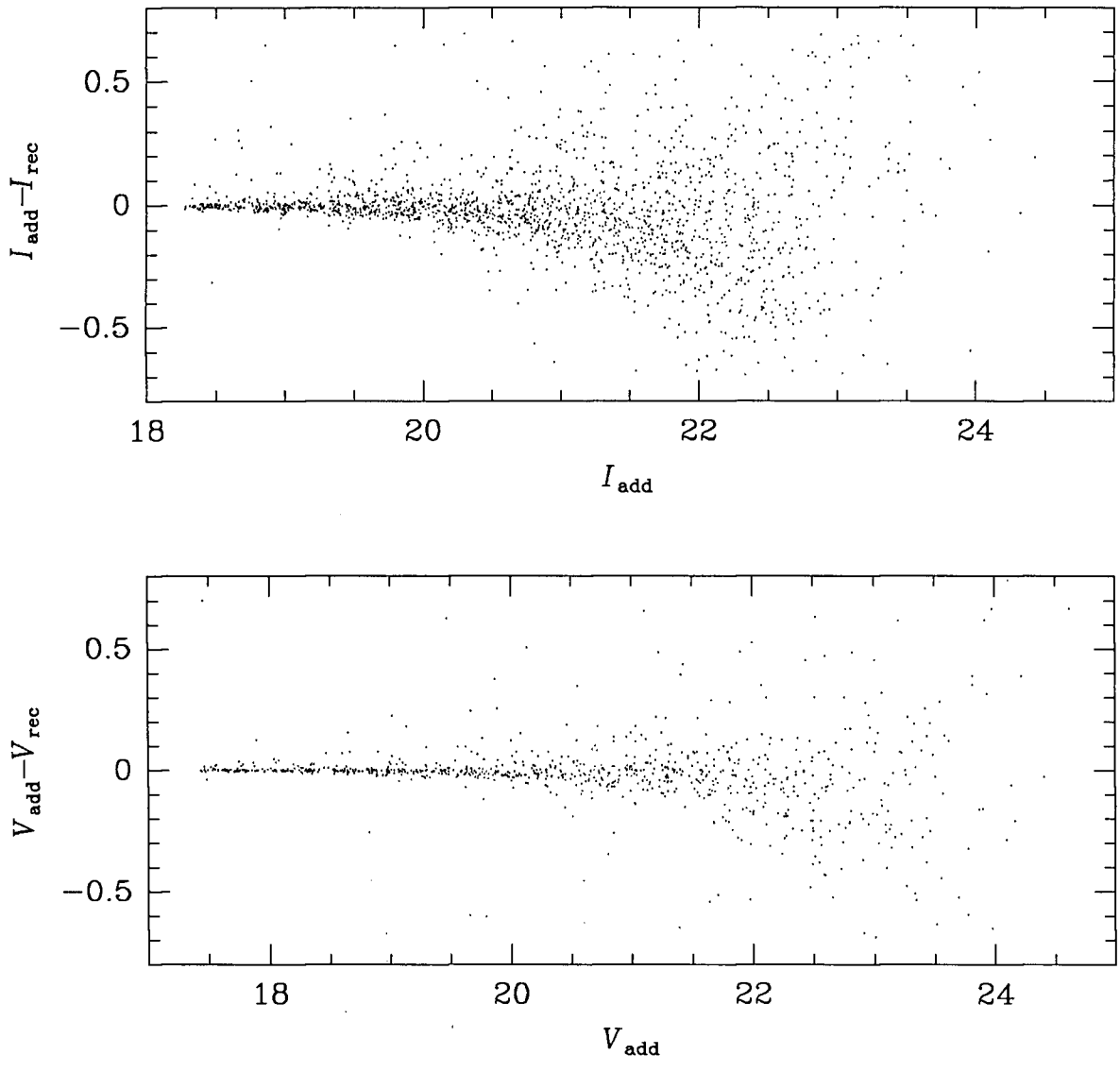

FIGURE 6.1. Error diagram for synthetic stars added to the binned TI program field frames

The subscripts 'add' and 'rec' refer to the magnitudes at which the synthetic star was added and recovered. Stars below the zero line on the ordinate were recovered at a fainter magnitude at which they were added, and *vice versa*.

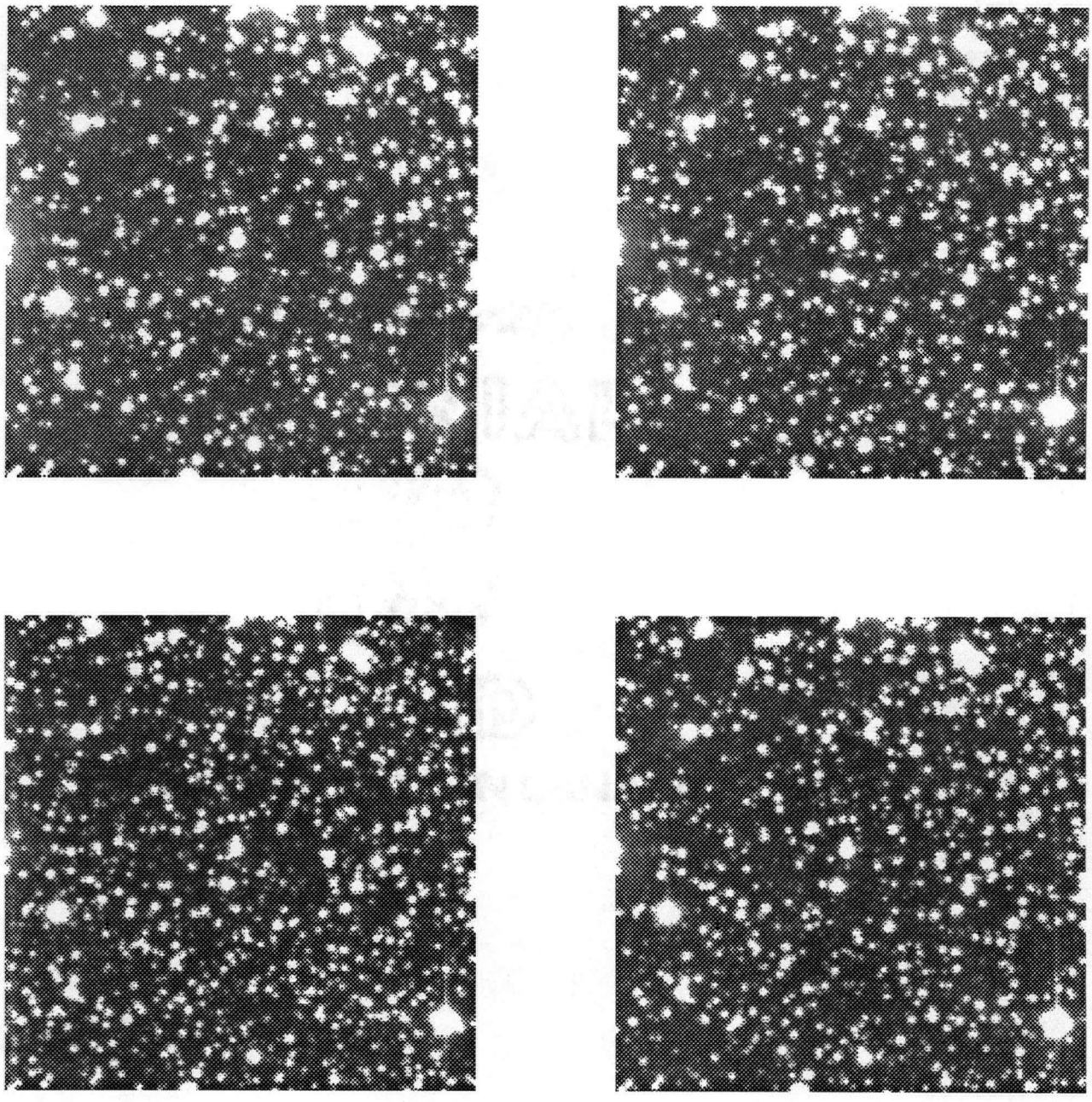

FIGURE 6.2. Varying crowding conditions on the I program field

From top left, going clockwise, the percentage add levels are 0, 25, 75 and 100 per cent.

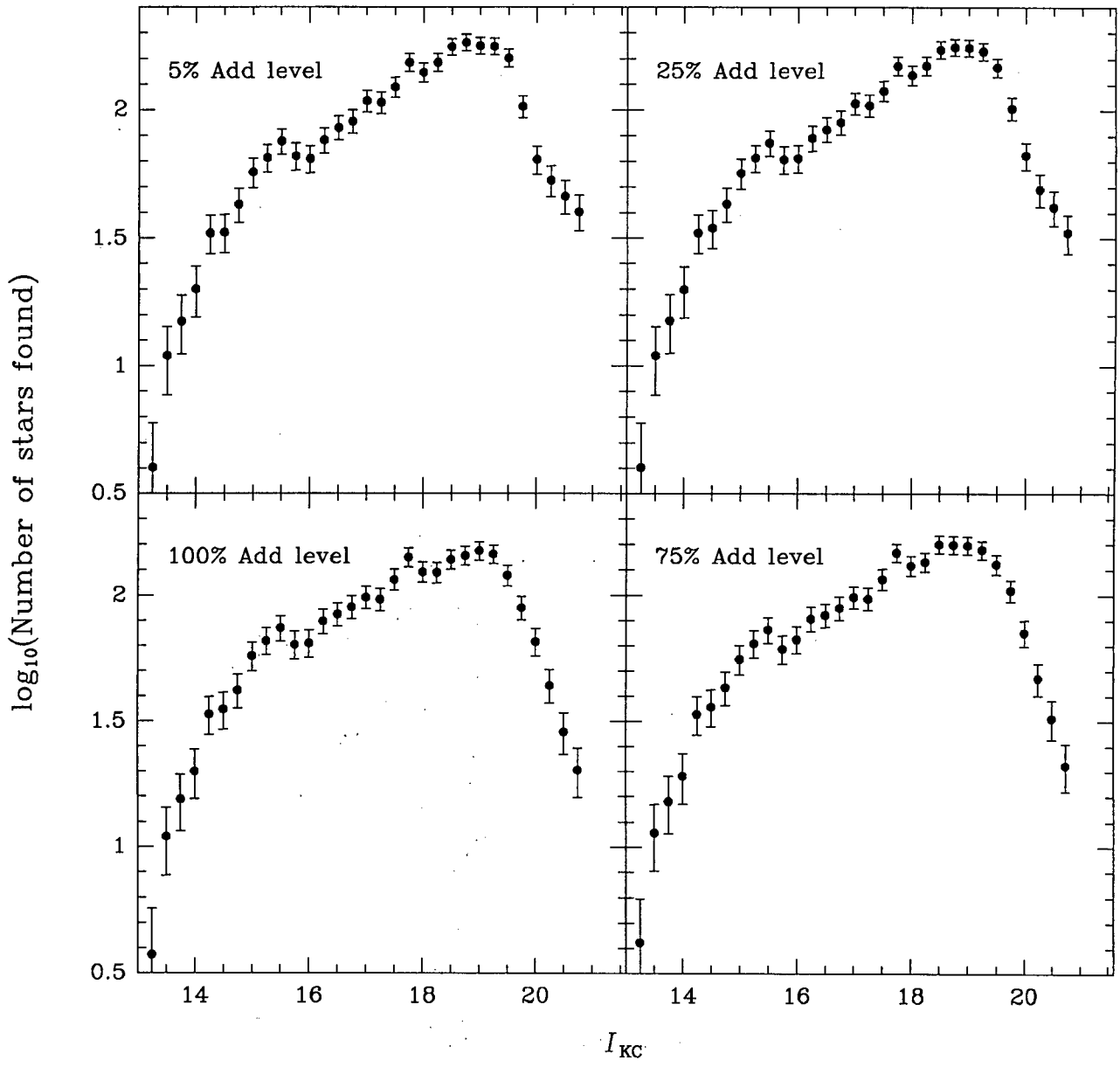

FIGURE 6.3. Uncorrected luminosity functions for various crowding conditions

The above plots were generated by adding stars to the TI binned *I* program field at varying levels. Differences in the morphologies only become manifest after the turn over, the fainter stars being lost on the more crowded frames. (*N.b.* only real stars are counted.)

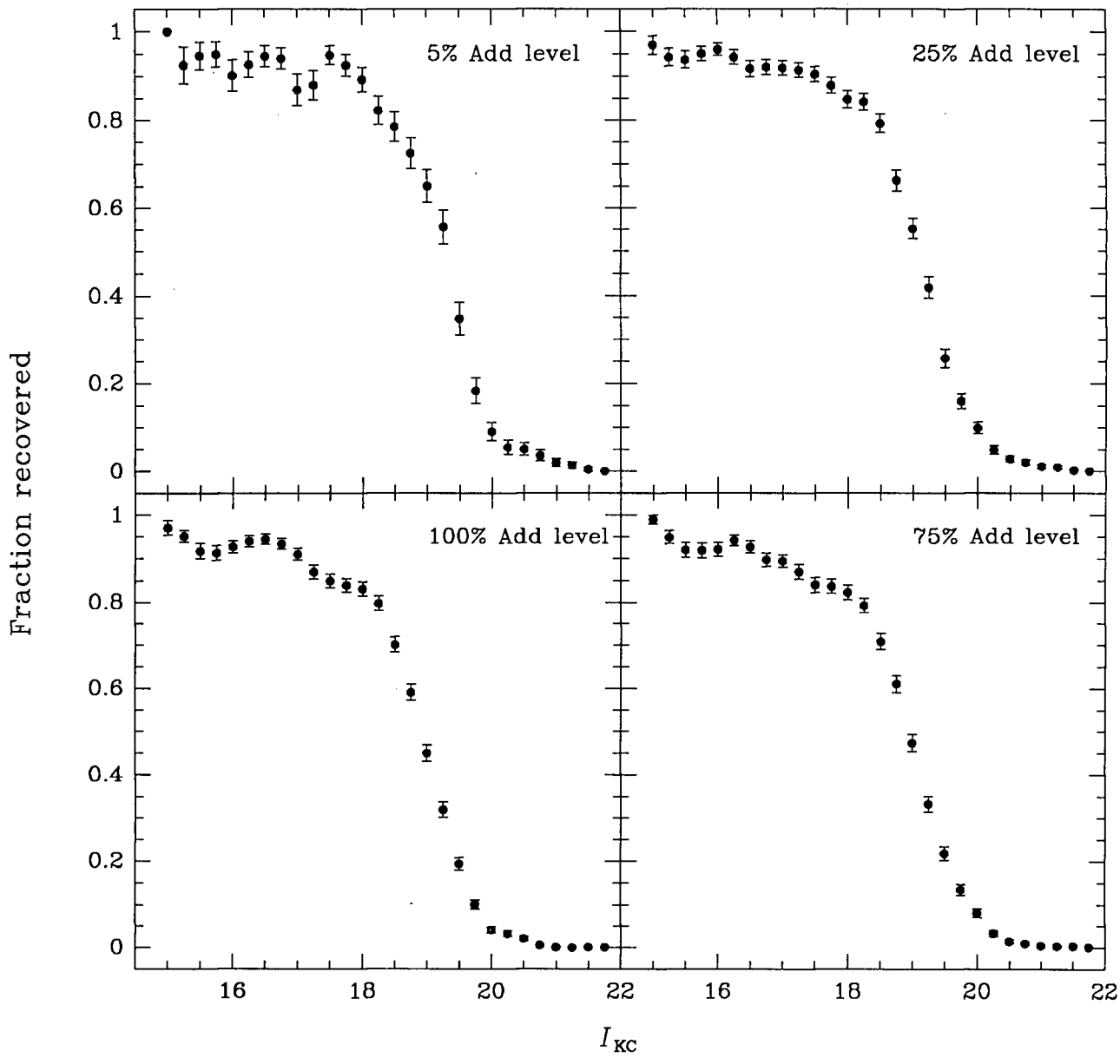

FIGURE 6.4. Recovery efficiency for various crowding conditions

The above plots were generated by adding stars to the TI binned *I* program frame at varying levels. At 100 per cent, more stars are 'lost' and hence the luminosity function cannot be determined to such faint magnitudes, this effect is attributable to crowding.

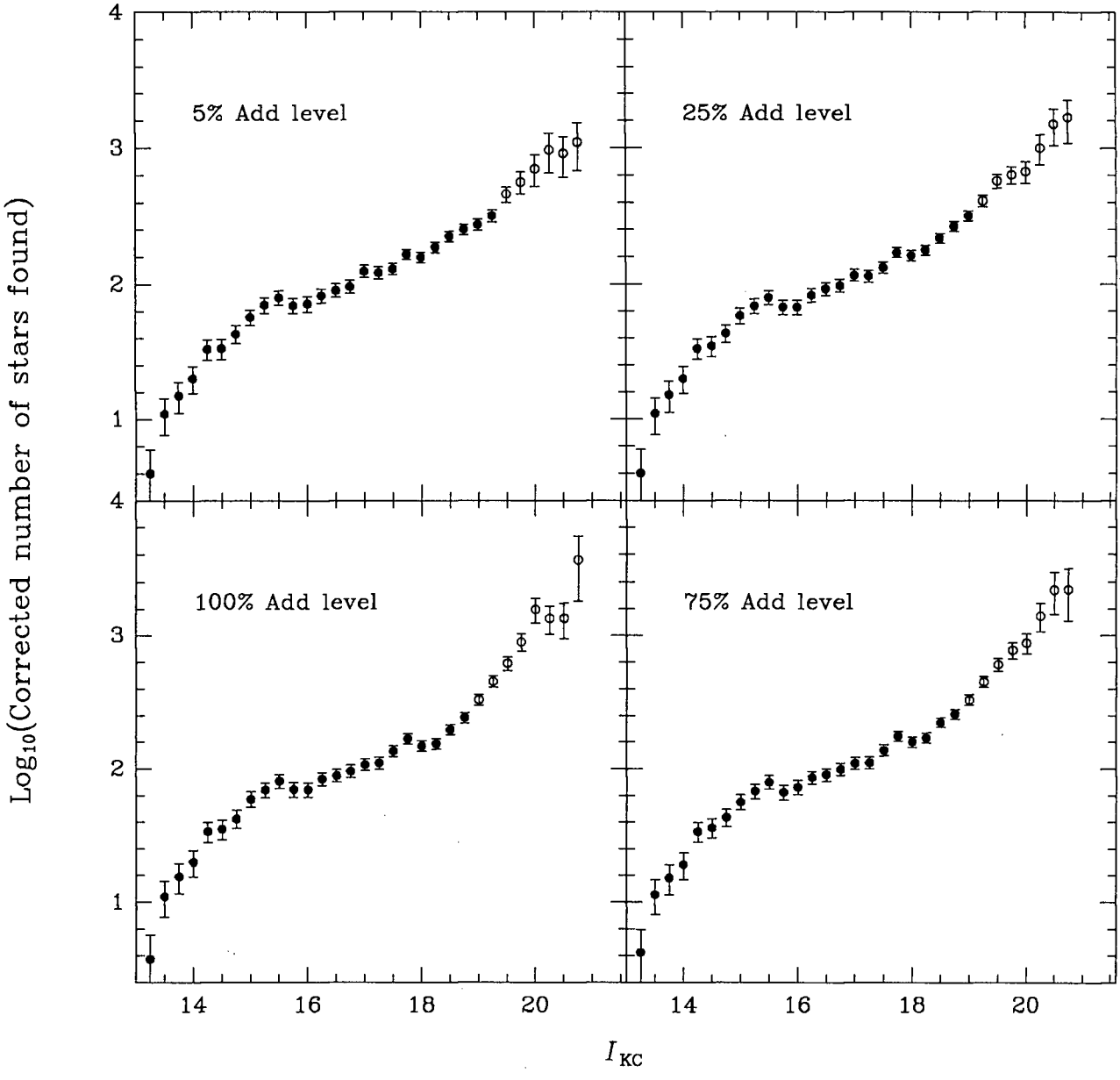

FIGURE 6.5. Corrected luminosity functions for various crowding conditions

The above plots were generated by adding stars to the TI binned *I* program frame at varying levels. The open circles indicate bins in which the completeness was less than 50 per cent. The difference in the morphologies is discussed in the text.

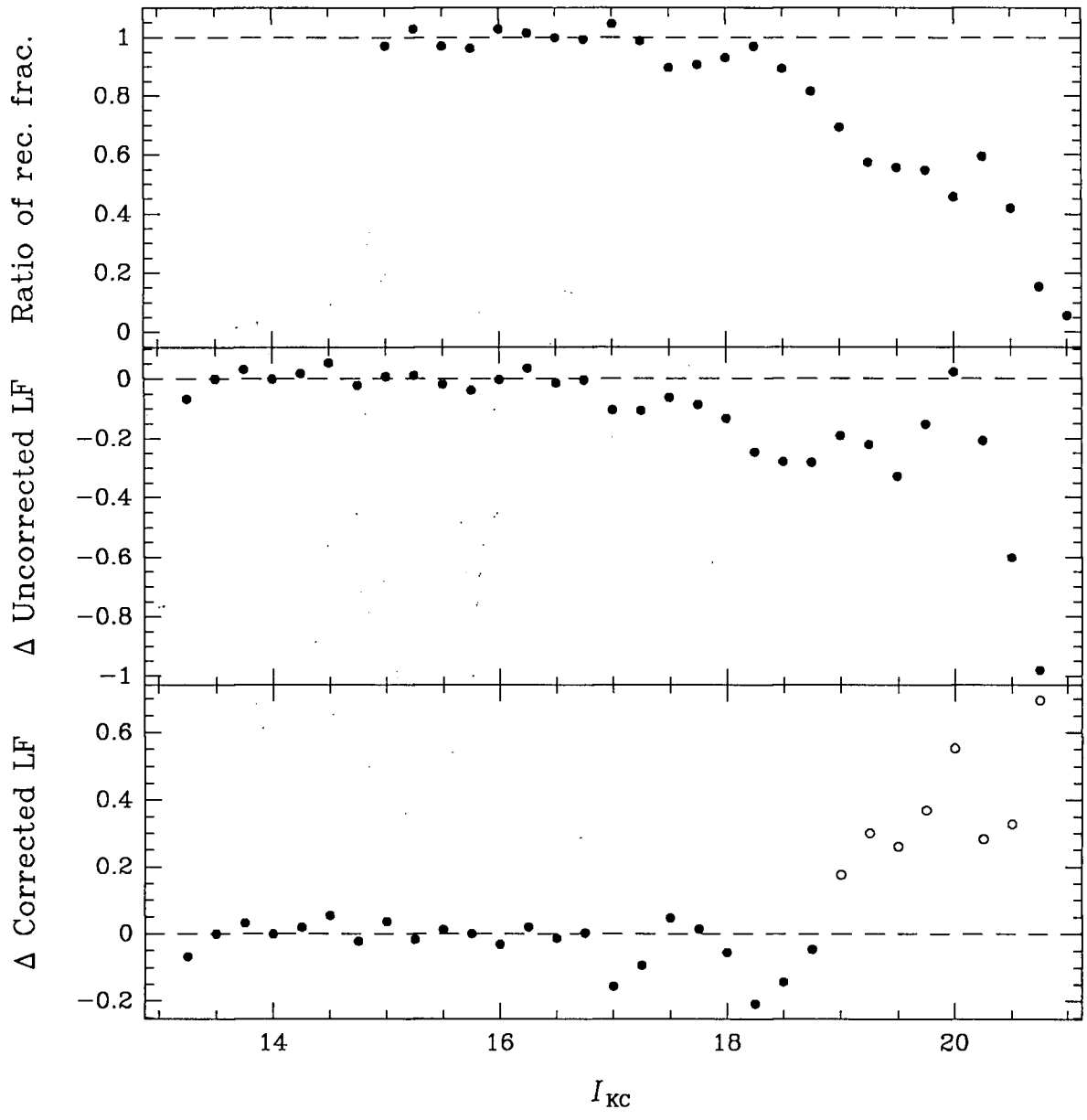

FIGURE 6.6. Comparison of frames with 5% and 100% add levels

The ratio of the recovery fractions (in the sense 100% ÷ 5%) are shown in the upper panel. The lower panels show differences in the uncorrected and corrected luminosity functions (see Figures 6.3 and 6.5). The difference, Δ, is in the sense (100% −5%) ÷ 5%. Open points in the bottom panel indicate that the recovery fraction was less than 50 per cent, and dashed lines are to guide the eye.

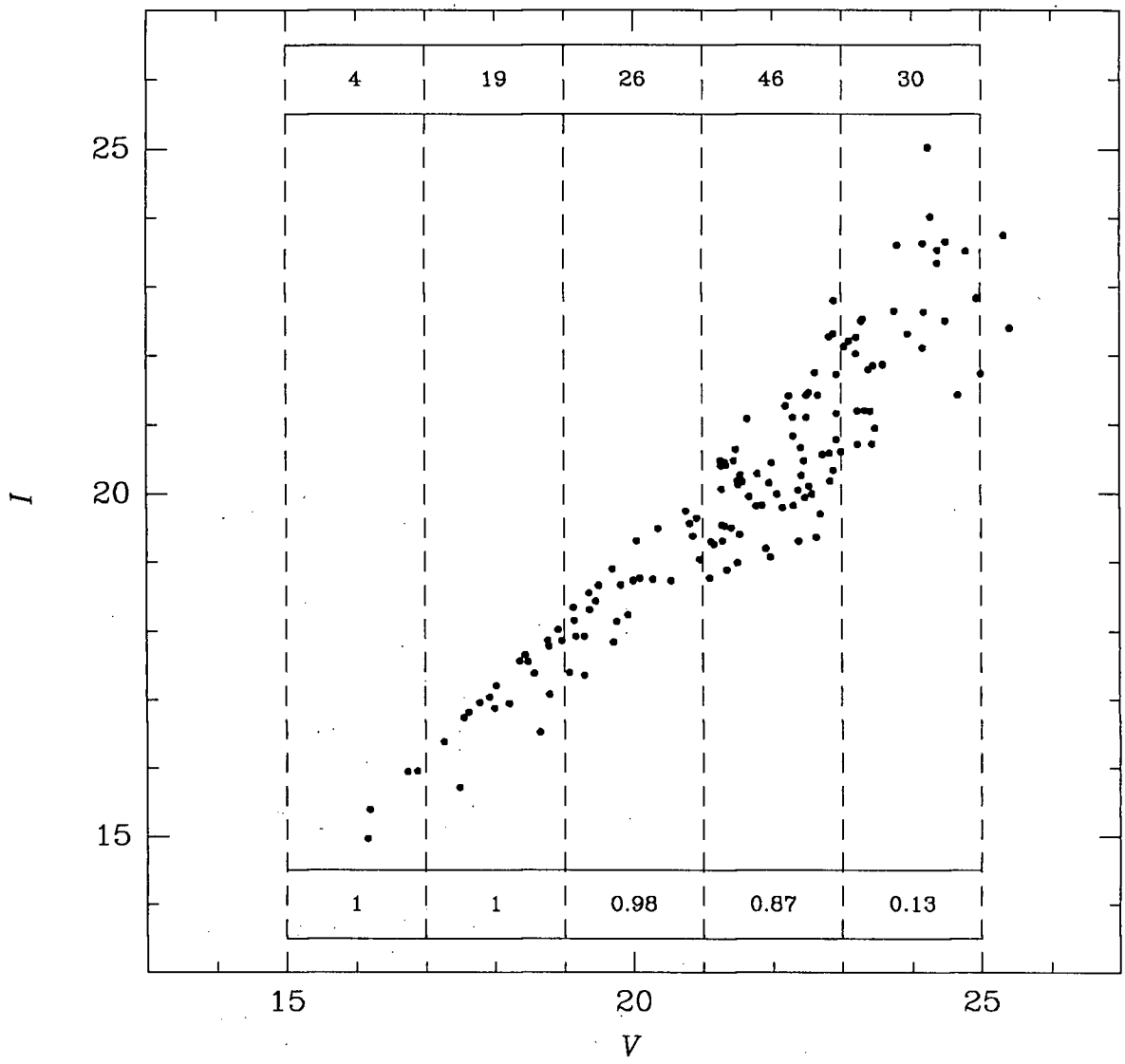

FIGURE 6.7. Stars found in two colours, with bins and incompleteness shown

The stars shown were found on both the TI *V* and *I* background fields. The incompleteness of each *V* bin is indicated in the lower part of the panel and the uncorrected number of stars in each bin in the upper part of the panel.

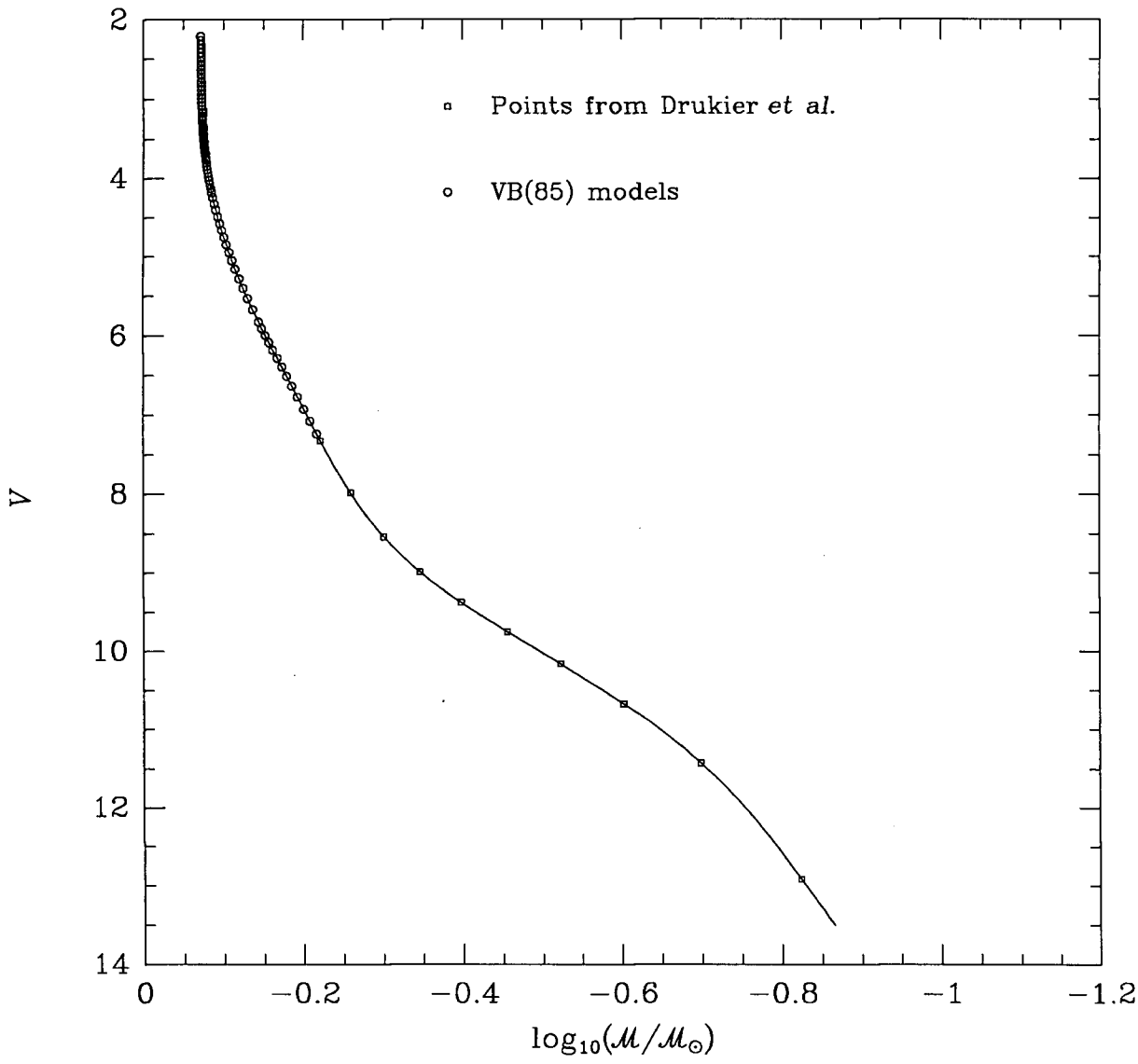

FIGURE 6.8. V mass-luminosity relationship

The relationship is from Drukier *et al.* (1988). Circles denote values from VB85 isochrones, while squares indicate the Drukier *et al.* extension of the relationship to fainter magnitudes.

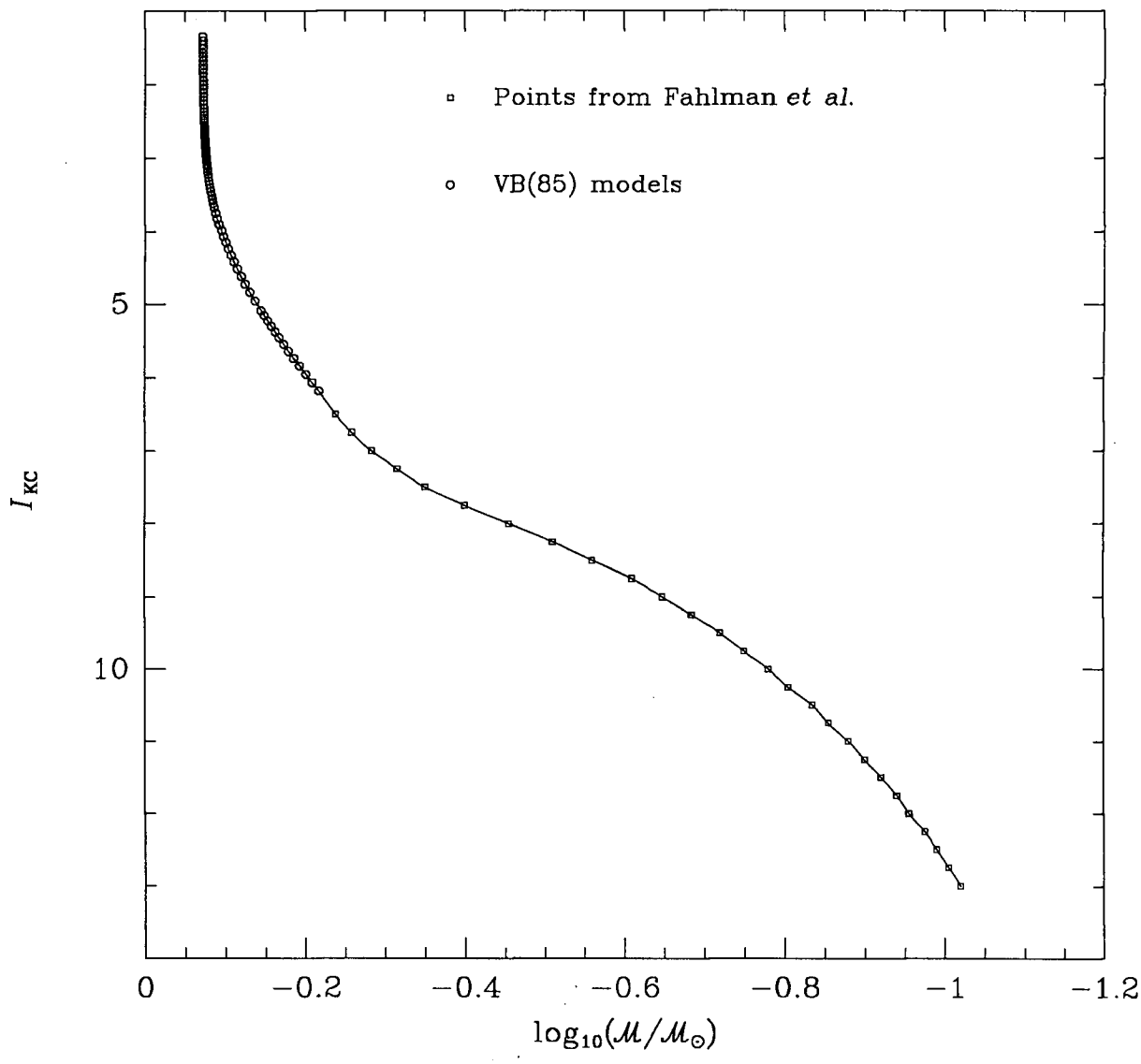

FIGURE 6.9. I mass-luminosity relationship

Circles denote points taken from VB85 isochrones, while squares denote points from the Fahlman *et al.* (1989) MLR, which was adopted for $I > 6\overset{m}{.}5$.

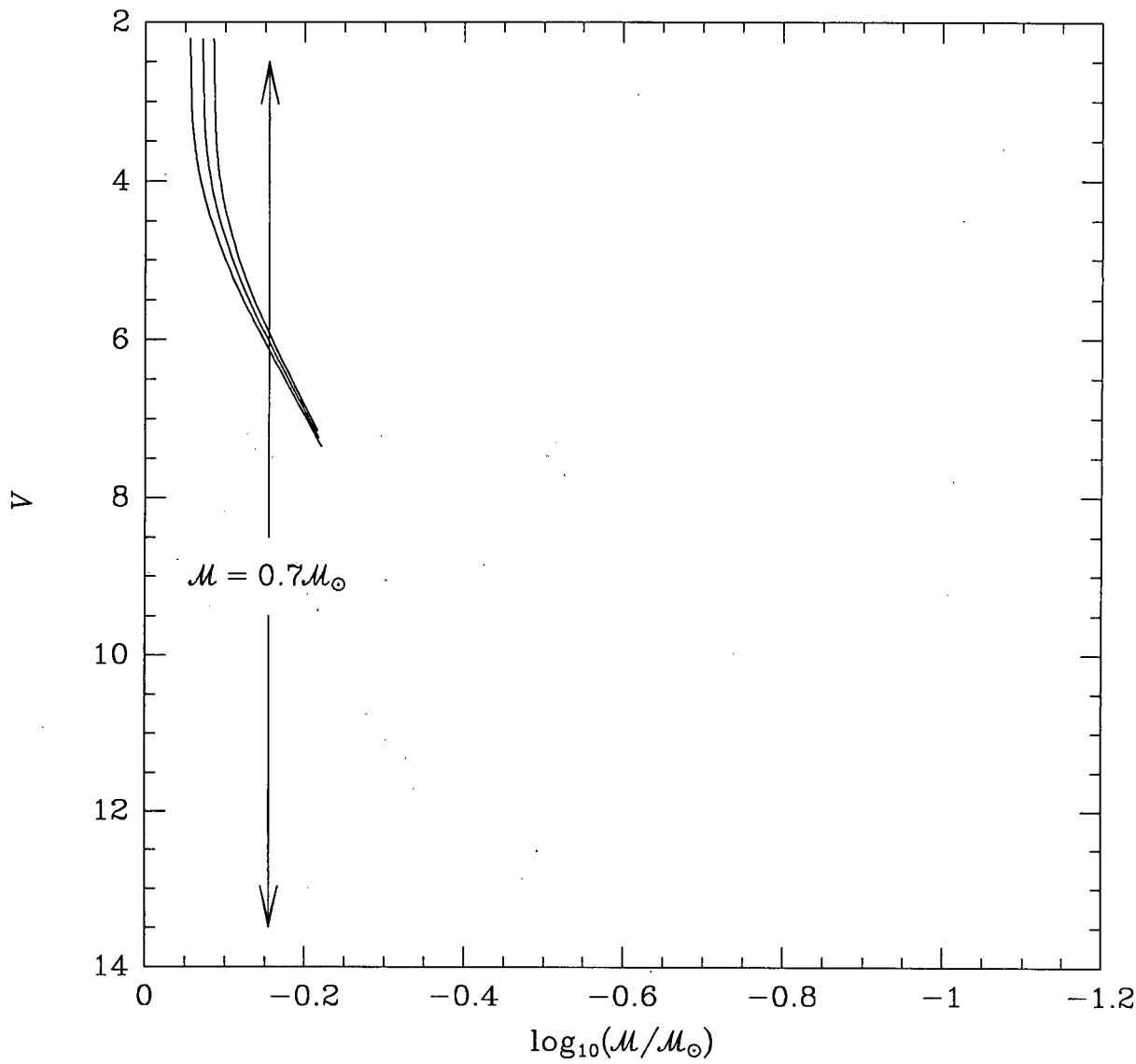

FIGURE 6.10. The effect of cluster age on the V MLR

The three curves are VB85 model isochrones with α=1.6, [Fe/H]=−1.27, and Y=0.20 and ages of 14, 16 and 18 Gyr from left to right respectively. The point on the abscissa corresponding to a mass of $0.7\mathcal{M}_\odot$ is indicated.

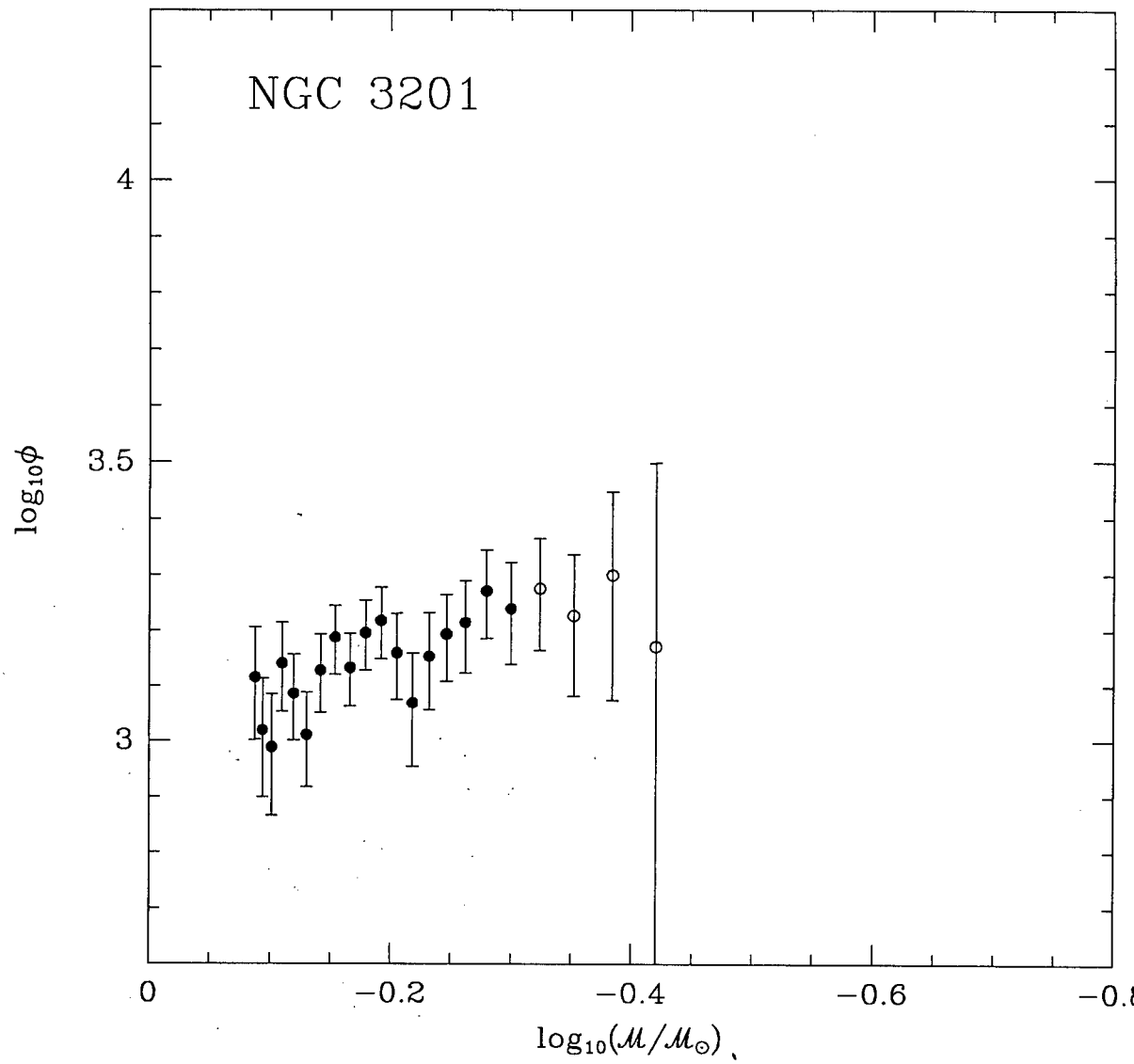

FIGURE 6.11. Mass function for the V TI program field

The stars were binned into bins of width $0\overset{m}{.}5$ and interval $0\overset{m}{.}25$. The mass function has been corrected for background objects. Open circles indicate bins in which the completeness was less than 0.5.

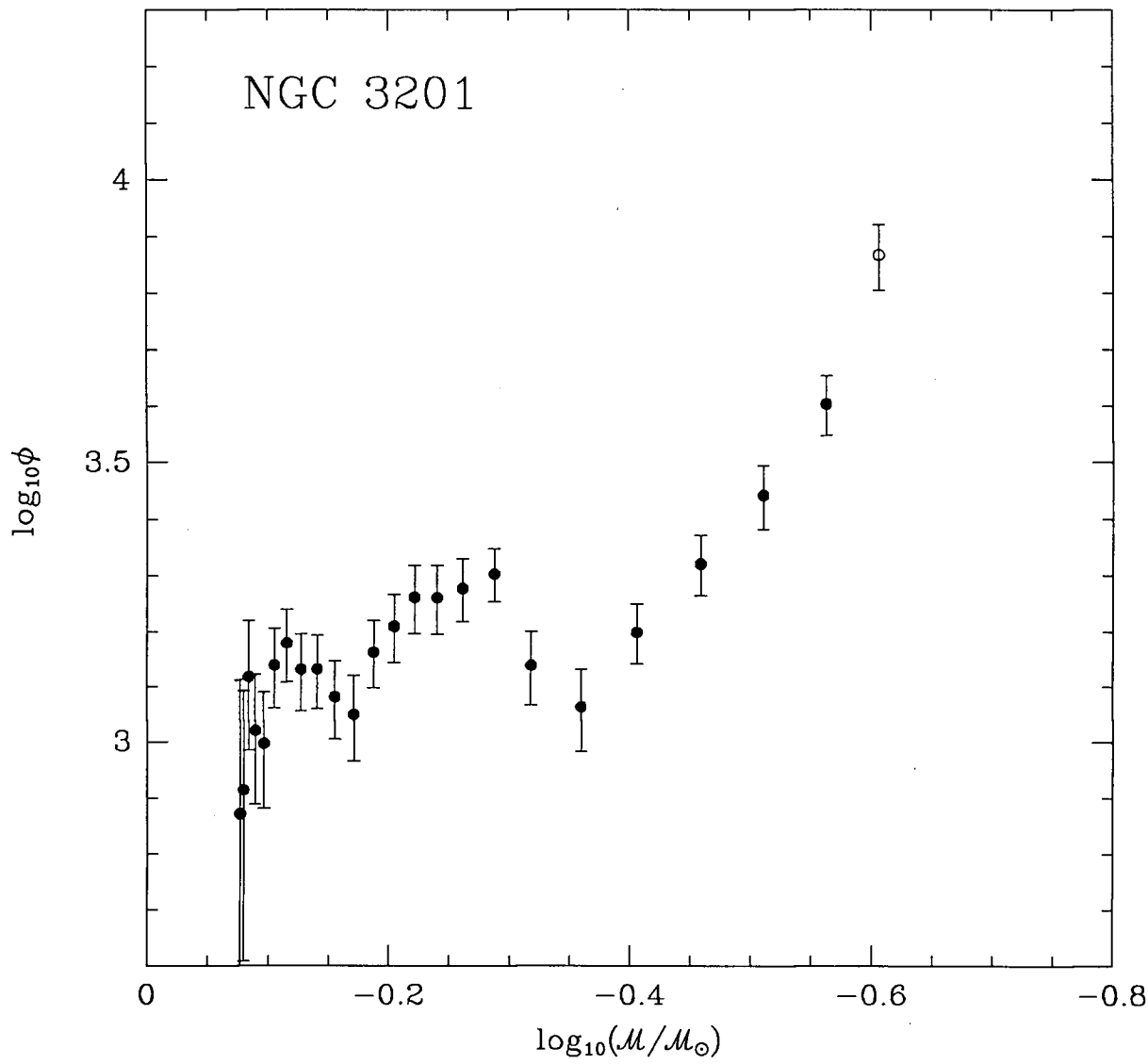

FIGURE 6.12. Mass function for the I TI program field

The stars were binned into bins of width $0\overset{m}{.}5$ and interval $0\overset{m}{.}25$. The mass function has been corrected for background objects. Open points indicate bins in which the completeness was less than 0.5.

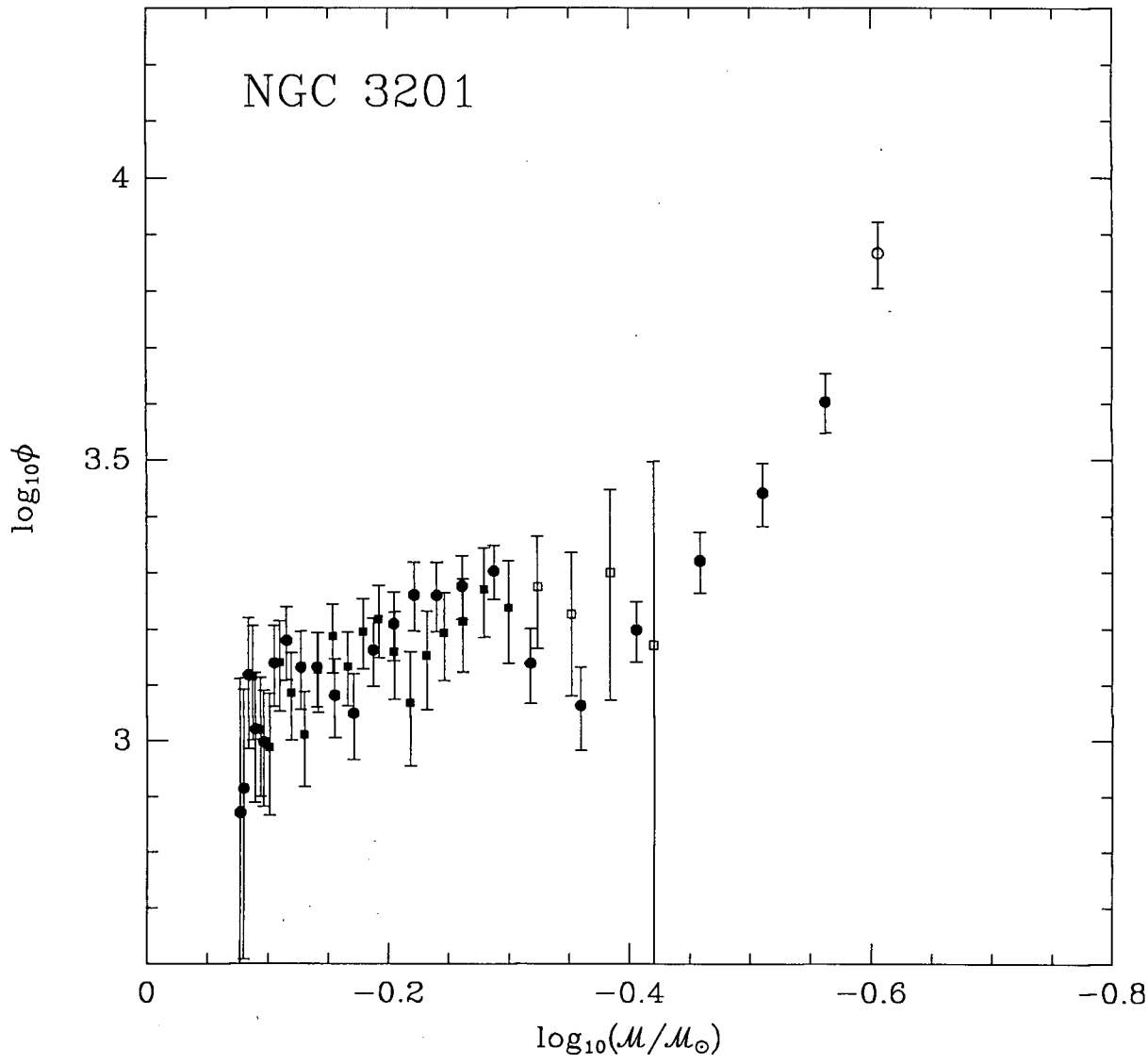

FIGURE 6.13. Mass functions for V and I TI program fields

Squares are for the '*V* mass function' and Circles are for the '*I* mass function'. The stars were binned into bins of width $0\overset{m}{.}5$ and interval $0\overset{m}{.}25$. The mass functions were corrected for background objects. Open points indicate bins in which the completeness was less than 0.5.

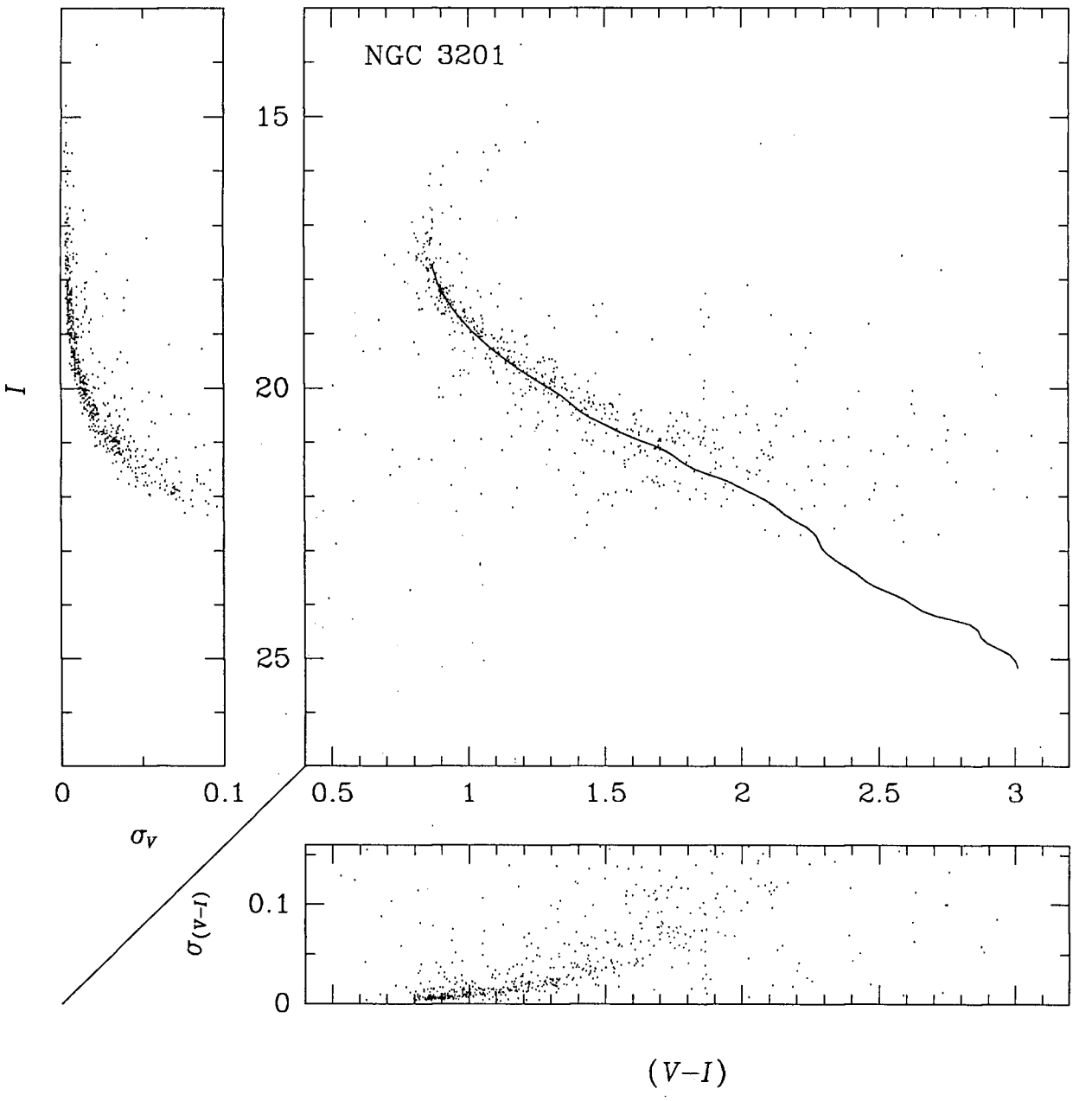

FIGURE 6.14. An isochrone derived from the V and I MLRs

The points shown were derived by matching stars found on a standard reduction of the binned *V* and *I* fields. The stars were calibrated to absolute magnitudes by use of colour-less transformations, equations 3.18, and the errors are those returned by ALLSTAR, added in quadrature for $(V-I)$. The isochrone was reddened by $\mathrm{E}(V-I)$=0$^{\mathrm{m}}$.286 and corrected for the *I* distance modulus of NGC 3201.

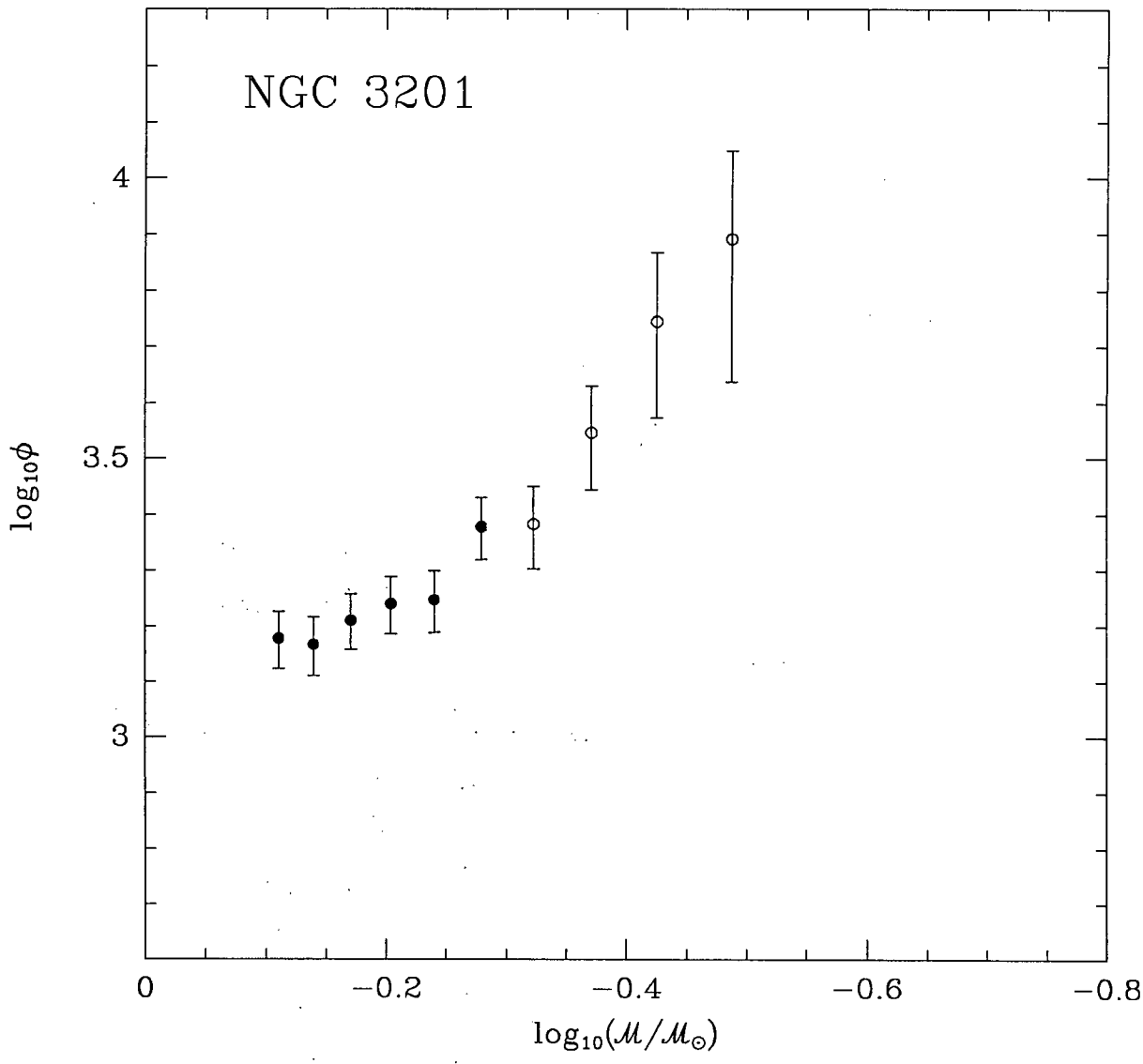

FIGURE 6.15. Uncorrected mass function for the V TI program field

The mass function was not corrected for background objects. The bins used are of equal width in mass. Open circles indicate bins in which the completeness was less than 0.5.

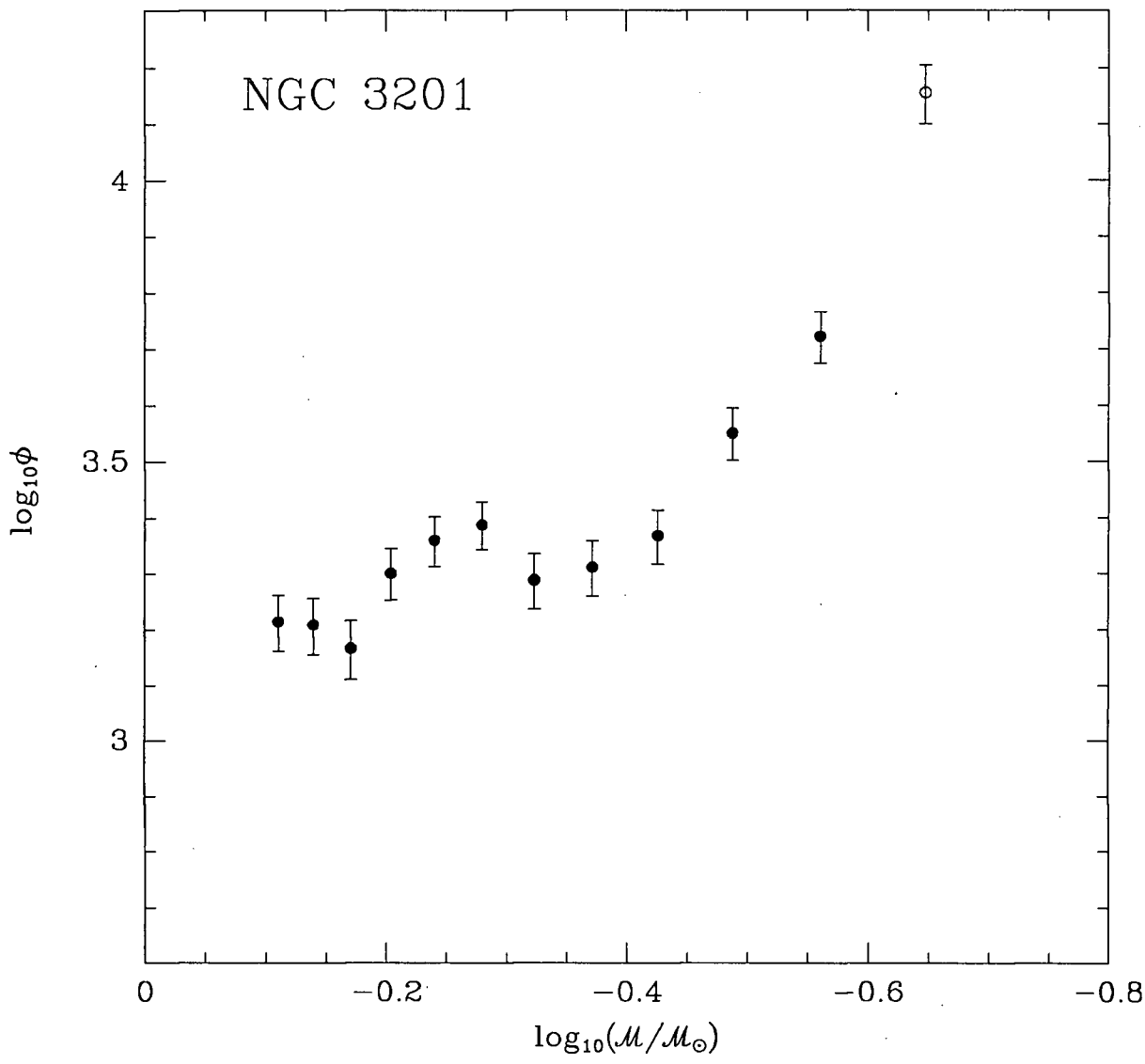

FIGURE 6.16. Uncorrected mass function for the I TI program field

The mass function was not corrected for background objects. The bins used are of equal width in mass. Open circles indicate bins in which the completeness was less than 0.5.

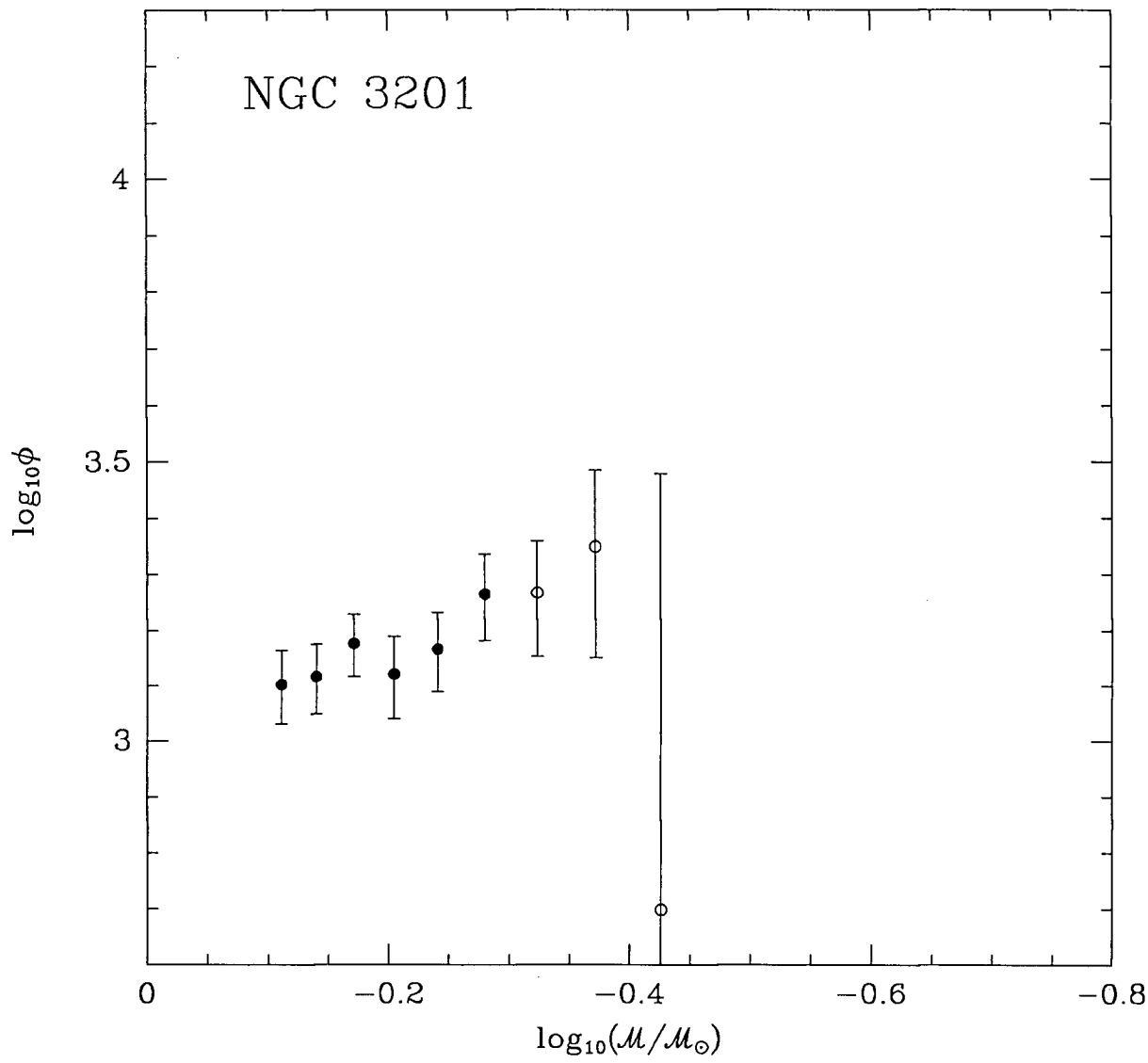

FIGURE 6.17. Corrected mass function for the V TI program field

The mass function was corrected for background objects. The bins used are of equal width in mass. Open circles indicate bins in which the completeness was less than 0.5.

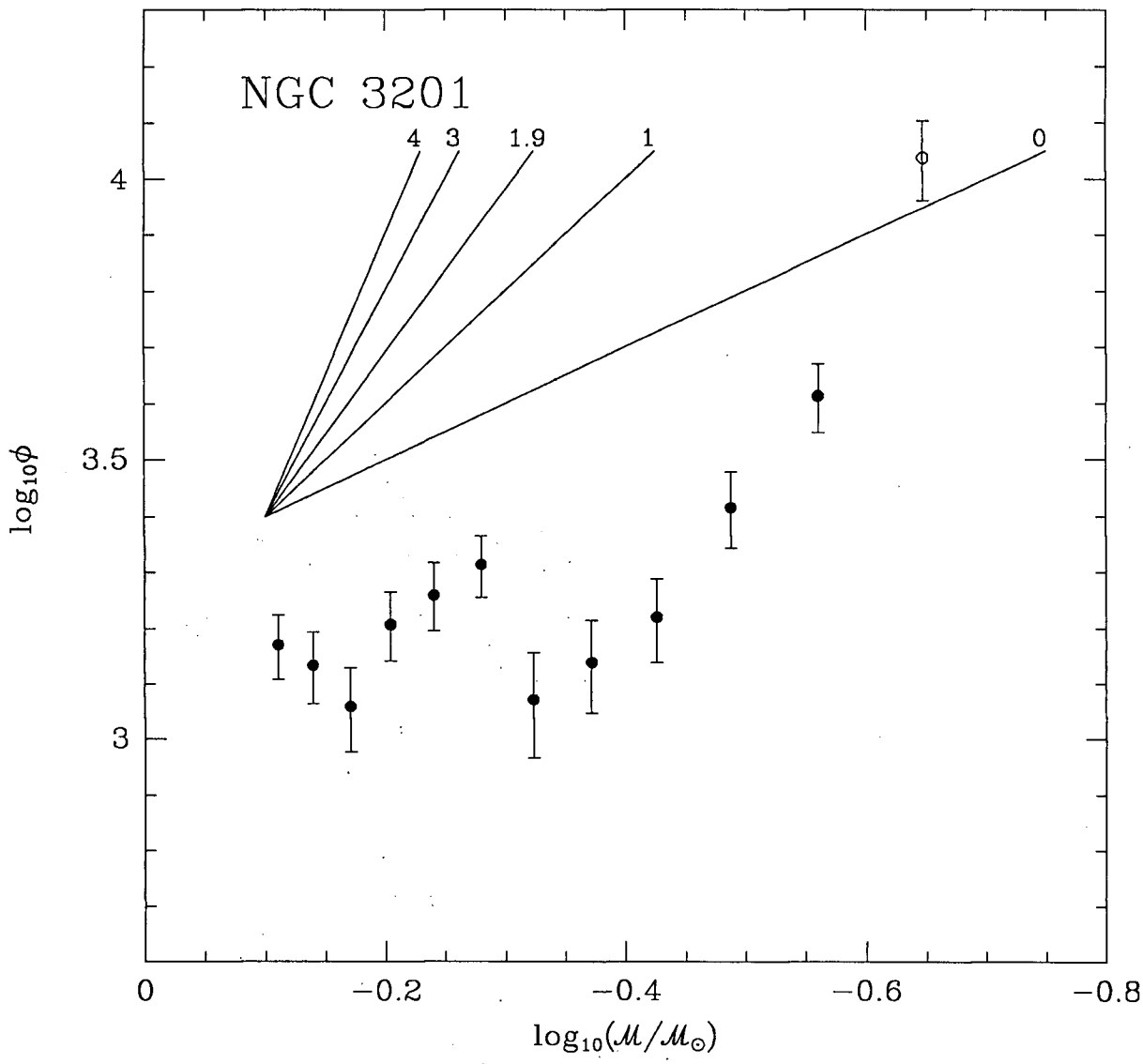

FIGURE 6.18. Corrected mass function for the I TI program field.

The mass function was corrected for background objects. Bins used are of equal width in mass. Open circles indicate bins in which the completeness was less than 0.5. The solid lines indicate relationships of the form

$$log_{10}\phi = log_{10}\left[\left(\frac{\mathcal{M}}{\mathcal{M}_\odot}\right)^{-(1+x)}\right],$$

with x having the values indicated.

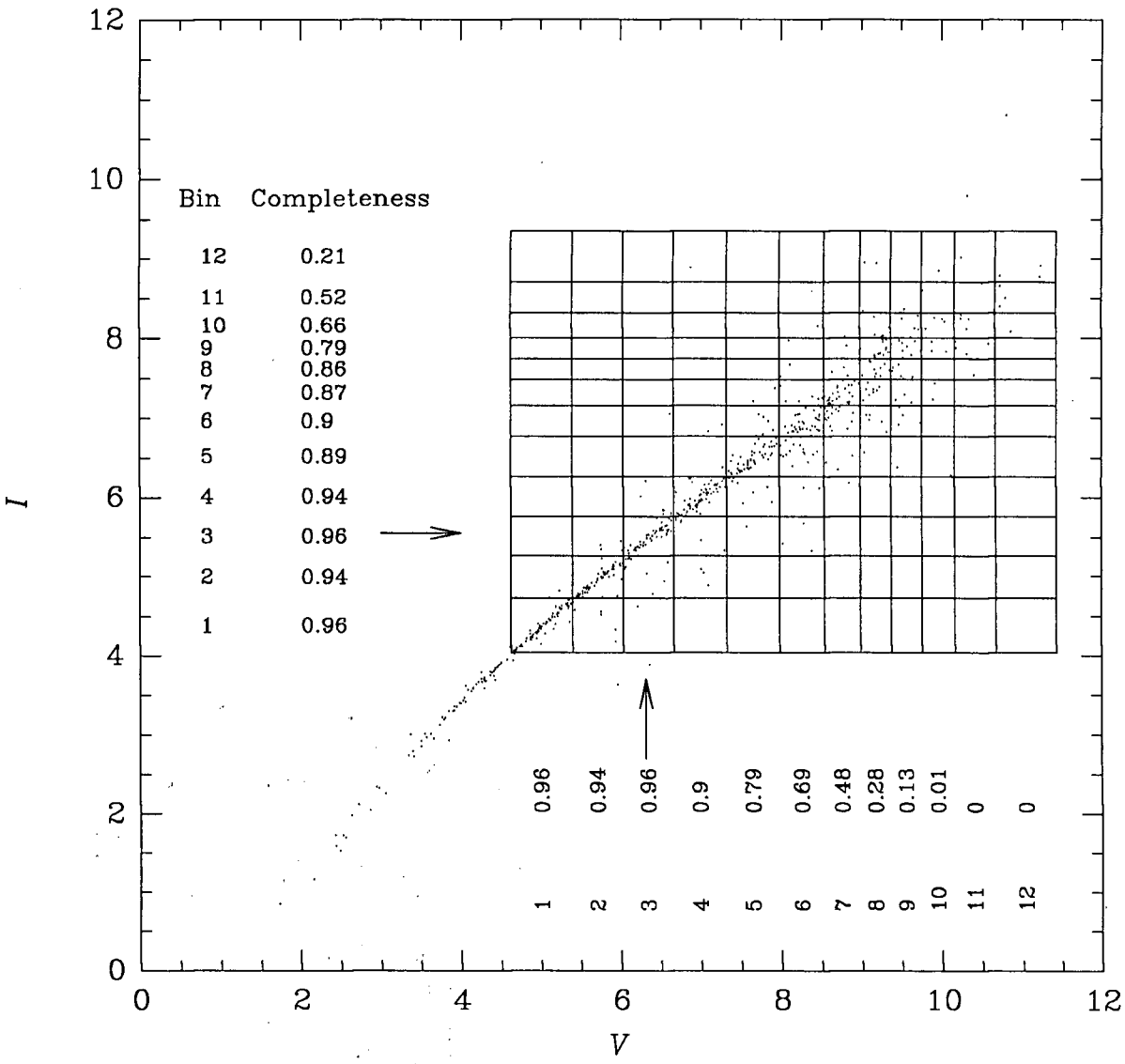

FIGURE 6.19. A 'magnitude-magnitude diagram' for the TI program field

The diagram was generated by matching stars on the binned *V* and *I* program fields. The magnitude equivalents of equal mass divisions (in $0.05\mathcal{M}_{\odot}$) are shown. The bins are numbered, and the recovery efficiencies in the bins are indicated.

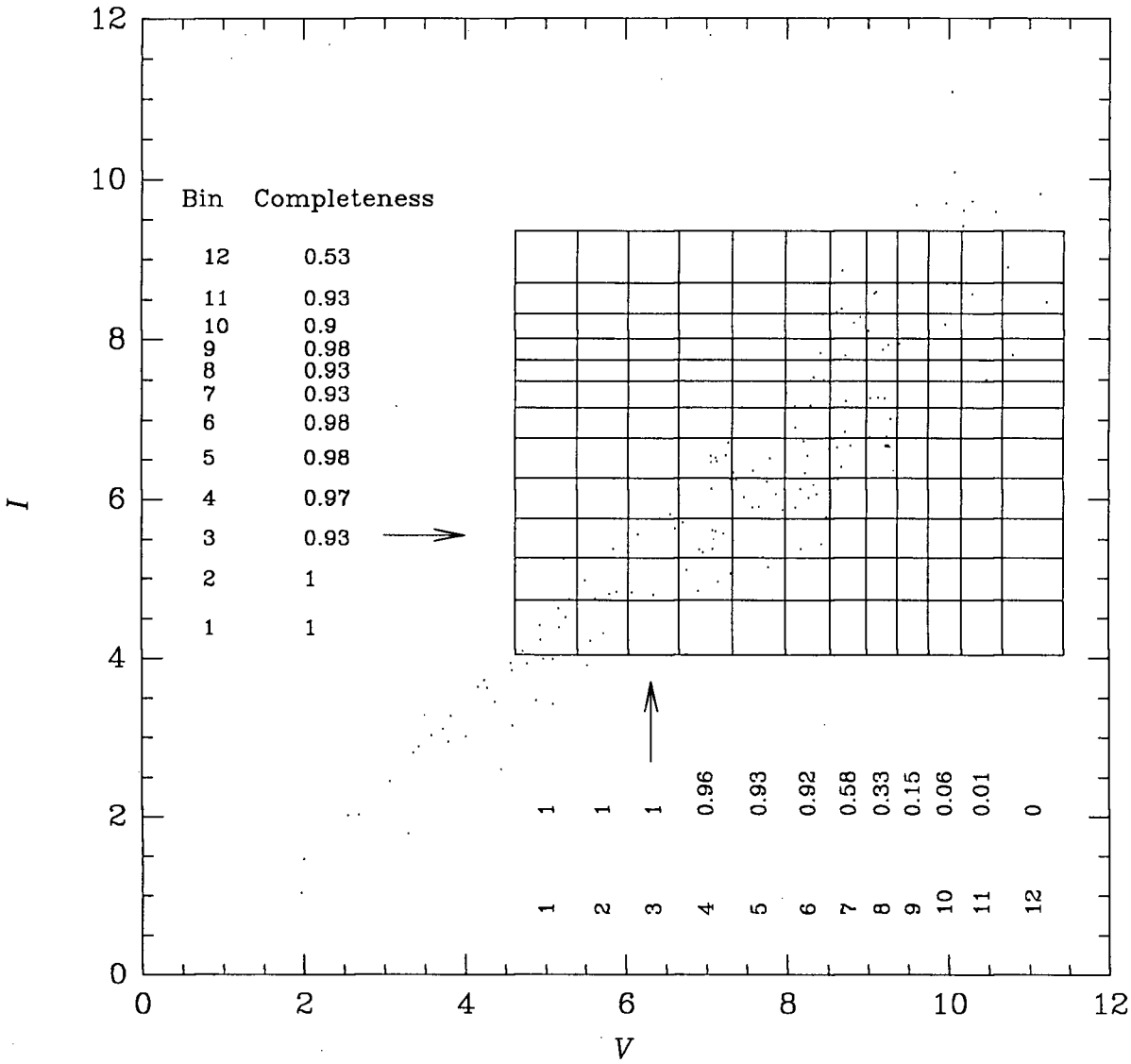

FIGURE 6.20. A 'magnitude-magnitude' diagram for the TI background field

The diagram was generated by matching stars on the binned *V* and *I* background fields. The magnitude equivalents of equal mass divisions (in $0.05\mathcal{M}_{\odot}$) are shown. The bins are numbered, and the recovery efficiencies indicated.

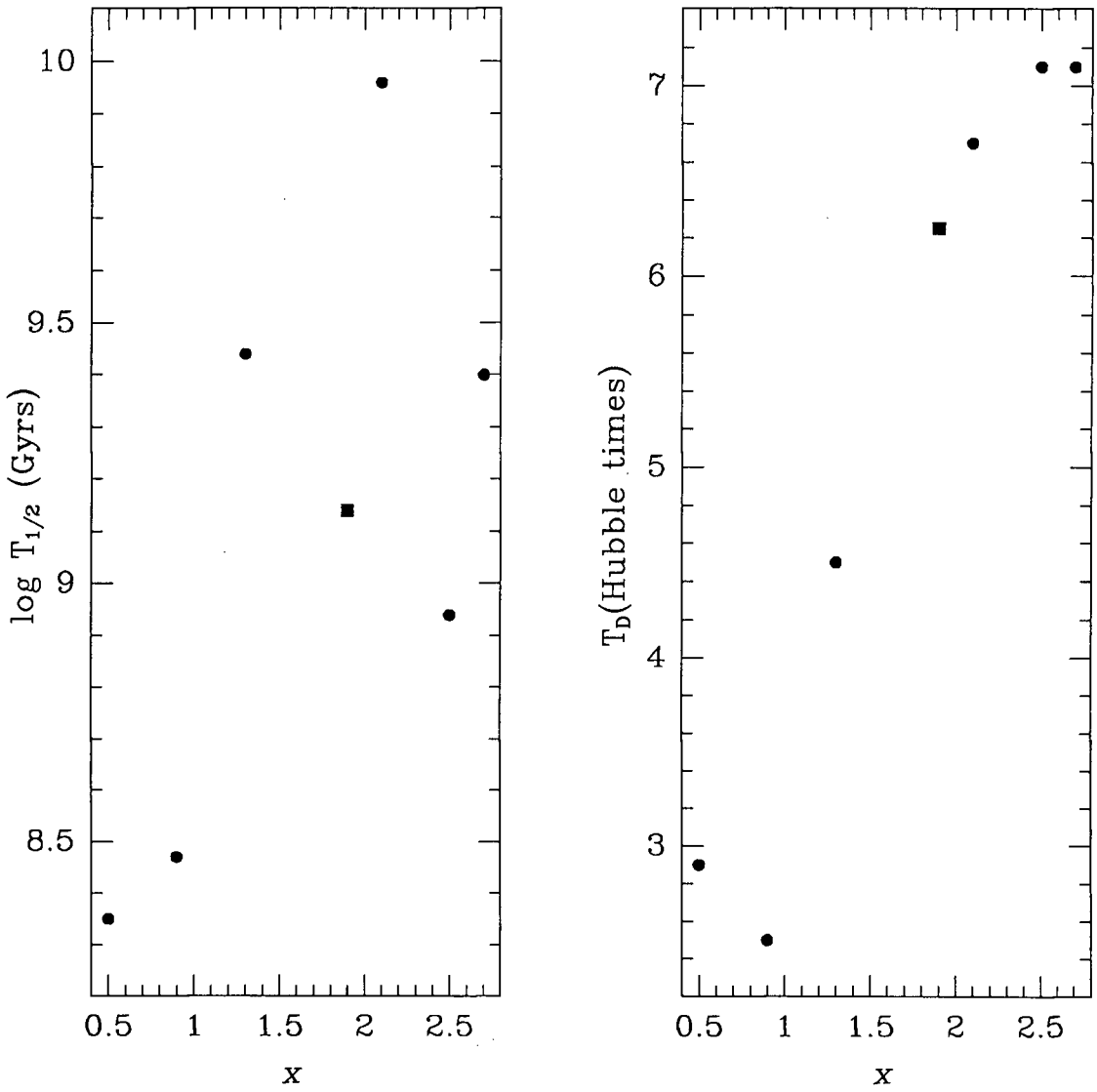

FIGURE 6.21. Plots of half-mass relaxation time and 'time until destruction' against mass function slope below 0.4$\mathcal{M}_\odot$

Circles represent data from RFBFST, while the square represents data for NGC 3201, the value of *x* being determined in this study.

Chapter 7
CONCLUSIONS

Both deep and shallow CMDs were produced for NGC 3201. The shallow data allowed for estimates of the cluster reddening and metallicity. The values obtained were not as tightly constrained as previous studies, but did show general agreement. Matching the deep CMD to a subdwarf fiducial allowed for a value of the distance modulus to be derived. A value of $(m - M)_V$=14$^{\rm m}$.2 was found, in agreement with other values in the literature.

Synthetic isochrone fitting to the deep CMDs implied an age of 15 ± 2 Gyrs on the scale of VB85. Isochrone fitting to the shallow data set produced consistent results, though in both cases the fitting was poor, and the derived ages must be taken as being inconclusive.

No obvious equal-mass binary sequence was seen in either the TI or TEK field, though it was stressed that this does not preclude the possibility of binaries in NGC 3201.

The CMD for the shallower data set had a group of blue stragglers. The blue stragglers were shown to be more centrally concentrated than subgiant stars in the same magnitude range. This provides strong evidence for mass segregation in NGC 3201.

An unusual star, first observed by Lee (1977), was noted. New values were derived for the *U, B* and *V* magnitudes of the star, the new values being contrary to those of Lee, due to a possible mismatch by him. The possible nature of the object was speculated on.

Using Monte Carlo techniques, the luminosity function of the cluster in both the *V* and the *I* band was derived. The *I* band MLR from Fahlman *et al.* (1989) was adapted slightly, and then used to generate the mass function of NGC 3201. A *V* band MLR from Drukier *et al.* (1988) was similarly used to generate a mass function. Differences between the two mass functions are discussed, and a reason proposed for the differences seen. The two MLRs were used to generate a synthetic isochrone, and this isochrone was shown to follow the morphology of the data. This shows that the two MLRs are of the right form, unless errors had conspired to give the apparent match.

Finally, the gradient of the mass function was determined for the lower mass stars. The mass function for the less massive stars was found to have a slope of x=1.9. The 'time until destruction' and the 'destruction rate' for the cluster are found, and the data are found to fit into the picture of RFBFST well, implying that many dynamical processes are at work in the destruction of globular clusters.

BIBLIOGRAPHY

Aguilar, L., Hut, P., and Ostriker, J.P. 1988, *Ap. J.* **335**, 720

Alcaino, G. 1974, in *Atlas of Globular Clusters* (Talleres de la imprenta de la universidad católica de Chile), p. 26

Alcaino, G. 1976, *Astron. Astrophys. Suppl.* **28**, 409

Alcaino, G., and Liller, W. 1981, *A. J.* **86**, 1480

Alcaino, G., and Liller, W. 1984, *A. J.* **89**, 1712

Alcaino, G., Liller, W., and Alvarado, F. 1989, *Astron. Astrophys.* **216**, 68 (ALA89)

Bahcall, J.N., and Soneira, R.M. 1980, *Ap. J. Suppl.*, **44**, 73

Bahcall, J.N., and Soneira, R.M. 1984, *Ap. J. Suppl.*, **55**, 67

Bennett, P.D. 1989, *OPDATA Reference Manual* (Vancouver: TRIUMF Computing Document)

Bevington, P.R. 1969, *Data Reduction and Error Analysis for the Physical Sciences* (New York: McGraw-Hill), chapter 4

Binney, J., and Tremaine, S. 1987, Galactic Dynamics (Princeton: Princeton University Press), p. 514

Bolte, M. 1988, *P.A.S.P.* **100**, 869

Bolte, M. 1989, *Ap. J.* **341**, 168

Börner, G. 1988, *The Early Universe* (Berlin Springer-Verlag)

Buonanno, R., Buscerna, G., Corsi, C.E., Ferraro, I., and Iannicola, G. 1983, *Astr. Ap*, **126**, 278

Cacciari, C. 1984, *A. J.* **89**, 231

Carney, B.W. 1980, *Ap. J. Suppl.* **42**, 481

Chieffi, A., Straniero, O., and Salaris, M. 1991, in *ASP Conference Series Volume 13, The Formation and Evolution of Star Clusters*, ed. Kenneth James (BookCrafters inc.), p. 219

Cohen, J.G., Frogel, J.A., Personn, S.E., and Elias, J.H. 1981, *Ap. J.* **249**, 481

Da Costa, G.S., Frogel, J.A., and Cohen, J.G. 1981, *Ap. J.* **248**, 612

D'Antona, F. 1987, *Ap. J.* **320**, 653

Demarque, P., and McClure, R. 1977, In *The Evolution of Galaxies and Stellar Populations*, eds. B. Tinsley and R.B. Larson (Yale University Observatory, New Haven)

Downes, R.A. 1986, *Ap. J. Suppl.* **61**, 569

Drukier, G.A., Fahlman, G.G., Richer, H.B., and VandenBerg, D.A. 1988, *A. J.* **95**, 1415

Drukier, G.A., Fahlman, G.G., and Richer, H.B. 1989, *Ap.J.* **342**, L27

Fahlman, G.G., Richer, H.B., and VandenBerg, D.A. 1985, *Ap. J. Suppl.* **58**, 225

Fahlman, G.G., Richer, H.B., Searle, L., and Thompson, I.B. 1989, *Ap. J.* **343**, L49

Fich, M., and Tremaine, S. 1990, Preprint

Frogel, J.A., Cohen, J.G., and Personn, S.E. 1983, *Ap. J.* **275**, 773

Graham, J.A. 1981, *P.A.S.P.* **93**, 291

Gratton, R.G. 1982, *Astron. Astrophys.* **115**, 171

Gratton, R.G., and Ortolani, S. 1989, *Astron. Astrophys.* **211**, 41

Greenstein, J.L., and Sargent, A.I. 1974, *Ap. J. Suppl.* **28**, 157

Heber, U. 1986, *Astron. Astrophys.* **155**, 33

Iben, I., and Rood, R.T. 1970, *Ap. J.* **159**, 605

King, I.R. 1966, *A. J.* **71**, 64

King, I.R. 1971, *P.A.S.P.* **83**, 199

Kinman, T.D. 1959, *M.N.R.A.S.* **119**, 157

Landolt, A.U. 1973, *Astron. J.* **78**, 959

Landolt, A.U. 1983, *Astron. J.* **88**, 439

Lang, K.R. 1980, in *Astrophysical Formula (second edition)* (New York: Springer-Verlag), p. 518

Larson, R.B. 1976, in *Galaxies*, eds. L. Martinet and M. Mayer (Geneva: Geneva Observatory), p. 67

Larson, R.B. 1986, in *IAU Symposium 126, The Harlow-Shapley Symposium on Globular Cluster Systems in Galaxies*, eds. J.E. Grindlay and A.G. Davis Philip (Dordrecht: Kluwer), p. 311

Lee, S.W. 1977, *Astron. Astrophys. Suppl.* **28**, 409

Leonard, P.J.T. 1989, *A. J.* **98**, 217

Lutz, T.E., Hanson, R.B., and Van Altena, W.F. 1988, in *The Extragalactic Distance Scale*, eds. S. van den Bergh and C.J. Pritchett (Utah: Brigham Young University Print Services)

Luyten, W.J. 1955, *A Catalogue of 1849 Stars with Proper Motions Exceeding 0."5 Annually* (Minneapolis: Lund Press)

MacKay, C.D. 1986, *Ann. Rev. Astron. Astrophys.* **24**, 255

McClure, R.D., Hesser, J.E., Stetson, P.B. and Stryker, L.L. 1985, *P.A.S.P.* **97**, 665

McClure, R.D., VandenBerg, D.A., Smith, G.H., Fahlman, G.G., Richer, H.B., Hesser, J.E., Harris, W.E., Stetson, P.B., and Bell, R.A. 1986, *Ap. J.* **307**, L49

Menzies, J. 1967, *Ph. D. thesis* (Australian National University)

Mihalas, D., and Binney, J. 1981, *Galactic Astronomy (second edition)* (San Francisco: Freeman)

Nemec, J.M., and Harris, H.C. 1987, *Ap. J.* **316**, 172

Penny, A.J. 1984, in *IAU symposium 105, Observational Tests of the Stellar Evolution Theory*, eds. A. Maeder and A. Renzini (Dordrecht: Reidel), p. 157

Penny, A.J., and Dickens, R.J. 1986, *M.N.R.A.S.* **220**, 845

Peterson, B.A., Murdin, P., Wallace, P.T., Manchester, R.N., Penny, A.J., Jordan, A., Hartley, K.F., and King, D. 1978, Nature **276**, 475

Pilachowski, C.A., Sneden, C., and Canterna, R. 1980, in *IAU symposium 85, Star Clusters*, ed. J. Hesser (Dordrecht: Reidel), p. 467

Pilachowski, C.A., Sneden, C., and Wallerstein, G. 1983, *Ap. J. Suppl.* **52**, 241

Press, W.H., Flannery, B.P., Teukolsky, S.A., and Vetterling, W.T. 1987, in *Numerical Recipes. The Art of Scientific Computing* (Cambridge: Cambridge University Press)

Richer, H.B., and Fahlman, G.G. 1986, *Ap. J.* **304**, 273

Richer, H.B., and Fahlman, G.G. 1988, *Ap. J.* **325**, 218

Richer, H.B. 1991, Preprint

Richer, H.B., and Fahlman, G.G., 1991, in *ASP Conference Series Volume 13, The Formation and Evolution of Star Clusters*, ed. Kenneth James (BookCrafters inc.), p. 219

Richer, H.B., Fahlman, G.G., Buonanno, R., Fusi Pecci, F., Searle, L., and Thompson, I.B. 1991, *Ap. J.* **381** in press (RFBFST)

Rodgers, A.W., and Eggen, J. 1974, *P.A.S.P.* **86**, 742

Sandage, A. 1969, *Ap. J.* **158**, 1115

Sato, T., Richer, H.B., and Fahlman, G.G. 1989, *A. J.* **98**, 1335

Savage, B.D., and Mathis, J.S. 1979, *Ann. Rev. Astron. Astrophys.* **17**, 73

Searle, L., and Zinn, R. 1978, *Ap. J.* **225**, 357

Spitzer, L. (Jr.), and Mathieu, R.D. 1980, *Ap. J.* **241**, 618

Spitzer, L. (Jr.) 1987, in *Dynamical Evolution of Globular Clusters* (Princeton: Princeton University Press)

Stetson, P.B. 1987a, *DAOPHOT Users Manual* (Victoria: Dominion Astrophysical Observatory)

Stetson, P.B. 1987b, *P.A.S.P.* **99**, 191

VandenBerg, D.A. 1983, *Ap. J. Suppl.* **51**, 29

VandenBerg, D. A., and Bell, R.A. 1985, *Ap. J. Suppl.* **58**, 561 (VB85)

VandenBerg, D.A., Bolte, M., and Stetson, P.B. 1990, *A. J.* **100**, 445

Webbink, R.F. 1985, in *IAU symposium 113, Dynamics of Star Clusters*, eds. J. Goodman and P. Hut (Dordrecht: Reidel), p. 541

White, R.E., and Kraft, T.T. 1972, *P.A.S.P.* **84**, 298

Zinn, R.J. 1980a, *Ap. J. Suppl.* **42**, 19

Zinn, R.J. 1980b, *Ap. J.* **241**, 602

Zinn, R.J., and West, M.J. 1984, *Ap. J. Suppl.* **55**, 45

Zinn, R.J. 1985, *Ap. J.* **293**, 424